Université Paris 13

THÈSE

Présentée pour l'obtention du grade de

Docteur de l'Université Paris 13

Discipline: Mécanique et Matériaux

par

Takayuki OTSUKA

Modélisation micromécanique de la plasticité de transformation dans les aciers par homogénéisation numérique fondée sur la TFR

soutenue publiquement **le 27 janvier 2014**
devant le jury composé de

M. **Sibrand van der Zwaag**, Professeur, Université de Delft (Pays-bas), rapporteur
M. **Marc Bernacki**, Chargé de recherche, HDR, CEMEF, Mines ParisTech, rapporteur
M. **Jean-Baptiste Leblond**, Professeur, Université Paris 6, examinateur
M. **Patrick Franciosi**, Directeur de recherche CNRS, LSPM, Université Paris 13, examinateur
Mme **Brigitte Bacroix**, Directeur de recherche CNRS, LSPM, Université Paris 13, directrice de thèse
M. **Renald Brenner**, Chargé de recherche CNRS, IJLRDA, Université Paris 6, directeur de thèse

LSPM–CNRS, Université Paris 13
99. av. J.B. Clément, 93430 Villetaneuse, France

Université Paris 13

DISSERTATION

Submitted for the degree of

Doctor of Paris 13 University

Speciality: Mechanics and Materials

by

Takayuki OTSUKA

Micromechanical modelling of transformation plasticity in steels based on fast Fourier transform numerical scheme

defended publicly **on January 27th, 2014**
in front of the jury composed of

M. **Sibrand van der Zwaag**, Professor, Technical University of Delft, referee
M. **Marc Bernacki**, Research Scientist, HDR, CEMEF, Mines ParisTech, referee
M. **Jean-Baptiste Leblond**, Professor, Paris 6 University, examiner
M. **Patrick Franciosi**, Directeur de recherche CNRS, LSPM, Paris 13 University, examiner
Mme **Brigitte Bacroix**, CNRS Research Scientist, Directeur de recherche CNRS, LSPM, Paris 13 University, PhD supervisor
M. **Renald Brenner**, CNRS Research Scientist, IJLRDA, Paris 6 University, PhD supervisor

LSPM–CNRS, Paris 13 University
99. av. J.B. Clément, 93430 Villetaneuse, France

Université Paris 13 ; Sorbonne Paris Cité,
Labratoire des Sciences des Procédés et des Matériaux,
UPR 3407, 99 avenue Jean-Baptiste Clément, 93430,
Villetaneuse, France

École doctorale Galilée
Université Paris 13, 99,
avenue Jean-Baptiste
Clément, Villetaneuse

Résumé

Au cours de processus thermomécaniques engendrant une transformation de phase dans les aciers, une déformation plastique importante peut se produire sous l'effet d'une contrainte appliquée, même si celle-ci est plus faible que la limite d'élasticité de la phase la plus molle. Ce phénomène s'appelle plasticité de transformation ou TRansformation Induced Plasticity (TRIP), et peut jouer un rôle important sur le contrôle des procédés de transformation industriels. Par exemple, au cours du refroidissement par trempe de produits semi-finis ou finis (plaques, tôles, roues, ...), ce phénomène peut affecter la planéité des produits plats et engendrer des contraintes résiduelles qui vont affecter la qualité finale de produits finis. Il s'avère donc important de prévoir cette plasticité de transformation induite par un chargement thermomécanique donné.

Dans cette thèse, un modèle micromécanique de plasticité cristalline avec transformation de phase a été développé. Il s'appuie sur l'utilisation de la transformée de Fourier rapide (TFR) développée pour des milieux périodiques. L'expansion volumique induite par une transformation de phase de type diffusive (« Greewood-Johnson effet ») est prise en compte dans le modèle afin d'estimer la plasticité de transformation et le comportement mécanique pendant la transformation de phase.

Les résultats obtenus par TFR ont confirmé l'existence d'une relation linéaire entre contrainte appliquée et déformation plastique induite par la transformation, lorsque la contrainte appliquée faible (c'est-à-dire inférieure à la moitié de la limite d'élasticité de la phase la plus molle). Lorsque la contrainte appliquée est plus élevée, le modèle prévoit que cette relation linéaire n'est plus valable, même si la déformation plastique de transformation augmente toujours avec la contrainte ; ceci est bon accord avec des observations expérimentales.

L'interaction entre paramètres microstructuraux (tels que texture, morphologie et taille de grains, ...) et mécaniques (contrainte de rappel, sensibilité à la vitesse de déformation, ...) a été analisée. Il a été montré que tous ces paramètres doivent être pris en compte dans l'estimation de la plasticité de transformation. L'effet de l'écrouissage cinématique de la phase mère sur l'anisotropie de déformation induite a égalament été discuté.

Par ailleurs, les résultats numériques obtenus par TFR ont été comparés à des résultats issus de modèles analytiques existants et à des mesures expérimentales. Compte tenu du bon accord entre résultats numériques et expérimentaux, les résultats obtenus par TFR

ont servi référence pour améliorer les modèles analytiques existants ; ces nouveaux modèles simplifiés s'avèrent plus précis que ceux proposés auparavant.

Mots-clefs;
Plasticité de transformation, transformée de Fourier rapide, TFR, acier, plasticité cristalline

Remerciements

Je tiens tout d'abord à remercier très sincèrement mes directeurs de thèse, Madame Brigitte Bacroix et Monsieur Renald Brenner. Je remercie Madame Brigitte Bacroix de m'avoir guidé et conseillé pendant deux ans ainsi que pour son support personnel qui a facilité ma vie en France et permis d'initier ce projet. Je remercie Monsieur Renald Brenner pour m'avoir dirigé avec patience malgré les connaissances en plasticité cristallline plutôt légères que j'avais au début de cette thèse. Il m'a consacré beaucoup de temps et son aide a été inégalable pour me permettre d'acquérir la technique de simulation numérique et de me familiariser avec la plasticité cristalline.

Cette thèse a été réalisée dans le cadre d'une collaboration entre le CNRS et Nippon Steel & Sumotomo Metal Corporation (NSSMC), Japon, de septembre 2011 à juillet 2013. Mes remerciements vont donc également aux personnes de Nippon Steel & Sumitomo Metal Corporation, qui ont permis de mettre en place cette collaboration : notamment Monsieur Shigeru Ogawa qui m'a permis d'aller étudier en France pendant deux ans, Monsieur Noriyuki Suzuki qui m'a conseillé d'étudier sous la diréction de Madame Brigitte Bacroix, Monsieur Tohru Akashi qui m'a aidé et encouragé, Monsieur Shinsuke Usui qui a été toujour mon meilleur ami avec qui j'ai partagé beaucoup de voyages en vélo à travers l'Europe et toute l'équipe des ressources humaines – Madame Miho Uchida, Madame Saya Kuroda et Monsieur Toyoji Aoki pour m'avoir également aidé financièrement, personnellement, et avoir ainsi contribué à rendre possible cette thèse.

Un grand merci va également à Ms Sibrand van der Zwaag (un de mes rapporteurs), Hao Chen et Casper Versteylen, tout trois de l'Université de Delft pour des discussions et réunions de travail efficaces sur la plasticité de transformation et ses manifestations expérimentales. Leurs conseils m'ont été essentiels pour avancer cette thèse. C'est également avec plaisir que je remercie mes rapporteurs et examinateurs pour le temps qu'ils ont accordé à la lecture de cette thèse et à l'élaboration de leur rapport.

Je souhaiterais égalament remercier mes collègues et des professeurs du LSPM qui, de près ou de loin, m'ont aidé dans ce travail, et spécialement, Hung, Oana, Chunping, Hanife et Tatiana.

En finalement, j'adresse un grand merci à ma famille et spécialement à ma femme, Masako, qui m'ont toujours fait confiance, soutenu et permis de vivre en France pendant ma thèse.

Abstract

During phase transformation in steels, when stress is applied, significant large strain can be observed even though the applied stress is much smaller than the yield stress of the softest phase. The phenomenon is called Transformation Plasticity or TRansformation Induced Plasticity (TRIP). Transformation plasticity is known to play an important role during steel producing processes. For example, during quenching process of plates, sheets, wheels and gear products, the phenomenon affects their shape and residual stresses which determines the quality of products. In this PhD thesis, a micromechanical model of crystal plasticity with phase transformation is developed. It takes advantage of the fast Fourier transform (FFT) numerical scheme for periodic media. Volume expansion along with phase transformation (Greenwood-Johnson effect) is taken into account in the model in order to evaluate the transformation plasticity and mechanical behaviour during phase transformation. The FFT results confirm linear relation between applied stress and transformation plastic strain, if the applied stress does not exceed a half the value of yield stress of the parent phase. For relatively large applied stresses, transformation plastic strain increases nonlinearly with respect to the applied stress. These results agree well with experimental ones.

The metallurgical and mechanical interactions during phase transformation are also analysed, such as texture, grain morphology, grain size, back stress effect and viscoplastic deformation effect. It is shown that they cannot be neglected for estimating transformation plasticity. Among others, the role of kinematic hardening of the parent phase on the resulting strain anisotropy is discussed.

Finally, the FFT numerical results have been compared with existing analytical models as well as experimental results. Moreover, these FFT computations have been used as references to develop new approximate analytical models. They are shown to improve on previous proposals. These new models were confirmed that they estimate well the transformation plasticity than other analytical models which have been treated in this PhD thesis.

Keywords;
Transformation plasticity, fast Fourier transform, FFT, steel, crystal plasticity

Table of Contents

Chapter 1 Introduction

In the course of the heat treatment process of steels, mechanical, thermal and metallurgical properties interact with each other. Apparently, this fact involves difficulties in modelling the complete phenomena and makes it difficult to carry out proper simulations. For example, crystallographic reconfigurations such as recrystallisation or phase transformation lead to changes of materials' mechanical properties. A description of these coupling effects is illustrated in Fig. 1.

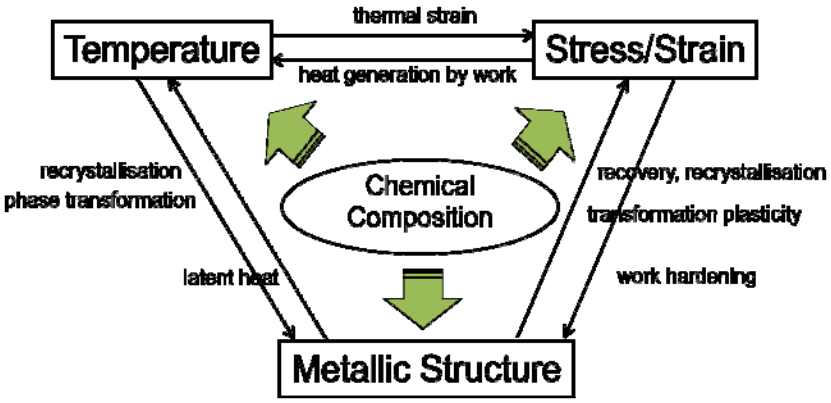

Fig. 1 Description of coupling effects during phase transformation.

As already mentioned, because the constitutive relations are dependent on temperature, deformation history, chemical composition and metallic structure including grain size or dislocation density, experimental materials data are absolutely important. With this aspect, many researchers devote themselves to measure and collect those data. Among those complex phenomena, transformation plasticity is known to be one of the most important phenomena [1] [2] [3]. However, the experimental data remain limited because of the difficulties in performing experiments as well as their cost. Besides, it is extremely difficult to distinguish between individual effects such as austenite grain size or cooling rate on transformation plasticity by experiments. Consequently, one of the aims of this PhD thesis is to investigate the influence of metallurgical parameters on transformation plasticity, especially for in the case of diffusive transformation. It is expected to give some indications on further works on this topic.

Two main mechanisms for transformation plasticity are classically invoked: (i) a

displacive mechanism (i.e. Magee effect [4]) with a shape change during transformation and (ii) a diffusive mechanism (i.e. Greenwood-Johnson effect [5]), implying nucleation and growth steps, with a volume change plastically accommodated [2]. They have been the subject of a number of experimental studies (see, among others, [6] [7] [3] [8] [9] [10] [11]).

The phenomenon is known to play a central role during phase transformation since it affects the shape and residual stresses of heat treated materials. On one hand, phenomenological models have been developed and taken into account in the frame work of finite element heat treatment simulations [12] [13] [14].

On the other hand, micromechanical modelling of transformation plasticity dates back to the pioneering theoretical work of Leblond *et al*. [15] based on a rigorous homogenisation procedure. Few years later, an approximate analytical model has been derived [16], to describe transformation plasticity due to the Greenwood-Johnson mechanism. Since then, further developments have been proposed based on this approach [17]. Besides, it is worth mentioning that a variety of mean-field models have also been developed; see, for instance [18] [19] [20]. Apart from these works, numerical micromechanical modelling has been performed, making use of the finite-element method (FEM) to study diffusional transformations. With increasing complexity, numerical investigations have first considered the case of a two-phase material with J_2 plasticity, then various nucleation rules [15] [16] [21] [22] [23], and very recently, the case of polycrystalline materials with crystalline plasticity at the slip system level, with a microstructure described by a Poisson-Voronoi tessellation [24].

In the context of classical plasticity (i.e. without solid phase transformation), an efficient numerical scheme based on fast Fourier transforms (FFT) [25] has been successfully applied to a variety of problems and constitutive relations [26] [27] [28] [29] [30]. This alternative approach to FEM allows to consider large polycrystalline aggregates with reasonable CPU time and memory allocation. Its accuracy has been discussed by confronting with FEM simulation results [31]. Besides, meshing of the microstructure is not necessary: the computation is directly made on the digital image of the material (regular grid of pixels in 2D or voxels in 3D). These features are especially convenient to consider experimental microstructural data obtained by fine-scale EBSD or X-ray diffraction contrast tomography [32] [33] [34]. By contrast to FEM, the FFT method is a periodic homogenisation scheme which makes it less general.

In the present work, we first carry out experiments for obtaining transformation plasticity data for several carbon steels. In addition, experiments on Invar metals are performed in order to confirm the Greenwood-Johnson effect by taking advantage of their small

transformation expansion. Then, we investigate the application of the FFT method in the context of plasticity induced by diffusional transformation. Following previous investigations for classical plasticity, a simple numerical scheme is derived making use of a phenomenological transformation kinetic model. The numerical model is described and compared to an exact theoretical solution in 4.1. Then, use is made of FFT reference results on representative polycrystalline aggregates for (i) a critical analysis of two existing analytical micromechanical models [16] [17] and (ii) the proposal of a new model (4.3). These analytical models are compared for different material data (transformation expansion coefficient and ratio of the yield stress of the parent and mother phases) corresponding to bainite and pearlite transformations.

Chapter 2 Literature review

2.1 Definition of transformation plasticity

During heat treatment process, the heating and cooling curves sometimes do not coincide with each other. The irreversible change in length is significant during phase transformation, which is called transformation plasticity [35]. This thermal ratcheting can be caused by even unconscious small applied stress. The phenomenon attracts both scientific and industrial interests because it affects significantly the shape and residual stress of heat treated materials.

According to the review work by Fischer *et al*. [2], Greenwood and Johnson (1965) have accounted for the mechanism of transformation plasticity in terms of volume change during phase transformation (G-J effect) [5]. After Greenwood and Johnson, many models which describe transformation plasticity have been suggested (they will be presented in details later on).

By contrast to G-J effect, there exists an alternative transformation plasticity mechanism, which is called Magee effect [4]. This mechanism is rather important for displacive phase transformation, and so, Shape Memory Alloys (SMAs). It implies a shape change. According to the Magee effect, when small stress is applied during phase transformation, particular Martensite variants are selected.

Concerning the application of these models, Miyao *et al*. [36] have taken the transformation plasticity effect into account for the heat treatment simulation of gear products, Taleb *et al*. [37] calculated the residual stresses with the effect of transformation plasticity during welding process and Fukumto *et al*. [38] have carried out the quenching simulation of helical gears with bainitic phase transformation. According to these works, it is revealed that transformation plasticity impact tremendously residual stress and product quality.

2.2 Parameters which influence the transformation plasticity

2.2.1 Pre-hardening

Taleb *et al*. [39] have carried out several experiments of transformation plasticity in order to investigate the effect of pre-deformation of 16MND5 (French norm, see Table 1) steel. The idea seems to be extremely important because, in general, heat treatment processes

are carried out just after mechanical deformation such as rolling, grinding or forging. The experimental procedure is follows. The specimens are heated up to 1100 ºC and subject to subsequent cooling down to 20 ºC to obtain bainitic or martensitic phase. The materials are subject to pre-hardening right before the phase transformation. The results show interesting phenomena.

For bainitic transformation, the pre-hardening by tension leads to positive transformation plastic strain and the pre-hardening by compression leads to negative one.

For martensitic transformation, the experimental results show totally opposite effect of pre-hardening; the pre-hardening by tension leads to negative transformation plasticity and the pre-hardening by compression leads to positive one.

These results show

Table 1 Chemical composition of 16MND5 (wt%).

C	Si	Mn	P	S	Ni	Cr	Mo	Cu	Co
0.16	0.015	1.30	0.010	0.007	0.74	0.18	0.48	0.06	0.01

2.2.2 Austenite grain size (AGS)

Nozaki *et al*. [40] elaborated the effect of AGS on transformation plasticity of SCM415 (Japanese norm, see Table 2) steel. Though they have investigated heating, cooling and cyclic temperature conditions, let us concentrate on the cooling condition. They have changed the heating temperature and holding temperature ranging from 900 ºC-5min to 1100 ºC-15min to obtain the grain size of 5 μm, 13 μm and 125 μm. The transformation types of the first two grain size cases are ferrite-pearlitic, and the second one is ferrite-bainitic. The results showed complex effect of initial grain size. In addition, there is not only dependence on grain size, but also dependence on applied stress. Despite the complexity, they concluded that the smaller the grain size, one observes the larger the transformation plastic strain. They also mentioned that the grain size effect is controlled by grain boundary sliding but the magnitude of the effect is much smaller than that of internal stress, i.e. G-J effect.

There is also a work on this topic by Boudiaf *et al*. [10] on 35NiCrMo16 steel. They have carried out not only tension test, but torsion and even biaxial loading test during martensitic phase transformation. The results of uniaxial tension tests showed that if the holding temperature is high, in other words if the grain size is large, the transformation plastic strain will be large accordingly. Alternatively, no difference has been detected for torsion tests, and the results of biaxial tests show lightly opposite results to uniaxial tension tests.

The results of uniaxial tension tests by Boudiaf *et al*. seem to be in contradiction to the results by Nozaki *et al*.. This can be explained by the difference of the applied stresses. In fact, tests by Boudiaf *et al*. were done under 92 MPa and 130 MPa equivalent stresses. By contrast, Nozaki *et al*. did tests under several applied stress value ranging from 10 MPa to 50 MPa.

To sum up, the results by Boudiaf *et al*. include the effects of both loading type (tension/torsion) and stress magnitude so that it is difficult to assert simply the effect of grain size. One can say that the grain size affects differently the transformation plasticity depending on the conditions of applied stress and loading type.

Table 2 Chemical composition of SCM415 (wt%).

C	Si	Mn	P	S	Ni	Cr	Mo	Cu	Co
0.18	0.29	0.68	0.017	0.014	0.07	1.03	0.16	0.11	-

Table 3 Chemical composition of 35NiCrMo16 (wt%).

C	Si	Mn	P	S	Ni	Cr	Mo	Cu	Co
0.35	0.29	0.48	0.21	0.011	1.81	3.78	0.27	0.17	-

2.2.3 Anisotropy

It has been also reported that the transformation plastic strain may vary according to applied stress direction, such as tension, compression and torsion. According to the work by Videau *et al*. [41], transformation plastic strain during martensitic phase transformation of Cr-Ni-Mo-Al-Ti steel by tension is the highest, torsion is a little bit smaller than that of tension and compression gives the lowest value.

By contrast, the paper by Miyao *et al*. [36] shows no significant difference between tension and compression.

2.2.4 High applied stress

As we have seen above, transformation plasticity models are often expressed as a linear relationship between applied stress and transformation plastic strain. This is confirmed by many experimental works [12] [42]. However, if the applied stress exceeds certain threshold value, the linear relation does not hold. The value is often observed to be half the value of yield stress of parent phase [5] [41]. To the author’s knowledge, no definitive explanation for this phenomenon has been provided yet.

2.3 Modelling of transformation plasticity

2.3.1 Phenomenological models

Phenomenological description of transformation plasticity can be given by a simple relation between transformation plastic strain, volume fraction of new phase and applied stress (Inoue [12] and Desalos [6] respectively), such that

$$\dot{\varepsilon}^{tp} = 2K(1-z)\dot{z}\sigma \,, \tag{1}$$

$$\dot{\varepsilon}_{ij}^{tp} = 3K(1-z)\dot{z}s_{ij} \,, \tag{2}$$

where ε^{tp} is transformation plastic strain, K is a transformation plastic coefficient, z is volume fraction of new phase and σ is applied stress.

The extended version of transformation plastic strain to multi phase transformation was proposed by the author [43]:

$$\dot{\varepsilon}_{ij}^{tp} = \sum_{I=2}^{N} 3K_I \left(\sum_{J=1}^{I-1} z_J \right) \dot{z}_I s_{ij} \,. \tag{3}$$

The transformation plastic coefficient K can be easily calculated by taking integration of the equation from transformation start point $z = 0$ to finish point $z = 1$, one obtains:

$$\varepsilon^{tp} = K\sigma \,. \tag{4}$$

In this way, the transformation plastic coefficient K can be identified with experimental results. This K value represents sensitivity of applied stress on transformation plastic strain. Typically, this value varies from 10^{-5} to 10^{-4} MPa^{-1} [1][44]. A Japanese group has been making an effort to make a data base for facilitating heat treatment simulations. The activity bore fruits of a database called MATEQ (MATerial database for Quenching process simulation) [1]. The database consists of TTT and CCT diagrams, heat conduction coefficients, density, specific heat, elastic modulus, s-s curves, temperature-elongation diagrams and transformation plasticity data (K values in equation (4)), depending on the chemical compositions. Thus, the users can assess these data by searching with steel grades (in Japanese Industrial Standards; JIS) or chemical compositions.

2.3.2 Micromechanical models

2.3.2.1 Analytical models

Greenwood and Johnson [5] have developed a model of transformation plasticity in their paper by considering volume change during phase transformation, such that

$$\dot{\varepsilon}^{tp} = \frac{5}{6\sigma_1^y} \frac{\Delta \dot{V}}{V} \sigma \,, \tag{5}$$

where σ_1^y is a yield stress of parent phase and $\Delta V/V$ is volume expansion ratio by phase transformation and σ is externally applied stress. In a similar way, Abrassart [45] suggested an equation as,

$$\dot{\varepsilon}^{tp} = \frac{1}{4\sigma_1^y}\frac{\Delta\dot{V}}{V}(3z - 2z^{\frac{3}{2}})\sigma \,. \tag{6}$$

In addition to those models, Leblond *et al*. [15] have obtained the following equation with an approximate micromechanical model.

$$\dot{\varepsilon}_{ij}^{tp} = \begin{cases} 0 \quad \text{if} \quad z \le 0.03 \\ \left(\frac{-2\beta}{\sigma_y^1}\right)\ln(z)\dot{z}\frac{3}{2}s_{ij} \quad \text{if} \quad z > 0.03 \end{cases}, \tag{7}$$

where β is a transformation expansion coefficient and s_{ij} is a deviatoric stress tensor. For the description of nonlinearity under high applied stress condition, they modified their equation as follows:

$$\dot{\varepsilon}_{ij}^{tp} = \begin{cases} 0 \quad \text{if} \quad z \le 0.03 \\ \left(\frac{-3\beta}{\sigma_y^1}\right)h\left(\frac{\Sigma^{eq}}{\Sigma^u}\right)\cdot\ln(z)\dot{z}s_{ij} \quad \text{if} \quad \xi > 0.03 \end{cases} \tag{8}$$

and

$$h\left(\frac{\Sigma^{eq}}{\Sigma^u}\right) = \begin{cases} 1 \quad \text{if} \quad \frac{\Sigma^{eq}}{\Sigma^u} \le \frac{1}{2} \\ 1 + 3.5\left(\frac{\Sigma^{eq}}{\Sigma^u} - \frac{1}{2}\right) \quad \text{if} \quad \frac{\Sigma^{eq}}{\Sigma^u} > \frac{1}{2} \end{cases}, \tag{9}$$

where the function $h(\Sigma^{eq}/\Sigma^u)$ is added to express the nonlinearity. Σ^{eq} is the applied equivalent stress and Σ^u is the yield stress of parent phase. The function is fitted with results by FEM calculations.

Thereafter, the total transformation plastic strain arising during phase transformation under small applied stress can be given by:

$$\dot{\varepsilon}_{ij}^{tp} = \int_{0.03}^{1}\left(\frac{-2\beta}{\sigma_y^1}\right)\ln(z)\,\dot{z}\frac{3}{2}s_{ij}dz \cong 0.8648\left(\frac{-2\beta}{\sigma_y^1}\right)\frac{3}{2}s_{ij} \,. \tag{10}$$

This pioneering micromechanical model is worth explaining in some details since it has been the basis of many developments.

Leblond *et al*. [15] started with the general expression of strain rate during γ/α phase transformation as a function of volume change:

$$\dot{E}^{tp} = \left\{(1-z)\left\langle\frac{\delta\varepsilon_1^p}{\delta z}\right\rangle_{V_1} + z\left\langle\frac{\delta\varepsilon_2^p}{\delta z}\right\rangle_{V_2} + \left\langle\Delta\varepsilon_{1\to2}^p\right\rangle_{F(U_n)}\right\}\dot{z} \,, \tag{11}$$

where left term denotes macroscopic plastic strain rate caused by phase transformation,

$\langle \delta\varepsilon_1^p/\delta z\rangle_{V_1}$ represents the average value through parent phase of the ratio of plastic strain increment due to volume fraction change and $\langle \Delta\varepsilon_{1\to2}^p\rangle_{F(U_n)}$ is the average value of volume expansion (contraction) over the the transformation front F weighted by its normal velocity U_n. Starting with the equation (11), 5 hypotheses have been considered.

H1. The microscopic elastic compliance tensor may be equated to the macroscopic overall elastic compliance tensor.

H2. For small or moderately high applied stresses, the γ phase is entirely plastic, but the α phase remains elastic or its plastic strain rate remains always much smaller than that of the γ phase.

H3. Both phases are ideal-plastic and obey the von Mises criterion and the Prandtl-Reuss flow rule.

H4. Correlations between $\delta\varepsilon_1^{eq}/\delta z$ and s_1 can be neglected.

H5. For small applied stresses, the average stress deviator in phase 1 is almost equal to the overall average stress deviator.

By neglecting Magee mechanism (we will discuss in the later section), i.e. $\langle \Delta\varepsilon_{1\to2}^p\rangle_{F(U_n)} = 0$, and with H2, the equation (11) can be reduced into:

$$\dot{E}^{tp} = (1-z)\,\langle\frac{\delta\varepsilon_1^p}{\delta z}\rangle_{V_1}\,\dot{z}\ . \tag{12}$$

And with H3, the equation (12) will be:

$$\dot{E}^{tp} = \frac{3(1-z)}{2\sigma_1^y}\langle\frac{\delta\varepsilon_1^{eq}}{\delta z}s_1\rangle_{V_1}\,\dot{z}\ , \tag{13}$$

If the correlations between $\delta\varepsilon_1^{eq}/\delta z$ and s_1 can be neglected (H4), equation (13) becomes:

$$\dot{E}^{tp} = \frac{3(1-z)}{2\sigma_1^y}\langle\frac{\delta\varepsilon_1^{eq}}{\delta z}\rangle_{V_1}S_1\dot{z}\ , \tag{14}$$

where

$$S_1 = \langle s_1\rangle_{V_1}\ . \tag{15}$$

Hypothesis 5 means that S_1 in equation (15) can be replaced to applied stress, such that:

$$\dot{E}^{tp} = \frac{3(1-z)}{2\sigma_1^y}\langle\frac{\delta\varepsilon_1^{eq}}{\delta z}\rangle_{V_1}S\dot{z}\ . \tag{16}$$

Then, the problem is reduced to how to calculate the term $\langle\delta\varepsilon_1^{eq}/\delta z\rangle_{V_1}$. To solve this, Leblond *et al*.[15] considered the spherical model as shown in Fig. 2.

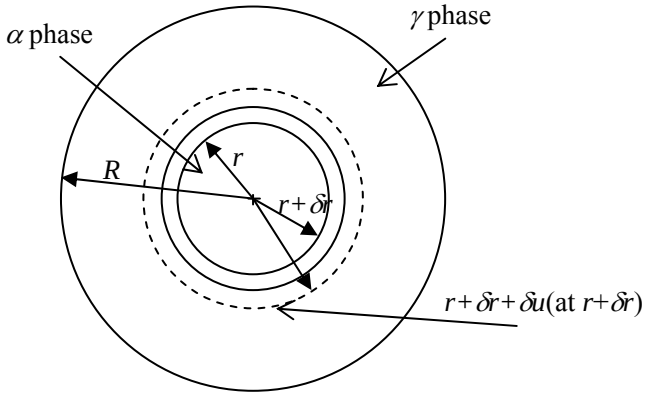

Fig. 2 Typical geometry for the evaluation of $\langle \delta\varepsilon_1^{eq}/\delta z \rangle_{V_1}$.

Since the stress applied is assumed to be small, the term $\langle \delta\varepsilon_1^{eq}/\delta z \rangle_{V_1}$ is estimated under external load free condition[1]. At the time instant t, the radii of the outer γ and inner α spheres are, respectively R and r, so that the proportion of phase 2 within the whole model is $z = r^3/R^3$. Between the time instants t and $t + \delta t$ the region comprised originally between the radii r and $r + \delta r$ is transformed into phase 2, so that z increases by the amount $\delta z = 3r^2\delta r/R^3$. Because of the positive volume change induced by the transformation, the points located originally at $r + \delta r$ come to a new location $r + \delta r + \delta u$ (at $r + \delta r$); this induces plastic deformations in the γ crust. When we introduce the spherical coordinates, such that:

$$\delta\varepsilon_{xx} = \frac{du(x)}{dx}, \qquad \delta\varepsilon_{\theta\theta} = \delta\varepsilon_{\phi\phi} = \frac{\delta u(x)}{x} , \tag{17}$$

and equilibrium condition leads:

$$\delta\varepsilon_{xx} + \delta\varepsilon_{\theta\theta} + \delta\varepsilon_{\phi\phi} = 0 , \tag{18}$$

which implies that:

$$\delta u(x) = \frac{3\beta r^2 \delta r}{x^2} , \tag{19}$$

where β is volume expansion by phase transformation.
In addition, equivalent strain is written as follows:

$$\delta\varepsilon^{eq}(x) = \left[\frac{2}{3}\left(\delta\varepsilon_{xx}^2 + \delta\varepsilon_{\theta\theta}^2 + \delta\varepsilon_{\phi\phi}^2\right)\right]^{\frac{1}{2}} = \frac{6\beta r^2 \delta r}{x^3} . \tag{20}$$

Hence, the total equivalent strain increment due to volume change can be obtained by taking overall integral of equation (20) from radii r to R, such that:

[1] The assumption will be discussed in Chapter 4.

$$\langle\frac{\delta\varepsilon_1^{eq}}{\delta z}\rangle_{V_1}=\frac{1}{\frac{4}{3}\pi(R^3-r^3)}\int_r^R\frac{6\beta r^2\delta r}{x^3}\frac{4\pi x^2dx}{3r^2\frac{\delta r}{R^3}}=-\frac{2\beta}{1-\xi}\ln(z)\ . \tag{21}$$

Then, we finally obtain the equation (7).

The validity of hypotheses H2 and H5 has been confirmed by 3D FE calculations. The model by Leblond predicts accurately transformation plastic strain [15]. In addition, Leblond [16] extends their model with strain hardening. Taleb *et al*. modified the Leblond's model as follows [17].

$$\dot{\varepsilon}_{ij}^{tp}=\begin{cases}\left(\frac{-2\beta}{\sigma_1^y}\right)\ln(z_l)\dot{\xi}\frac{3}{2}s_{ij} & \text{if} \quad z\le z_l\\ \left(\frac{-2\beta}{\sigma_1^y}\right)\ln(z)\dot{\xi}\frac{3}{2}s_{ij} & \text{if} \quad z>z_l\end{cases}\ , \tag{22}$$

and

$$z_l=\frac{\sigma_1^y}{2\beta}\frac{4\mu+3K}{9K\mu}\ , \tag{23}$$

where K and μ are balk and shear elastic moduli respectively.

The differences between Leblond's model and Taleb's model are; the threshold volume fraction value which separates into two equations, the equation when the volume fraction is under threshold value. This Taleb's modification derives from the consideration of elastic fraction at the beginning of phase transformation (in this stage, not entire parent phase undergoes plastic deformation).

Another equation is also proposed, modifying Leblond's hypothesis 5; S_1 as a decreasing function accompanied with transition of phase transformation, such that:

$$\dot{\varepsilon}_{ij}^{tp}=\begin{cases}\left(\frac{-2\beta}{\sigma_1^y}\right)\ln(z_l)\,\dot{z}(1-z^2)\frac{3}{2}s_{ij} & \text{if} \quad z\le z_l\\ \left(\frac{-2\beta}{\sigma_1^y}\right)\ln(\xi)\dot{z}(1-z^2)\frac{3}{2}s_{ij} & \text{if} \quad z>z_l\end{cases}\ . \tag{24}$$

In contrast to the Leblond's model, Nozaki *et al*. [46] have developed a model taking into account the external stress for evaluating $\langle\delta\varepsilon_1^{eq}/\delta z\rangle_{V_1}$. This model is considered to be an extension of G-J model. They obtained the following equation.

$$\varepsilon^{tp}=\frac{\Delta V}{V}\left[\frac{16}{45}\frac{\left(\sigma/\sigma_1^y\right)^2}{1-\left(\sigma/\sigma_1^y\right)^2}\right]^{\frac{1}{2}}\ . \tag{25}$$

This relation implies that the relationship between applied stress and resulting transformation plastic strain is not linear.

2.3.2.2 Numerical models

Alternative micromechanical approaches to investigate transformation plasticity were proposed by Leblond *et al.* [15] followed by Gautier *et al*. [7] and Ganghoffer *et al*. [21] by using Finite Element Method (FEM) taking into account G-J effect. They successfully reproduced transformation plasticity phenomenon arising from classical plastic strain. In these works, J_2 flow theory associated with von Mises yield criterion was adopted.

Barbe *et al*. [22][23][24] developed finite element modelling by using crystal plasticity and 3D polycrystal microstructure. It should be noted that they applied a considerable number of elements taking advantage of today's development of computer capacity.

Models by Barbe *et al*. [22][23][24] consist of crystal plasticity of f.c.c. (austenite phase) and b.c.c. (ferrite phase) and intermediate zone where both f.c.c. and b.c.c. slip systems are active. The intermediate zone is set to be thin enough. The transformation starts randomly inside the austenitic phase, and because the new grains are bigger than that of ancient grains (volume expansion), it causes plastic deformation. They obtained almost the same results relevant to equation (7).

However, the problem of this approach is that the FEM calculations require a lot of computation time as well as computer resources.

2.4 Crystal plasticity constitutive models

The summation of individual strain component, such as elastic ε_{ij}^{e}, plastic ε_{ij}^{p}, thermal ε_{ij}^{th} and transformation strain ε_{ij}^{m} gives the total strain:

$$\varepsilon_{ij} = \varepsilon_{ij}^{e} + \varepsilon_{ij}^{p} + \varepsilon_{ij}^{th} + \varepsilon_{ij}^{m} , \tag{26}$$

and its rate form reads:

$$\dot{\varepsilon}_{ij} = \dot{\varepsilon}_{ij}^{e} + \dot{\varepsilon}_{ij}^{p} + \dot{\varepsilon}_{ij}^{th} + \dot{\varepsilon}_{ij}^{m} . \tag{27}$$

The stress rate can be given by a tensor product of elastic compliance C_{ijkl} and elastic tensor rate $\dot{\varepsilon}_{kl}^{e}$ such that:

$$\dot{\sigma}_{ij} = C_{ijkl}\dot{\varepsilon}_{kl}^{e} . \tag{28}$$

By eliminating elastic strain rate $\dot{\varepsilon}_{ij}^{e}$ from equations (27) and (28), one obtains

$$\dot{\sigma}_{ij} = C_{ijkl}\left(\dot{\varepsilon}_{kl} - \dot{\varepsilon}_{kl}^{p} - \dot{\varepsilon}_{kl}^{th} - \dot{\varepsilon}_{kl}^{m}\right) . \tag{29}$$

The second term of the right side in equation (29) shows the effect of plastic strain rate. Here, the plastic strain will be expressed in the framework of crystal plasticity as follows. Plastic deformation is caused by glide of dislocations on specific planes. It is said that there are 12 slip systems for f.c.c. crystals and 48 for b.c.c.. The slip system will be active when resolved shear stress applied on the surface reaches Critical Resolved Shear Stress (CRSS) value τ_s. The resolved shear stress is given by

$$\tau^{\alpha} = p_{ij}^{\alpha}\sigma_{ij} , \tag{30}$$

where p_{ij}^{α} is a Schmid tensor of a slip surface, such that

$$p_{ij}^{\alpha} = \frac{1}{2}\left(s_i^{\alpha} m_j^{\alpha} + s_j^{\alpha} m_i^{\alpha}\right), \tag{31}$$

where s_i^{α} is slip direction and m_i^{α} is normal direction of slip surface of α slip system. The set of vectors *s* and *m* for both f.c.c. and b.c.c. materials are provided in Table 4.

Table 4 Slip systems of f.c.c. and b.c.c. metals.

(a) f.c.c.

		m	*s*
1	{111} <110>	(1, 1, 1)	(1, -1, 0)
2		(1, 1, 1)	(1, 0, -1)
3		(1, 1, 1)	(0, 1, -1)
4		(-1, 1, 1)	(1, 1, 0)
5		(-1, 1, 1)	(1, 0, 1)
6		(-1, 1, 1)	(0, 1, -1)
7		(1, -1, 1)	(1, 1, 0)
8		(1, -1, 1)	(1, 0, -1)
9		(1, -1, 1)	(0, 1, 1)
10		(1, 1, -1)	(1, -1, 0)
11		(1, 1, -1)	(1, 0, 1)
12		(1, 1, -1)	(0, 1, 1)

(b) b.c.c.

		m	s			m	s
1		(1, 1, 0)	(-1, 1, 1)	1		(1, 1, 2)	(-1, -1, 1)
2		(1, 1, 0)	(1, -1, 1)	2		(-1, -1, 2)	(1, 1, 1)
3		(-1, 1, 0)	(1, 1, -1)	3		(-1, 1, 2)	(1, -1, 1)
4		(-1, 1, 0)	(1, 1, 1)	4		(1, -1, 2)	(-1, 1, 1)
5		(1, 0, 1)	(1, 1, -1)	5		(1, 2, 1)	(-1, 1, -1)
6	{110}	(1, 0, 1)	(-1, 1, 1)	6	{112}	(-1, 2, -1)	(1, 1, 1)
7	<111>	(-1, 0, 1)	(1, -1, 1)	7	<111>	(1, 2, -1)	(-1, 1, 1)
8		(-1, 0, 1)	(1, 1, 1)	8		(-1, 2, 1)	(1, 1, -1)
9		(0, 1, 1)	(1, 1, -1)	9		(2, 1, 1)	(1, -1, -1)
10		(0, 1, 1)	(1, -1, 1)	10		(2, -1, -1)	(1, 1, 1)
11		(0, -1, 1)	(1, 1, 1)	11		(2, -1, 1)	(1, 1, -1)
12		(0, -1, 1)	(-1, 1, 1)	12		(2, 1, -1)	(1, -1, 1)
1		(1, 2, 3)	(1, 1, -1)	13		(2, 3, 1)	(1, -1, 1)
2		(-1, 2, 3)	(1, -1, 1)	14		(-2, 3, 1)	(1, 1, -1)
3		(1, -2, 3)	(-1, 1, 1)	15		(2, -3, 1)	(1, 1, 1)
4		(1, 2, -3)	(1, 1, 1)	16		(2, 3, -1)	(-1, 1, 1)
5		(2, 1, 3)	(1, 1, -1)	17		(3, 2, 1)	(-1, 1, 1)
6	{123}	(-2, 1, 3)	(1, -1, 1)	18	{123}	(-3, 2, 1)	(1, 1, 1)
7	<111>	(2, -1, 3)	(-1, 1, 1)	19	<111>	(3, -2, 1)	(1, 1, -1)
8		(2, 1, -3)	(1, 1, 1)	20		(3, 2, -1)	(1, -1, 1)
9		(1, 3, 2)	(1, -1, 1)	21		(3, 1, 2)	(-1, 1, 1)
10		(-1, 3, 2)	(1, 1, -1)	22		(-3, 1, 2)	(1, 1, 1)
11		(1, -3, 2)	(1, 1, 1)	23		(3, -1, 2)	(1, 1, -1)
12		(1, 3, -2)	(-1, 1, 1)	24		(3, 1, -2)	(1, -1, 1)

When τ^{α} equals to CRSS, the slip system activates. Let γ^{α} a strain value along α slip surface, then the plastic strain rate can be expressed as a summation of plastic shear strain rate on each slip system such that

$$\dot{\varepsilon}_{ij}^{p} = \sum_{\alpha} \dot{\gamma}^{\alpha} p_{ij}^{\alpha} \ . \tag{32}$$

Thus, we obtain the local constitutive equation of crystalline materials.

$$\dot{\sigma}_{ij} = C_{ijkl}\left(\dot{\varepsilon}_{kl} - \dot{\varepsilon}_{kl}^{th} - \dot{\varepsilon}_{kl}^{m}\right) - \sum_{\alpha} \dot{\gamma}^{\alpha} C_{ijkl} p_{kl}^{\alpha} \ , \tag{33}$$

$$\begin{cases} \tau^{\alpha} = g^{\alpha} \\ \tau^{\alpha} < g^{\alpha} \end{cases} \quad \text{with} \quad \begin{matrix} \dot{\gamma}^{\alpha} \geq 0 \\ \dot{\gamma}^{\alpha} = 0 \end{matrix} . \tag{34}$$

2.4.1 Hardening law expressed by accumulation of shear strain

Because materials hardening by plastic deformation, the evolution of CRSS of α slip system is considered to be associated with shear strain rate [47], such that

$$\dot{g}^{\alpha} = \sum_{\beta} h^{\alpha\beta} \left| \dot{\gamma}^{\beta} \right| , \tag{35}$$

where $h^{\alpha\beta}$ is hardening coefficient. If $\alpha = \beta$, $h^{\alpha\beta}$ is called self hardening. Otherwise, it is called latent hardening. If $h^{\alpha\beta}$ is zero, the model describes elasto-perfect plastic material. Many proposals have been made for the expression of $h^{\alpha\beta}$, for instance, according to a phenomenological low, the hardening matrix has been expressed by Peirce *et al*. [48] as:

$$h^{\alpha\alpha} = h = H_0 \operatorname{sech}^2 \left[\frac{H_0 \sum_{\beta} \gamma^{\beta}}{\tau_s - \tau_0} \right] , \tag{36}$$

$$h^{\alpha\beta} = qh + (1 - q) h \delta_{\alpha\beta} , \tag{37}$$

where H_0 is a coefficient, τ_0 is an initial yield stress value and τ_s is a saturate stress value. The parameter q takes values from 1.0 to 1.4 depending on the material.

2.4.2 Hardening law expressed by dislocation density

The well-known model to describe the relationship between hardening and dislocation density has been introduced by Bailey and Hirsch [49]:

$$\tau = \tau_y + a \mu \tilde{b} \sqrt{\rho} , \tag{38}$$

where τ is resolved shear stress, τ_y is initial critical resolved shear stress, a is a dimensionless constant, μ is Young's modulus and $\tilde{b}$ is magnitude of Bergers vector. The CRSS can be expressed as:

$$g^{\alpha} = \tau_y + a \mu \tilde{b} \sqrt{\sum_{\beta} d^{\alpha\beta} \rho^{\beta}} , \tag{39}$$

where $d^{\alpha\beta}$ denotes effect of each dislocation density ρ^{β} on g^{α}. The rate form of equation (39) is:

$$\dot{g}^{\alpha} = \frac{a \mu \tilde{b} \sum_{\beta} d^{\alpha\beta} \dot{\rho}^{\beta}}{2 \sqrt{\sum_{\beta} d^{\alpha\beta} \rho^{\beta}}} . \tag{40}$$

Tabourot *et al*. [50] used a model initially proposed by Mecking and Estrin [51]. In this model, dislocation evolution is expressed by the sum of production and annihilation

terms.

$$\dot{\rho}^{\alpha} = \frac{1}{\tilde{b}}\left(\sqrt{\frac{\sum_{\beta} a^{\alpha\beta}\rho^{\beta}}{K}} - 2y_c\rho^{\alpha}\right)|\dot{\gamma}^{\alpha}| \,. \tag{41}$$

The interaction matrix $a^{\alpha\beta}$ takes the values shown in Table 5 [50]. In addition, they considered that the $d^{\alpha\beta}$ equals to unity. By contrast, Franciosi and Zaoui [52] take $d^{\alpha\beta}$ as the same value as $a^{\alpha\beta}$ which is shown in Table 6. If we associate the matrix with the order of slip system written in Table 4, the Table 6 can also be expressed as Table 7.

Table 5 Interaction coefficients.

$a^{\alpha\beta} = a^0 = 0.2$	if $\alpha = \beta$
$a^{\alpha\beta} = a^1 = 0.3$	if α collinear/coplanar with β if g^{α} perpendicular to g^{β}
$a^{\alpha\beta} = a^2 = 0.4$	if α and β form a junction
$a^{\alpha\beta} = a^4 = 1.0$	if α and β form a Lomer-Cottrell lock

Table 6　Interaction coefficients by Franciosi-Zaoui.

	A2	A3	A6	B2	B4	B5	C1	C3	C5	D1	D4	D6
A2	SH^{a0}	$Copl^{a1}$	$Copl^{a1}$	CS^{a1}	GJ^{a2}	GJ^{a2}	HL^{a1}	GJ^{a2}	LC^{a3}	HL^{a1}	LC^{a3}	GJ^{a2}
A3		SH^{a0}	$Copl^{a1}$	GJ^{a2}	HL^{a1}	LC^{a3}	GJ^{a2}	CS^{a1}	GJ^{a2}	LC^{a3}	HL^{a1}	GJ^{a2}
A6			SH^{a0}	GJ^{a2}	LC^{a3}	HL^{a1}	LC^{a3}	GJ^{a2}	HL^{a1}	GJ^{a2}	GJ^{a2}	CS^{a1}
B2				SH^{a0}	$Copl^{a1}$	$Copl^{a1}$	HL	LC	GJ	HL	GJ	LC
B4					SH^{a0}	$Copl^{a1}$	LC	HL	GJ	GJ	CS	GJ
B5						SH^{a0}	GJ	GJ	CS	LC	GJ	HL
C1							SH^{a0}	$Copl^{a1}$	$Copl^{a1}$	CS	GJ	GJ
C3			Sym.					SH^{a0}	$Copl^{a1}$	GJ	HL	LC
C5									SH^{a0}	GJ	LC	HL
D1										SH^{a0}	$Copl^{a1}$	$Copl^{a1}$
D4											SH^{a0}	$Copl^{a1}$
D6												SH^{a0}

SH : Self hardening (a^0).

Copl : Coplanar syst. (a^1).

CS : Colinear syst. (cross slip) (a^1).

HL : Hirth Lock syst. Pair with normal slip directions (a^1).

GJ : Systems pair leading to Glissile junctions formation (a^2).

LC : Systems pair leading to Lomer-Cottrell sessile locks formation (a^3).

$a^3 > a^2 > a^1 > a^0$.

Table 7 Interaction coefficients by Franciosi-Zaoui associated with the order in Table 4.

	1(A2)	2(A3)	3(A6)	4(C1)	5(C3)	6(C5)	7(B2)	8(B4)	9(B5)	10(D1)	11(D4)	12(D6)
1(A2)	h^0	h^1	h^1	h^3	h^4	h^4	h^4	h^5	h^2	h^4	h^2	h^5
2(A3)		h^0	h^1	h^4	h^2	h^5	h^3	h^4	h^4	h^4	h^5	h^2
3(A6)			h^0	h^4	h^5	h^2	h^4	h^2	h^5	h^3	h^4	h^4
4(C1)				h^0	h^1	h^1	h^5	h^4	h^2	h^5	h^2	h^4
5(C3)					h^0	h^1	h^2	h^4	h^5	h^4	h^4	h^3
6(C5)						h^0	h^4	h^3	h^4	h^2	h^5	h^4
7(B2)							h^0	h^1	h^1	h^5	h^4	h^2
8(B4)			Sym.					h^0	h^1	h^2	h^4	h^5
9(B5)									h^0	h^4	h^3	h^4
10(D1)										h^0	h^1	h^1
11(D4)											h^0	h^1
12(D6)												h^0

SH : Self hardening (h^0).
Copl : Coplanar syst. (h^1).
CS : Colinear syst. (cross slip) (h^3).
HL : Hirth Lock syst. Pair with normal slip directions (h^2).
GJ : Systems pair leading to Glissile junctions formation (h^4).
LC : Systems pair leading to Lomer-Cottrell sessile locks formation (h^5).

With these models, hardening parameter and dislocation density are directly connected.

2.4.2.1 Dislocation density evolution models [53]

Dislocation density, in general, can be divided into statistically stored dislocation density (SS dislocation density) and geometrically necessary dislocation density (GN dislocation density). SS dislocation density represents the stored dislocations which are trapped at obstacles like grain boundaries or precipitations. On the other hand, GN dislocation density introduced by Ashby [54] is related to elastic incompatibility caused by plastic strain gradients.

Statistically stored dislocation density model [55]

The relation between slip strain and shear stress is expressed in Fig. 3.

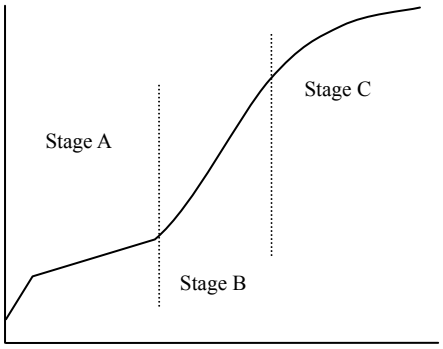

Fig. 3 Work hardening specification of single crystals.

In stage A, the slip can easily occur because dislocation density is low. Stage B represents linear hardening stage where dislocation density augments. And stage C represents dynamic recovery caused by thermally activated dislocation annihilation, where subgrains are formed. If we classify the dislocation into mobile and sessile (static) one, we can formulate these dislocations as:

$$\begin{aligned} \dot{\rho}_m^\alpha &= \dot{\gamma}^\alpha \left(\frac{g_s}{\tilde{b}^2} \frac{\rho_i^\alpha}{\rho_m^\alpha} - g_m \rho_m^\alpha - \frac{g_i}{\tilde{b}} \sqrt{\rho_i^\alpha} \right) , \\ \dot{\rho}_i^\alpha &= \dot{\gamma}^\alpha \left(g_m \rho_m^\alpha - \frac{g_i}{\tilde{b}} \sqrt{\rho_i^\alpha} - g_i \rho_i^\alpha \right) , \end{aligned} \tag{42}$$

where g_s, g_m, g_i and g_r are the parameters of: dislocation loop emitted from dislocation source, immobilisation of mobile dislocation density in stage A, immobilisation of mobile dislocation density in stage B and dynamic recovery, respectively.

Self-organisation model [56]

Walgraef and Anifantis have divided the creation of dislocation into slow $\dot{\rho}_S$ and fast $\dot{\rho}_F$ ones. They assumed that these two dislocation population obey the following diffusion equations:

$$\begin{aligned} \dot{\rho}_S^\alpha + \nabla \cdot (-M_S \nabla \mu_S) &= a - b\rho_S^2 - c\rho_S^3 - \beta \rho_S + \gamma \rho_F \rho_S^2 , \\ \dot{\rho}_F^\alpha + \nabla \cdot (-D \nabla_x \rho_F) &= \beta \rho_S - \gamma \rho_F \rho_S^2 , \end{aligned} \tag{43}$$

where a, b, c represent creation and annihilation rates of slow distribution; $\beta \rho_S$ is the rate of fast dislocations production liberated by the applied stress when it surpasses a threshold value; and γ corresponds to the pinning rate of fast moving dislocations by practically immobile dipoles; M_S the mobility tensor and μ_s the chemical potential-like variable; D is of the order of the thermal diffusivity below the threshold stress and increasing rapidly to its maximum value when it surpasses the threshold stress. The

numerical solution of this kind of problem is given by [57].

Geometrically necessary dislocation density model [58]

When there are several dislocations inside a Burgers circuit, the net Burgers vector can be obtained by taking integral along the path, such that

$$\boldsymbol{B} \equiv \oint_l \gamma \cdot d\boldsymbol{l} = \int_S \boldsymbol{\alpha} \cdot \boldsymbol{n} dS \ . \tag{44}$$

α is defined as follows.

$$\boldsymbol{\alpha} = -\mathrm{curl}\, \gamma \ . \tag{45}$$

This is dislocation density tensor. Thus, symmetric part of $\boldsymbol{\alpha}$ is:

$$\boldsymbol{\eta} = -(\mathrm{curl}\, \boldsymbol{\alpha}^T)_S \ , \tag{46}$$

where η is strain incompatibility tensor, which can express almost all the crystal defect. Dividing by Burgers vector,

$$\boldsymbol{\alpha_G} \equiv \frac{\boldsymbol{\alpha}}{\tilde{b}} = -\mathrm{curl} \frac{\boldsymbol{\gamma}}{\tilde{b}} \ , \tag{47}$$

where α_G is generalised GN dislocation density.

If we consider the plane which is set on the slip surface and slip tensor $\boldsymbol{\gamma}$ on the local coordinate, non-zero component of $\boldsymbol{\gamma}$ is only γ_{12}. Then the component of equation (47) will be:

$$\rho_{G_S} \equiv \alpha_{G11} = \frac{1}{\tilde{b}} \frac{\partial \gamma}{\partial x_3} \ , \qquad \rho_{G_e} \equiv \alpha_{G13} = \frac{1}{\tilde{b}} \frac{\partial \gamma}{\partial x_1} \ , \tag{48}$$

where ρ_{G_S} and ρ_{G_e} are screw dislocation density and edge dislocation density respectively.

2.4.2.2 Constitutive plastic flow rules

Many models for calculating $\dot{\gamma}^\alpha$ have been proposed suggested. Among those, we introduce three models by “Hutchinson [59]”, “Anand-Kothari [60]” and “Hutchinson [60], Peirce and Asaro [48], Pan and Rice [61]” expressed as follows.

Hutchinson model (Elastplastic)

Model by Hutchinson is a rate-independent crystal plasticity model. For such a case, during elastoplastic deformation, the resolved shear stress τ^α equals to CRSS (consistency condition) such that,

$$|\tau^\alpha| = \left| p_{ij}^\alpha \sigma_{ij} \right| = g^\alpha \ . \tag{49}$$

The rate form of equation (49) reads:

$$\dot{\tau}^\alpha = \mathrm{sgn}(\tau^\alpha) \dot{g}^\alpha \ . \tag{50}$$

For the small deformation problems, equation エラー! 参照元が見つかりません。 can be rewritten as:

$$\dot{\sigma}_{ij} p_{ij}^{\alpha} = \sum_{\beta} h^{\alpha\beta} \dot{\gamma}^{\beta} \ . \tag{51}$$

Because the plastic strain is a summation of slip rate on each slip system $\dot{\varepsilon}_{ij}^{p} = \sum_{\alpha} p_{ij}^{\alpha} \dot{\gamma}^{\alpha}$, the equation (29) reads:

$$\begin{aligned} \dot{\sigma}_{ij} p_{ij}^{\alpha} &= C_{ijkl}\left(\dot{\varepsilon}_{kl} - \dot{\varepsilon}_{kl}^{th} - \dot{\varepsilon}_{kl}^{m}\right) p_{ij}^{\alpha} - \sum_{\beta} p_{ij}^{\alpha} C_{ijkl} p_{kl}^{\beta} \dot{\gamma}^{\beta} \\ &= \sum_{\beta} h^{\alpha\beta} \dot{\gamma}^{\beta} \ , \end{aligned} \tag{52}$$

and thus,

$$C_{ijkl}\left(\dot{\varepsilon}_{kl} - \dot{\varepsilon}_{kl}^{th} - \dot{\varepsilon}_{kl}^{m}\right) p_{ij}^{\alpha} = \sum_{\beta} \dot{\gamma}^{\beta} \left(h^{\alpha\beta} + p_{ij}^{\alpha} C_{ijkl} p_{kl}^{\beta}\right) \ . \tag{53}$$

Now, we introduce a matrix $X^{\alpha\beta}$ for a combination of active slip systems α and β as

$$X^{\alpha\beta} = h^{\alpha\beta} + p_{ij}^{\alpha} C_{ijkl} p_{kl}^{\beta} \ . \tag{54}$$

Then, equation (32) can be rewritten as follows.

$$\sum_{\beta} \dot{\gamma}^{\beta} X^{\alpha\beta} = C_{ijkl}\left(\dot{\varepsilon}_{kl} - \dot{\varepsilon}_{kl}^{th} - \dot{\varepsilon}_{kl}^{m}\right) p_{ij}^{\alpha} \ . \tag{55}$$

Let $Y^{\alpha\beta}$ an inverse matrix of $X^{\alpha\beta}$, such that

$$Y^{\alpha\beta} = \left(X^{\alpha\beta}\right)^{-1} \ . \tag{56}$$

Then, the set of active slip system can be chosen as

$$\dot{\gamma}^{\alpha} = f_{ij}^{\alpha}\left(\dot{\varepsilon}_{ij} - \dot{\varepsilon}_{ij}^{th} - \dot{\varepsilon}_{ij}^{m}\right) , \quad \text{where} \quad f_{ij}^{\alpha} = \sum_{\beta} Y^{\alpha\beta} C_{ijkl} p_{kl}^{\beta} \ . \tag{57}$$

It is required that the matrix $X^{\alpha\beta}$ is non-singular. For this reason, the maximum number of active slip system, i.e. rank of matrix $X^{\alpha\beta}$, is limited to 5. From equation (57), we can find the values of shear strain rate, which depend on the prescribed strain rate or stress rate.

Anand-Kothari model (Elastoplastic)

Anand and Kothari have developed a rate-independent theory for finding a unique set of shear strain rates. In this theory, they introduced singular value decomposition (SVD) for obtaining inverse or pseudo inverse of the following matrix $A^{\alpha\beta}$.

$$A^{\alpha\beta} = h^{\alpha\beta} + \text{sign}(\tau^{\alpha})\text{sign}\left(\tau^{\beta}\right) p_{ij}^{\alpha} C_{ijkl}\left(\text{sym}(C) p_{kl}^{\beta}\right) , \tag{58}$$

where C is right Cauchy-Green tensor. For small deformation problem, C is a unit tensor. If we define b^α as

$$b^\alpha = |\tau^\alpha| - g^\alpha \ . \tag{59}$$

When the continuum material is subjected to plastic deformation, the yield surface deforms along with the local stress field. In this case, following equation should be satisfied at any local points.

$$\sum_\beta A^{\alpha\beta} x^\beta = b^\alpha \ . \tag{60}$$

The vector x^β appears in equation will be a solution of shear strain rate. Although, as is explained in the previously, there exists the cases that the matrix $A^{\alpha\beta}$ to be singular. To avoid this problem, Anand and Kothari introduced SVD technique to obtain pseudo inverse matrix. Matrix A can be factorised in the following form.

$$A = Q_1 \Sigma Q_2^T \ , \quad \text{where} \quad \Sigma = \mathrm{diag}(\sigma_i) \ . \tag{61}$$

Then we define A^+,

$$A^+ = Q_2 \Sigma^+ Q_1^T \quad \text{where} \quad \Sigma^+ = \mathrm{diag}(\sigma_i^+)$$
$$\text{and} \quad \sigma_i^+ = \begin{Bmatrix} 1/\sigma_i & \text{for} \quad \sigma_i > 0 \\ 0 & \text{for} \quad \sigma_i = 0 \end{Bmatrix} \ . \tag{62}$$

Here, pseudo solution of equation (60) can be obtained by following equation.

$$x^+ = A^+ b \ . \tag{63}$$

This solution is much more robust than directly taking inverse of matrix *A*. In addition, there is no limitation of the number of active slip systems.

Hutchinson-Peirce and Asaro-Pan and Rice model (Elasto-Viscoplastic)

In contrast to the former two methods, this model is rate-dependent, i.e. viscoplastic model. According to this model, every single slip system is active. In this case, the slip rate is given by following equation:

$$\dot{\gamma}^\alpha = \dot{\gamma}_0 \left(\frac{\tau^\alpha}{g^\alpha}\right) \left|\frac{\tau^\alpha}{g^\alpha}\right|^{\frac{1}{m}-1} \ . \tag{64}$$

Though its simplicity, the equation (64) causes numerical instability when m tends to 0. To avoid this numerical instability, Peirce *et al*. [48] proposed the rate tangent method as follows.

Presume that the plastic strain increment linearly changes its value with θ ($0 \leq \theta \leq 1$) during one step such that

$$\Delta\gamma^\alpha = \Delta t[(1-\theta)\dot{\gamma}_t^\alpha + \theta \dot{\gamma}_{t+\Delta t}^\alpha] \ . \tag{65}$$

Then the equation (33) can be transformed as follows:

$$\dot{\sigma}_{ij} = C^{\tan}_{ijkl}\dot{\varepsilon}_{kl} - \dot{P}^{\tan}_{ij} \ , \tag{66}$$

$$\dot{P}^{tan}_{ij} = \sum_{\alpha} \dot{f}^{\alpha} R^{\alpha}_{ij} \ , \tag{67}$$

$$C^{\tan}_{ijkl} = C_{ijkl} - \sum_{\alpha} R^{\alpha}_{ij} F^{\alpha}_{kl} \ , \tag{68}$$

$$F^{\alpha}_{ij} = \sum_{\beta} M_{\alpha\beta} Q^{\beta} \ , \tag{69}$$

$$\dot{f}^{\alpha} = \sum_{\beta} M_{\alpha\beta} \dot{\gamma}^{\beta}_{t} \ , \tag{70}$$

$$R^{\alpha}_{ij} = C_{ijkl} p^{\alpha}_{kl} \ , \tag{71}$$

$$Q^{\beta}_{ij} = \frac{\theta \Delta t \dot{\gamma}^{\beta}_{t}}{m\tau^{\beta}} q^{\beta}_{ij} \ , \quad q^{\beta}_{ij} = C_{ijkl} p^{\beta}_{kl} \ , \tag{72}$$

$$M_{\alpha\beta} = N^{-1}_{\alpha\beta} \ , \quad N_{\alpha\beta} = \delta_{\alpha\beta} + \frac{\theta \Delta t \dot{\gamma}^{\alpha}_{t}}{m} \left\{ \frac{q^{\alpha}_{ij} p^{\beta}_{ij}}{\tau} + \frac{h^{\alpha\beta}}{g^{\alpha}} \operatorname{sgn}\left(\tau^{\beta}\right) \right\} . \tag{73}$$

By this rate tangent method, one can take a large increment without numerical instability.

2.5 Thermal and transformation strains

Temperature change and phase transformation cause volumetric dilatation. These eigenstrains are called thermal strain and transformation strain respectively. In a microscopic view, it can be anisotropic but in mesoscopic or macroscopic point of view, it can be considered as isotropic if the material has overall isotropy. Here we'll take the position that those strains are isotropic. In this case, thermal and transformation strain rates can be written as follows.

$$\dot{\varepsilon}^{th}_{ij} = \alpha \dot{T} \delta_{ij} \quad , \qquad \dot{\varepsilon}^{m}_{ij} = \beta \dot{\xi} \delta_{ij} \ , \tag{74}$$

where $\dot{\varepsilon}^{th}_{ij}$ is thermal strain rate, α is a linear thermal expansion coefficient, $\dot{\varepsilon}^{m}_{ij}$ is transformation strain rate, β is a transformation expansion coefficient. Both coefficients, which are dependent on temperature and chemical composition, can be identified by experiments. For example Jablonka [62] empirically formulated the density equation of carbon steels for austenite, ferrite and cementite phases.

$$\rho^{\alpha}_{Jablonka} = (7875.96 - 0.297T - 5.62 \times 10^{-5} T^2) \times (1 - 2.62 \times 10^{-2} C_C) \ , \tag{75}$$

$$\rho^{\gamma}_{Jablonka} = (8099.79 - 0.506T) \times (1 - 1.46 \times 10^{-2} C_C) \ , \tag{76}$$

$$\rho^{Fe_3C}_{Jablonka} = 7686.45 - 6.63 \times 10^{-2} T - 3.12 \times 10^{-4} T^2 \ . \tag{77}$$

C_C denotes carbon content in percent. In addition to the equations by Jablonka, Miettinen [63] has expanded these equations for other chemical contents starting with following

pure iron density.

$$\rho_{Fe}^{\alpha} = 7875.96 - 0.297T - 5.62 \times 10^{-5}T^2 \,, \tag{78}$$

$$\rho_{Fe}^{\gamma} = 8099.79 - 0.506T \,. \tag{79}$$

The final forms of the steel density depending on chemical composition are:

$$\begin{aligned}\rho^{\alpha} = \rho_{Fe}^{\alpha} &+ (-206.35 + 0.00778T + 1.472 \times 10^{-6}T^2)C_C^{\alpha} \\ &+ (-8.58 + 1.229 \times 10^{-3}T + 0.852 \times 10^{-7}T^2 \\ &+ 0.018367C_{Cr}^{\alpha})C_{Cr}^{\alpha} \\ &+ (-0.22 - 0.470 \times 10^{-3}T - 1.855 \times 10^{-7}T^2 \\ &+ 0.104608C_{Ni}^{\alpha})C_{Ni}^{\alpha} - 36.86C_{Si}^{\alpha} - 7.24C_{Mn}^{\alpha} + 30.78C_{Mo}^{\alpha} \,,\end{aligned} \tag{80}$$

$$\begin{aligned}\rho^{\gamma} = \rho_{Fe}^{\gamma} &+ (-118.26 + 0.00739T)C_C^{\gamma} \\ &+ \left(-7.59 + 3.422 \times 10^{-3}T - 5.388 \times 10^{-7}T^2\right. \\ &\left. - 0.014271C_{Cr}^{\gamma}\right)C_{Cr}^{\gamma} \\ &+ \left(1.54 + 2.267 \times 10^{-3}T - 11.26 \times 10^{-7}T^2\right. \\ &\left. + 0.062642C_{Ni}^{\gamma}\right)C_{Ni}^{\gamma} - 68.24C_S^{\gamma} - 6.01C_{Mn}^{\gamma} + 12.45C_{Mo}^{\gamma} \,.\end{aligned} \tag{81}$$

Pearlite phase is a mixed phase of ferrite and cementite. In this case, we start with the mixture of pure ferrite and pure cementite, and then consider the effect of other chemical component than carbon. Let *X* volume fraction of ferrite phase, the density of the mixture phase will be as follows:

$$\rho = \frac{1}{\frac{X}{\rho^{\alpha}} + \frac{1-X}{\rho^{Fe_3C}}} \,. \tag{82}$$

Arimoto [44] suggested martensite density equation calculated by lattice constant such that

$$\rho^{M} = 7870.98 - 168.2C_C + 7.92C_C^2 \,. \tag{83}$$

The relation between thermal strain and density is follows

$$\varepsilon^{th} = \alpha \Delta T = \sqrt[3]{\frac{\rho(T)}{\rho(T + \Delta T)}} - 1 \,, \tag{84}$$

where ΔT is temperature change from reference state. In the same manner, the transformation strain can be expressed as follows (e.g. austenite-ferrite transformation).

$$\varepsilon^{m} = \beta = \sqrt[3]{\frac{\rho^{\gamma}}{\rho^{\alpha}}} - 1 \,. \tag{85}$$

2.6 Kinetic models of phase transformation

In the course of hot steel rolling and subsequent heat treatment or cold rolling processes,

following phases are concerned: austenite, ferrite, pearlite (ferrite + cementite), bainite and martensite. For example, a casted slab is reheated in reheating furnace and reduced its thickness by hot rolling. Then, it is cooled down with certain cooling rate according to required quality. Between reheating furnace and cooling equipment, the phase of the material is normally austenite. During cooling process, the phase transforms from austenite to ferrite, pearlite, bainite and martensite according to the cooling rate and chemical composition. The cooling rate and chemical compositions are carefully defined according to the customers' demand.

The transformation can be divided into two types: diffusive and non-diffusive (displacive). The former case includes ferritic, pearlitic and bainitic (controversial) transformations and the latter includes martensitic transformation. The transformation is expressed by the volume fraction of new phase ξ $(0 \leq \xi \leq 1)$. In this case, mathematical models for both diffusive and non-diffusive transformation are proposed.

2.6.1 Kinetics and formulation (diffusive transformation)

Firstly, we introduce Johnson-Mehl [64] relation. Diffusive transformation is caused by thermally activated atoms which traverse among atoms of parent (ancient) phase or daughter (new) phase. The phenomenon is often expressed by the difference of Gibbs free energy of both phases. Suppose that the daughter phase has circle shape in the unit volume of parent phase and let G the glowing velocity of daughter phase toward the normal direction of its surface A. In this case, the volume fraction increment of daughter phase is:

$$\dot{z} = GA \ . \tag{86}$$

In order to identify the surface A, Johnson and Mehl have introduced the concept of extended volume V_e and extended area A_e. According to this notion, nucleation occurs everywhere in the specimen and the daughter phase grows without any obstacles, namely

$$V_e = GA_e \ . \tag{87}$$

If the nuclei are randomly spread, we obtain:

$$A = (1 - z)A_e \ . \tag{88}$$

Using equations (87) and (88), integration of equation (86) will be:

$$z = 1 - \exp(-V_e) \ . \tag{89}$$

The daughter phase which has been germinated at the time τ, has volume of $4\pi G^3(t - \tau)^3/3$ at the time t. Let the germination speed $\dot{N}$, the extended volume V_e will be:

$$V_e = \int_0^t \frac{4}{3}\pi G^3 (t - \tau)^3 \dot{N} d\tau \ . \tag{90}$$

Here, $\dot{N}$ and G are function of Gibbs free energy. Gibbs free energy is a function of

stress, temperature and internal variables such as plastic strain ε_{ij}^{p} or back stress a_{ij}. If we consider that the effect of stress and temperature is much more significant than that of other, and let the effect $f_T(T)$ and $f_S(\sigma)$ respectively, we have:

$$z = 1 - \exp\left\{-\int_0^t f_T(T) f_S(\sigma)(t-\tau)^3 d\tau\right\} . \tag{91}$$

The functions $f_T(T)$ and $f_S(\sigma)$ can be measured by TTT diagrams under constant stress field. If one defines $f_S(\sigma) = 1$ under stress free condition, equation (91) will be:

$$z = 1 - \exp\left\{-\frac{1}{4} f_T(T) t^4\right\} . \tag{92}$$

Following enhanced equation of (92) is also suggested, which called KJMA (Kolmogorov-Johnson-Mehl-Avrami) equation [44]:

$$z = 1 - \exp(-bt^n) . \tag{93}$$

The materials parameter b and n are also identified by TTT diagrams.

2.6.2 Kinetics and formulation (non-diffusive transformation)

Because the research subject of this thesis is mainly on transformation plasticity during diffusive phase transformation, non-diffusive transformation is only briefly discussed. Non-diffusive transformation (martensitic transformation) starts when the temperature becomes lower than M_S point. M_S point is a function of chemical component and stress. It is clear that the phase is already transformed to ferrite or so, the martensitic transformation does not occur. It means that the intense cooling is necessary to obtain martensite phase. We just introduce the model by Koistinen-Marburger [65], or Magee [66] such that,

$$z = 1 - \exp[-\phi(M_S - T)] , \tag{94}$$

where ϕ is a material parameter. Oh and Inoue modified the equation [67] for the purpose of introducing stress effect as follows.

$$z = 1 - \exp\left[-\phi(M_S - T) + \psi_{ij}\sigma_{ij}\right] , \tag{95}$$

where ψ_{ij} is also a material parameter which is calculated by Gibbs free energy.

2.6.3 Inheritance of crystallographic orientation

The crystallographic orientation of the transformed phase is not random. There are certain relations between ancient phase and product phase orientations. These relations are more significant for martensitic phase transformation than ferritic phase transformation. However, it is reported that these relations are still valid for ferritic phase transformation [68]. The relations are also affected by applied stress and magnetic field [69] [70] [71]. In this section, three relations will be introduced, namely; Bain [72], Kurdjumov-Sachs [73]

and Nishiyama-Wasserman [74] [35]. The comparison of these models in a pole figure is shown in Fig. 4.

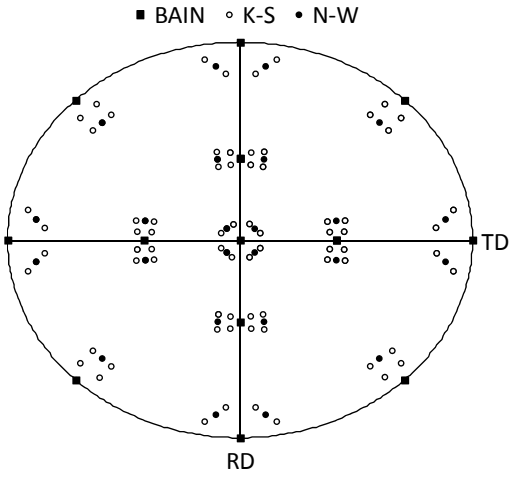

Fig. 4 Bain, K-S and N-W variants plotted on $[001]_\gamma$ pole figure.

2.6.3.1 Bain relation

Bain [72] introduced atomic corresponding model during phase transformation from austenitic phase into martensitic, bainitic or ferritic phase. After this correspondence, the transformed lattice is subject to compression along with $[001]$ direction. Let the lattice parameter of austenite and martensite be a_A and a_M, then the lattice deformation matrix can be denoted as:

$$\boldsymbol{B} = \begin{pmatrix} \sqrt{2}a_M/a_A & 0 & 0 \\ 0 & \sqrt{2}a_M/a_A & 0 \\ 0 & 0 & a_M/a_A \end{pmatrix}. \tag{96}$$

Then schematic illustration of Bain relation is shown in Fig. 5.

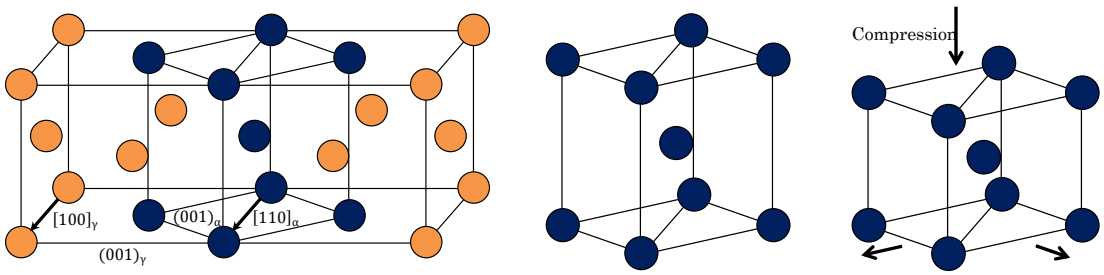

(a) Configuration of corresponding atoms deformation (b) b.c.c. lattice (c) Lattice

Orange points: f.c.c., Blue points: b.c.c.

Fig. 5 Bain relation for f.c.c to b.c.c. phase transformation.

The rotation matrix in general can be expressed by the invariants of the rotation (axis $[n_1 n_2 n_3]$ and angle θ):

$$V_i = \begin{pmatrix} n_1^2(1-\cos\theta)+\cos\theta & n_1 n_2(1-\cos\theta)-n_3\sin\theta & n_1 n_3(1-\cos\theta)+n_2\sin\theta \\ n_2 n_1(1-\cos\theta)+n_3\sin\theta & n_2^2(1-\cos\theta)+\cos\theta & n_2 n_3(1-\cos\theta)-n_1\sin\theta \\ n_3 n_1(1-\cos\theta)-n_2\sin\theta & n_3 n_2(1-\cos\theta)+n_1\sin\theta & n_3^2(1-\cos\theta)+\cos\theta \end{pmatrix}. \quad (97)$$

In this case, crystallographic rotation matrix (without Bain deformation) is defined by adopting 45° rotation about the axis $[001]$ such that:

$$\boldsymbol{R_B} = \begin{pmatrix} 1/\sqrt{2} & -1/\sqrt{2} & 0 \\ 1/\sqrt{2} & 1/\sqrt{2} & 0 \\ 0 & 0 & 1 \end{pmatrix}. \quad (98)$$

It is known that there are 3 variants for Bain relation. For the rest of 2 variants, they are easily found by applying rotating axes $[100]$ and $[010]$:

$$\boldsymbol{R_B^{(2)}} = \begin{pmatrix} 1 & 0 & 0 \\ 0 & 1/\sqrt{2} & -1/\sqrt{2} \\ 0 & 1/\sqrt{2} & 1/\sqrt{2} \end{pmatrix}, \quad (99)$$

$$\boldsymbol{R_B^{(3)}} = \begin{pmatrix} 1/\sqrt{2} & 0 & -1/\sqrt{2} \\ 0 & 1 & 0 \\ 1/\sqrt{2} & 0 & 1/\sqrt{2} \end{pmatrix}, \quad (100)$$

where the superscripts denote variant number.

2.6.3.2 K-S relation

Kurdjumov and Sachs [73] proposed another crystallographic relation [68] expressed in Fig. 6, which is called Kurdjumov-Sachs relation or K-S relation. The parallel surface is $\{111\}_\gamma // \{110\}_\alpha$ and the direction is $\langle 101\rangle_\gamma // \langle 101\rangle_\alpha$. The schematic view of this relation is shown in Fig. 6.

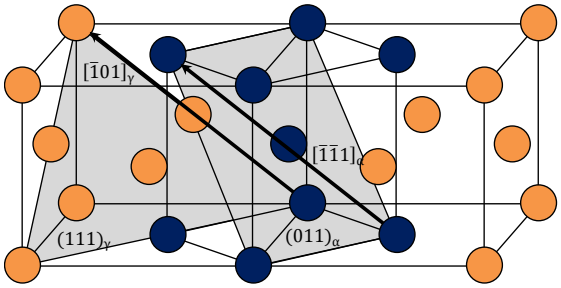

Orange points: f.c.c., Blue points: b.c.c.

Fig. 6 Kurdjumov-Sachs relation for f.c.c to b.c.c. phase transformation.

The corresponding rotation is $90^\cdot$ around the axis $\langle 112 \rangle$. Thus, the rotation matrix $A^{\gamma\to\alpha}$ can be given by inserting $(n_1, n_2, n_3) = (1,1,2)$ and $\theta_i = 90^\cdot$ into rotation matrix (97). It is known that there are 24 possible variants that b.c.c. materials take after phase transformation [68]. When we call the first variants obtained by Fig. 6, the relation between the variant 1 (V_1) and the other variants are given in Table 8.

Table 8 Crystallographic relation between V_1 and other variants [75].

Variant No.	Parallel surface	Parallel direction	Rotation axis	Angle(deg)
1	$(111)_\gamma$// $(011)_\alpha$	$[\bar{1}01]_\gamma$// $[\bar{1}\bar{1}1]_\alpha$	-	-
2		$[\bar{1}01]_\gamma$// $[\bar{1}1\bar{1}]_\alpha$	[0.5774,0.5774, −0.5774]	60.00
3		$[01\bar{1}]_\gamma$// $[\bar{1}\bar{1}1]_\alpha$	[0.0000,0.7071,0.7071]	60.00
4		$[01\bar{1}]_\gamma$// $[\bar{1}1\bar{1}]_\alpha$	[0.0000, −0.7071, −0.7071]	10.53
5		$[1\bar{1}0]_\gamma$// $[\bar{1}\bar{1}1]_\alpha$	[0.0000, −0.7071, −0.7071]	60.00
6		$[1\bar{1}0]_\gamma$// $[\bar{1}1\bar{1}]_\alpha$	[0.0000,0.7071,0.7071]	49.47
7	$(1\bar{1}1)_\gamma$// $(011)_\alpha$	$[10\bar{1}]_\gamma$// $[\bar{1}\bar{1}1]_\alpha$	[−0.5774, −0.5774,0.5774]	49.47
8		$[10\bar{1}]_\gamma$// $[\bar{1}1\bar{1}]_\alpha$	[0.5774,0.5774, −0.5774]	10.53
9		$[\bar{1}\bar{1}0]_\gamma$// $[\bar{1}\bar{1}1]_\alpha$	[−0.615,0.1862, −0.7667]	50.51
10		$[\bar{1}\bar{1}0]_\gamma$// $[\bar{1}1\bar{1}]_\alpha$	[−0.7387, −0.4625,0.4904]	50.51
11		$[011]_\gamma$// $[\bar{1}\bar{1}1]_\alpha$	[0.9329,0.3543,0.0650]	14.88
12		$[011]_\gamma$// $[\bar{1}1\bar{1}]_\alpha$	[−0.3568,0.6029,0.7136]	57.21
13	$(\bar{1}11)_\gamma$// $(011)_\alpha$	$[0\bar{1}1]_\gamma$// $[\bar{1}\bar{1}1]_\alpha$	[0.3543, −0.9329, −0.0650]	14.88
14		$[0\bar{1}1]_\gamma$// $[\bar{1}1\bar{1}]_\alpha$	[−0.4904,0.4625, −0.7387]	50.51
15		$[\bar{1}0\bar{1}]_\gamma$// $[\bar{1}\bar{1}1]_\alpha$	[−0.7384, −0.2461,0.6278]	57.2
16		$[\bar{1}0\bar{1}]_\gamma$// $[\bar{1}1\bar{1}]_\alpha$	[0.6589, −0.6589, −0.3628]	20.61
17		$[110]_\gamma$//	[−0.6589,0.3628, −0.6589]	51.73

		$[\bar{1}\bar{1}1]_\alpha$		
18		$[110]_\gamma$// $[\bar{1}1\bar{1}]_\alpha$	$[-0.7193, -0.3022, 0.6255]$	47.11
19		$[\bar{1}10]_\gamma$// $[\bar{1}\bar{1}1]_\alpha$	$[-0.1862, 0.7667, 0.6145]$	50.51
20		$[\bar{1}10]_\gamma$// $[\bar{1}1\bar{1}]_\alpha$	$[0.3568, 0.714, -0.6029]$	57.21
21	$(11\bar{1})_\gamma$// $(011)_\alpha$	$[0\bar{1}\bar{1}]_\gamma$// $[\bar{1}\bar{1}1]_\alpha$	$[0.9551, 0.0000, -0.2962]$	20.61
22		$[0\bar{1}\bar{1}]_\gamma$// $[\bar{1}1\bar{1}]_\alpha$	$[-0.3022, 0.626, 0.7193]$	47.11
23		$[101]_\gamma$// $[\bar{1}\bar{1}1]_\alpha$	$[-0.2461, -0.6278, -0.7384]$	57.21
24		$[101]_\gamma$// $[\bar{1}1\bar{1}]_\alpha$	$[0.9121, -0.4100, 0.0000]$	21.06

These 24 variants are plotted in Fig. 7 in $[001]_\alpha$ pole figure.

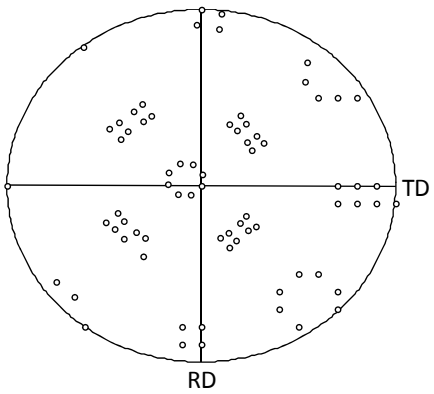

Fig. 7 K-S 24 variants plotted on $[001]_\alpha$ pole figure.

Let V_i the *i*-th variant rotation matrix from V_1, the rotation matrix from f.c.c. to b.c.c. can be written as follows:

$$A_i^{\gamma\to\alpha} = A^{\gamma\to\alpha} V_i \ . \tag{101}$$

Note that the rotation of $\theta_i = 90^\cdot$ about $(n_1, n_2, n_3) = (1,1,2)$ gives the 7-th variant shown in Table 8. Thus, in order to find the rotation matrix to 1st variant, one rotates $\theta_i = -49.47^\cdot$ about $(n_1, n_2, n_3) = (-1,-1,1)$ and finally obtains:

$$\boldsymbol{R_{KS}} = \begin{pmatrix} -0.075 & -0.167 & 0.983 \\ 0.742 & 0.650 & 0.167 \\ -0.667 & 0.742 & 0.075 \end{pmatrix}. \quad (102)$$

2.6.3.3 N-W relation

Nishiyama [74] and Wasserman [35] have suggested another model which describes orientation relation before and after phase transformation. This relation is depicted in Fig. 8.

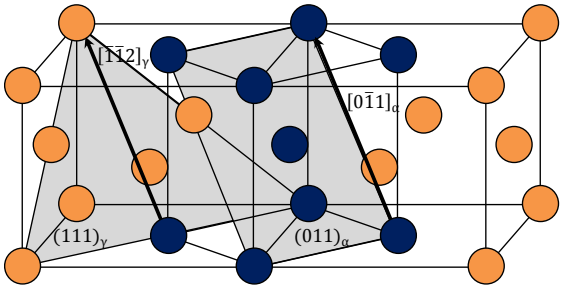

Orange points: f.c.c., Blue points: b.c.c.

Fig. 8 Nishiyama-Wasserman relation for f.c.c to b.c.c. phase transformation.

As shown in Fig. 8, the parallel surface is $\{111\}_\gamma//\{110\}_\alpha$ and the direction is $\langle 112\rangle_\gamma//\langle 011\rangle_\alpha$. The corresponding rotation is -95.3° around the axis $[-1+\sqrt{2}+\sqrt{3}, 1+\sqrt{2}+\sqrt{3}, \sqrt{2}]$. Thus, the rotation matrix $A^{\gamma\to\alpha}$ can be given by inserting $(n_1, n_2, n_3) = (1,1,2)$ and $\theta_i = 90^\circ$ into rotation matrix (97).

The number of variants that N-W relation has is 12. The relations among the 12 variants are shown in Table 9.

Table 9 Crystallographic relation between V_1 and other variants [75].

Variant No.	Parallel surface	Parallel direction	Rotation axis	Angle(deg)
1		$[211]_\gamma$// $[011]_\alpha$	-	-
2	$(111)_\gamma$// $(011)_\alpha$	$[121]_\gamma$// $[011]_\alpha$	$[0.0000, -0.7071, -0.7071]$	60.000
3		$[112]_\gamma$// $[011]_\alpha$	$[0.0000, 0.7071, 0.7071]$	60.000
4		$[211]_\gamma$// $[011]_\alpha$	$[1.0000, 0.0000, 0.0000]$	19.471
5	$(1\bar{1}1)_\gamma$// $(011)_\alpha$	$[121]_\gamma$// $[011]_\alpha$	$[-0.223, -0.697, -0.681]$	53.691
6		$[112]_\gamma$// $[011]_\alpha$	$[-0.223, 0.697, 0.681]$	53.691
7		$[0\bar{1}1]_\gamma$// $[011]_\alpha$	$[0.706, -0.706, -0.060]$	13.760
8	$(\bar{1}11)_\gamma$// $(011)_\alpha$	$[110]_\gamma$// $[011]_\alpha$	$[-0.681, -0.223, 0.697]$	53.691
9		$[110]_\gamma$// $[011]_\alpha$	$[-0.624, 0.471, -0.624]$	50.046
10		$[\bar{1}10]_\gamma$// $[011]_\alpha$	$[0.706, 0.706, 0.060]$	13.760
11	$(11\bar{1})_\gamma$// $(011)_\alpha$	$[101]_\gamma$// $[011]_\alpha$	$[-0.624, -0.471, 0.624]$	50.046
12		$[101]_\gamma$// $[011]_\alpha$	$[-0.681, 0.223, -0.697]$	53.691

Note that the rotation of -95.3° about the axis $[-1+\sqrt{2}+\sqrt{3}, 1+\sqrt{2}+\sqrt{3}, \sqrt{2}]$ gives 9th variant in the Table 9. Thus, in order to find the rotation matrix to 1st variant, one rotates $\theta_i = -50.046^\circ$ about $(n_1, n_2, n_3) = (-624, 0.471, -0.624)$ and one obtains:

$$\boldsymbol{R_{NW}} = \begin{pmatrix} 0 & 0.170 & -0.985 \\ 0.707 & 0.697 & 0.120 \\ -0.707 & -0.697 & -0.120 \end{pmatrix}. \quad (103)$$

The difference between N-W relation and K-S relation is only 5.3°.

Another way to find rotation matrix (98) is to start from Bain relation [76]. The rotation

from Bain relation to N-W relation is $-9.74^{\cdot}$ around the axis $[\bar{1}01]$, thus:

$$\boldsymbol{R_{B\to NW}} = \begin{pmatrix} 0 & 0 & 0 \\ 0 & \cos(-9.74^{\cdot}) & -\sin(-9.74^{\cdot}) \\ 0 & \sin(-9.74^{\cdot}) & \cos(-9.74^{\cdot}) \end{pmatrix}. \tag{104}$$

2.7 Prediction of beginning of diffusive transformation

Above models are dedicated for calculation of evolution of daughter phase (grains growing process). Here let us explain the model for prediction of transformation start timing. For non-diffusive transformation, the transformation start temperature is considered to be independent of the cooling history. So, the transformation start automatically when the temperature reaches M_S point. On the other hand, for diffusive transformation, the transformation starting temperature changes in response to the cooling velocity, heating temperature and so on. Scheil [77] introduced the notion of latent period and consumption ratio. In this model, the transformation starts when the following equation is satisfied.

$$\sum_i \frac{\Delta t_i}{\tau_i(T_i)} = 1 \ , \tag{105}$$

where $\tau_i(T_i)$ is time duration until phase transformation start when temperature is kept at constant value T_i. Δt_i is often taken as computational time increment in one step.

Chapter 3 Experimental determination of transformation plastic strain

3.1 Experimental method

3.1.1 Carbon Steels

Tensile machine with heating and cooling system is developed for identifying transformation plasticity. The Ar jet cooling system, which enables high cooling rates for obtaining martensite phase, is installed in the Instron 8802 fatigue testing machine in a research centre of Nippon Steel & Sumitomo Metal Corporation, Japan. In this facility, an induction heating system is adapted to heat up specimens up to 1300 ℃. It is also important to note that vacuum chamber is necessary for such high temperature; otherwise, thick layer of oxide scale is generated, which makes it difficult to detect precise temperature. In this PhD thesis, the specimen with chemical composition shown in Table 10 -with Japanese industrial standard (JIS) code- are adopted. They are initially heated up to 900 ℃ and keep the temperature for 5 minutes in order to obtain fully austenite phase, which is followed by applying small stress ranging from -50 MPa to 50 MPa. No sooner stress is applied than the specimens are cooled down. The cooling rates are 8 ℃/sec and 50 ℃/sec at 700 ℃/sec. In the course of cooling procedure, phase transformation from austenite phase to pearlite or martensite phase occurs depending on the cooling rates. During the transformation, one observes large strain generation depending on the values of applied stress.

3.1.2 Fe-Ni-Co Invar alloys

Two types of Invar alloys with chemical composition summarised in Table 11 are used. The aim of using Invar alloys is to take advantage of their extremely small transformation volume expansion [78] to determine the Greenwood-Johnson effect of martensite transformation.

Fe-25Ni-20Co Invar alloy has the magnetic transformation point at about 500 ℃, and below this temperature, coefficient of thermal expansion decreases significantly. Therefore, the alloy has considerably small transformation volume expansion when it transforms to martensite phase.

Another Invar alloy Fe-27Ni-20Co has Ms point below 0 ℃. It means that the alloy

remains austenite phase at room temperature. Hence, sub-zero cooling should be taken to obtain martensite phase. For the purpose of this, a liquid nitrogen direct cooling system has been developed and installed into a tensile testing machine (installed in Japan Ultra-high temperature Materials Research Centre: JUTEM, Japan) to achieve temperature lower than -100 ℃. This temperature is enough lower than Ms point of Fe-27Ni-20Co alloy according to the reference11). Maximum cooling rate of this system is about 0.2 ℃/sec. A picture of this apparatus is shown in Fig. 9. The specimens are cooled down by liquid Nitrogen during loading and strains are measured at the same time. The strain gauges are employed to ultra low temperature. The gauge's thermal expansion is identified beforehand, and the resultant strain is calculated by subtracting the gauge's thermal expansion from its original voltage data. This Invar alloy has tremendously small transformation volume expansion (almost zero). This is because, besides its lowness of Ms point, thermal expansion is tremendously small if the temperature is below magnetic transformation point. This alloy has a value of transformation volume expansion much smaller than that of Fe-25Ni-20Co alloy.

Table 10 Chemical composition for carbon steels (wt%).

	C	Si	Mn	P	S	Ni	Cr	Mo	Cu
S45C	0.46	0.19	0.65	0.08	0.05	0.02	0.02	0.0	0.02
SCM415	0.15	0.17	0.82	0.16	0.19	0.03	1.11	0.16	0.01
SM490	0.14	0.26	1.22	0.016	0.004	0.08	0.09	0.03	0.17
SCr420	0.21	0.26	0.87	0.017	0.018	0.45	0.5	0.16	0.01
SUJ2*	0.95-1.1	0.15-0.35	<0.50	<0.025	<0.025		1.3-1.6		

* The data signify standard values (not measured).

Table 11 Chemical composition for Invar alloys (wt%).

	Ni	Co
Fe-25Ni-20Co	25	20
Fe-27Ni-20Co	27	20

3.2 Results and Discussions

3.2.1 Temperature-strain curves

Obtained temperature-strain curves are depicted in Fig. 10 (a) for S45C carbon steel with natural cooling (pearlite transformation), in (b) for S45C with intense cooling (martensite transformation), in (c) for Fe-25Ni-20Co Invar alloy, and in (d) for Fe-27Ni-20Co Invar alloy.

From figure 2 (a) and (b), when temperature reaches the phase transformation start point, large strain development is observed. These strain values depend on the magnitude of applied stress, even though the applied stress is below yield stress of mother phase.

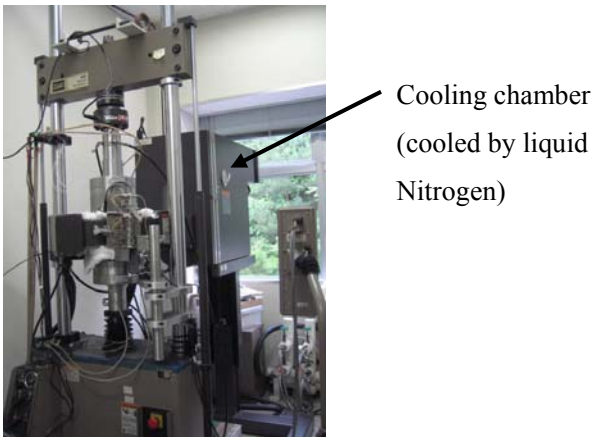

Fig. 9 Apparatus for tensile test under subzero condition.

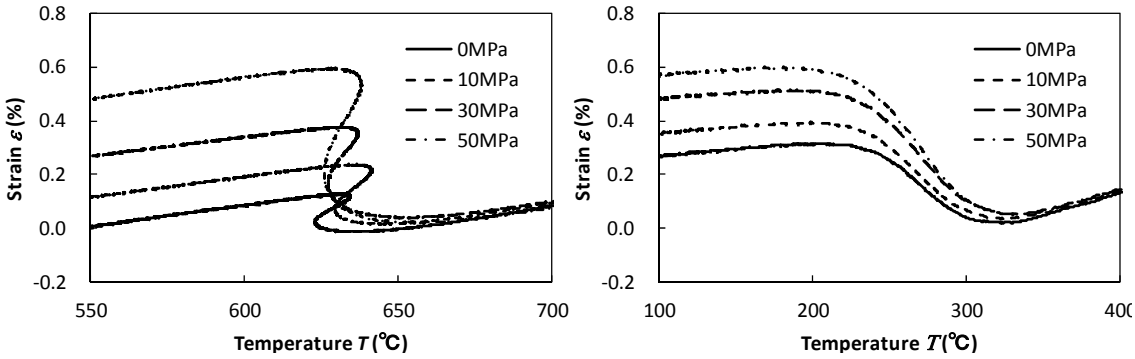

(a) S45C (pearlite transformation) (b) S45C (martensite transformation)

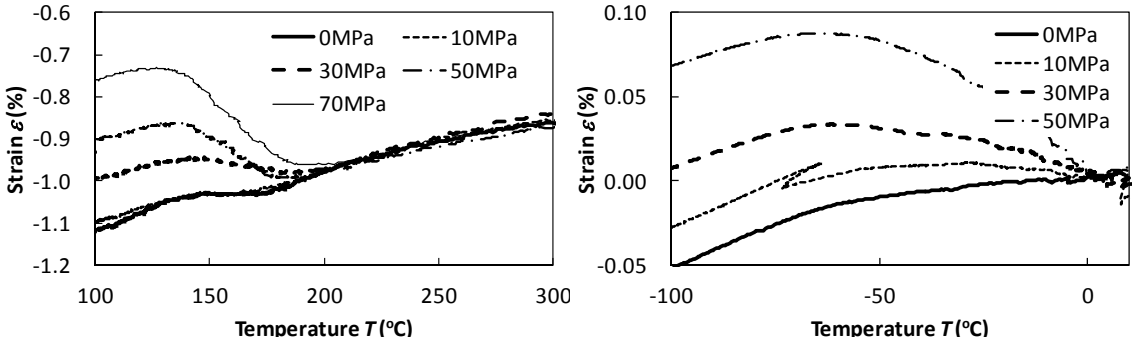

(c) Fe-25Ni-20Co (d) Fe-27Ni-20Co

Fig. 10 Temperature-Strain curves under various applied stress.

It should be also noted that the temperature of S45C pearlite transformation in Fig. 10 (a) rises during phase transformation. This is caused by latent heat generated with phase transformation. The reason why this temperature rising is not observed for martensite transformation in Fig. 10 (b), (c), is that the cooling rates for those martensite transformation are enormously faster so that the latent heat is not enough to bring temperatures upward.

From Fig. 10 (d), it is observed that the temperature drops below room temperature by liquid nitrogen i.e. sub-zero cooling is performed. The strain value is corrected by subtracting thermal expansion of strain gauge itself, which is preliminary identified. After cooling by liquid nitrogen, temperature returns back to room temperature. During cooling, the phase becomes fully martensite and remains at room temperature. Consequently, the coefficient of thermal expansion during returning back to room temperature (martensite) is different from that of during cooling (austenite). From Fig. 10 (c) and (d), one can also observe the dependence of strain during phase transformation with the applied stress. This fact says that the Invar alloy shows, although small, transformation plasticity, even though the transformation expansion is small. As we can see below, the magnitude of transformation plastic strain is one-order smaller than those of carbon steels.

3.2.2 Stress-transformation plastic strain relation

Transformation plastic strain values for each steel grade can be calculated by Fig. 10 depending on applied stress value. For example, transformation plastic strain of S45C pearlite transformation is the strain difference at 550 ℃ between stress-free strain value and the strain value with small applied stress. This calculation is valid only when every single test is carried out under the same temperature history. This is because transformation volume expansion and thermal strain vary significantly with temperature history such as cooling rate or heating temperature. Relations between applied stress and total transformation plastic strain are shown in Fig. 11 (a) for S45C (pearlite), (b) for S45C (martensite), (c) for Fe-25Ni-20Co, and (d) for Fe-27Ni-20Co respectively. Fig. 11 shows that the dependence of applied stress on transformation plastic strain is linear when the applied stress is small. In contrast, it is well-known that when applied stress is high, applied stress-transformation plastic strain relation is no longer linear. The threshold stress below which this linear relation is satisfied is approximately half the value of yield stress of mother phase [41]. The value of transformation expansion can be determined by strain results under 0 MPa applied stress. For Fe-25Ni-20Co and Fe-27Ni-20Co Invar alloys, in spite of its smallness of transformation volume expansion, it shows good proportional relationship between applied stress and transformation plastic strain. From

the Leblond's model, the proportionality factor between applied stress and total transformation plastic strain can be calculated by integrating (7) from transformation start point $z = 0.03$ to transformation complete point $z = 1$ such that,

$$K \cong 0.8648 \frac{2\beta}{\sigma_y^1} \ . \tag{106}$$

The value K is called transformation plasticity coefficient. Leblond's model indicates that this coefficient has linear relation with transformation expansion (This will be discussed in following section). Therefore, the transformation plasticity coefficient K can be calculated in two ways. One is by Leblond's model as expressed in equation (7). The other way is using Fig. 11 and equation (2). By integrating equation (2) from transformation start point $z = 0.03$ to transformation complete point $z = 1$, one obtains total transformation plastic strain, such that

$$\varepsilon_{ij}^{tp} = \int_0^1 3K(1-z)s_{ij}dz = \frac{3}{2}Ks_{ij} \ . \tag{107}$$

If applied stress is uniaxial, transformation plastic strain can be written in simple form.

$$\varepsilon^{tp} = K\sigma \ . \tag{108}$$

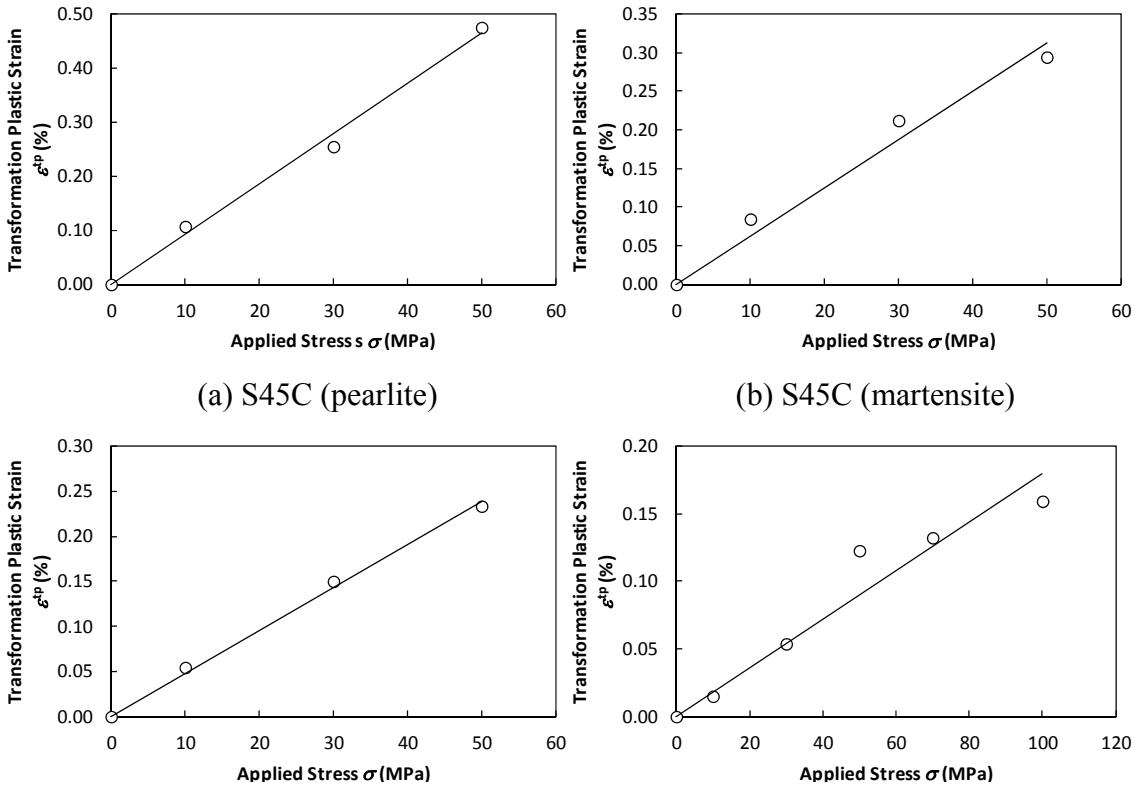

(a) S45C (pearlite) (b) S45C (martensite)

(c) Fe-25Ni-20Co (d) Fe-27Ni-20Co

Fig. 11 Transformation plastic strain under various applied stress for each material.

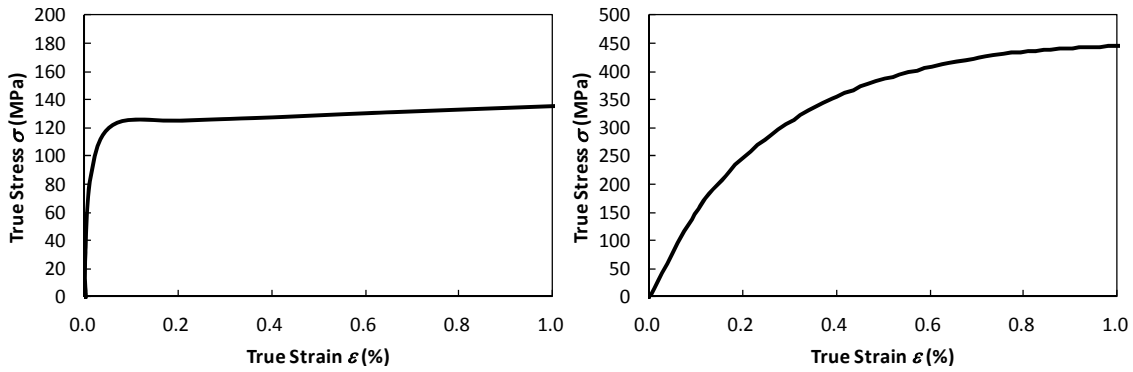

(a) S45C at 674 ℃ (b) S45C at 340 ℃

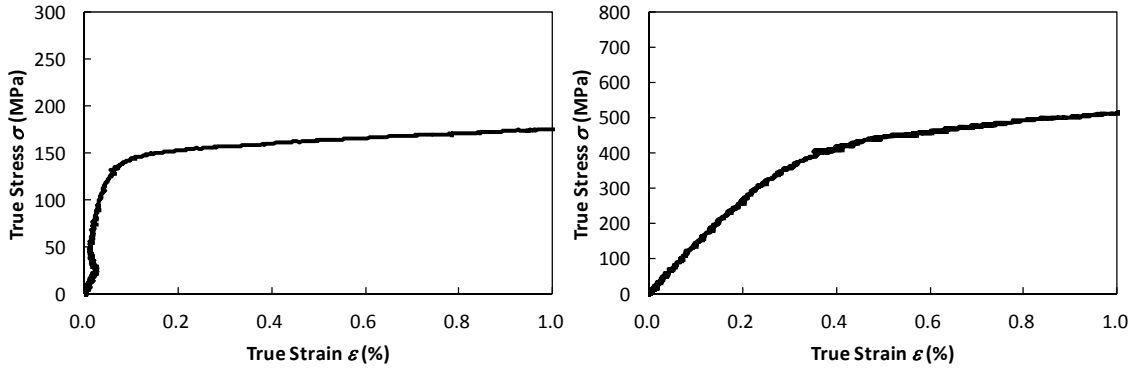

(c) Fe-25Ni-20Co at 220 ℃ (d) Fe-27Ni-20Co at RT

(Cooling rate at 700 ℃ is 50 ℃/sec.)

Fig. 12 Stress-strain curves right before transformation start.

Therefore, transformation plasticity coefficient K is a slope of Fig. 11. The transformation plasticity coefficients calculated by the latter way (108) are denoted by K_P (pearlite) and K_M (martensite).

3.2.3 Yield stresses

According to Leblond's model, the transformation plasticity coefficient depends on the coefficient of volume expansion and the yield stress of parent phase. To obtain stress-strain curves of mother phase of each material, tensile tests under the same temperature history as the tests for transformation plasticity (Fig. 10) are carried out. The specimens are heated up to 900 ℃, and keep the temperature for 5 minutes. After the 5 minutes, they are cooled down as the same manner (i.e. same cooling rate) of the tests for transformation plasticity. Shortly before transformation start point, tensile tests are carried out. The transformation start points can be determined by stress free temperature-strain curves. The loading points are carefully determined, for it is assumed

that the yield stress is dependent on temperature. It is also important to duplicate the cooling rate, because it affects the yield stress. If the upper yield point is not clear, then 0.2 % proof stress is adopted. The stress-strain curves of S45C (Pearlite), S45C (martensite), Fe-25Ni-20Co, and Fe-27Ni-20Co are drawn in Fig. 12 (a), (b), (c) and (d) respectively. These experiments are carried out at 0.02 (s^{-1}) strain rate.

3.2.4 Dependence of transformation plasticity coefficient on volume expansion and yield stress:

3.2.4.1 Case of pearlite

Transformation expansion can be obtained from temperature-strain curves under stress free condition. Although, strictly speaking, these values are not unique for one steel grade. It is because the transformation expansion is a dependent of cooling rate and obtained phase. This is the reason why one has to be careful when carrying out experiments that the temperature history should be exactly the same throughout the experimental sequence of one type of steel grade.

The obtained results of transformation volume expansion, yield stress and transformation plastic coefficient K_P are shown in Table 12. From the data in Table 12, relation between the parameter $2\beta/\sigma_y^1$ and transformation plasticity coefficient K_P are depicted in Fig. 13. Fig. 13 indicates that the relation between the parameter in equation (7) and transformation plasticity coefficients K_P is proportional, although the obtained transformation plasticity coefficients K_P are much larger than the one estimated by equation (7).

Table 12 Transformation expansion and transformation plasticity coefficient data for each material (pearlite transformation).

	β	σ_y^1 (MPa)	K_P (MPa^{-1})
S45C*	1.5×10^{-3}	121	9.2×10^{-5}
SCM415*	2.4×10^{-3}	88	14×10^{-5}
SM490*	1.8×10^{-3}	63	18×10^{-5}
SCr420*	2.1×10^{-3}	153	14×10^{-5}

* Cooling rate at 700 ℃ is 8 ℃/sec.

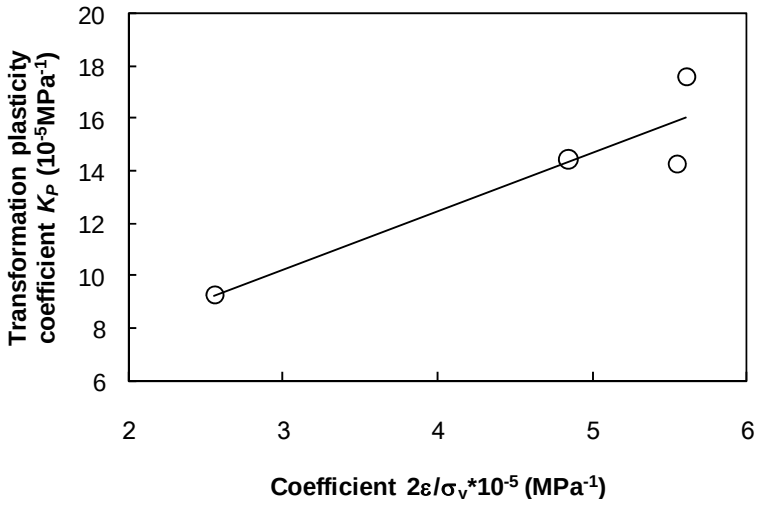

Fig. 13 Relation between parameter $-2\beta/\sigma_y^1$ and transformation plasticity coefficient.

3.2.4.2 Case of martensite

Similar to the pearlite transformation, obtained transformation expansion, yield stress and transformation plasticity coefficient K_M are shown in Table 13.

Along with the data shown in Table 13, the relations between parameter $2\beta/\sigma_y^1$ and transformation plasticity coefficient for martensite transformation K_M are depicted in Fig. 14. From Fig. 14, one can observe the proportional relation between transformation volume expansion over yield stress and transformation plasticity coefficient K_M. With smaller transformation volume expansion, we have considerably small value of transformation plasticity coefficient for Fe-25Ni-20Co and Fe-27Ni-20Co Invar alloy. From this proportional factor, parameter $2\beta/\sigma_y^1$ for martensite transformation can be calculated by equations (106) and (108).

Similar to pearlite transformation, the magnitude of the transformation plasticity coefficient K_M is slightly larger than that of parameter $2\beta/\sigma_y^1$. Even though, the proportional relation between the parameter and transformation plasticity is satisfied, i.e. the idea of equation (7) is confirmed to be valid.

Table 13 Transformation expansion and transformation plasticity coefficient data for each material (martensite transformation).

	β	σ_y^1 (MPa)	K_M (MPa^{-1})
S45C*	4.2×10^{-3}	240	5.8×10^{-5}
SCr420*	2.1×10^{-3}	150	10.8×10^{-5}
Fe-25Ni-20Co**	0.25×10^{-3}	153	3.2×10^{-5}
Fe-27Ni-20Co***	0.071×10^{-3}	270	1.6×10^{-5}

* Cooling rate at 700 ℃ is 8 ℃/sec.

** Cooling rate at 700 ℃ is 50 ℃/sec.

*** Cooling rate at 0 ℃ is 0.09 ℃/sec.

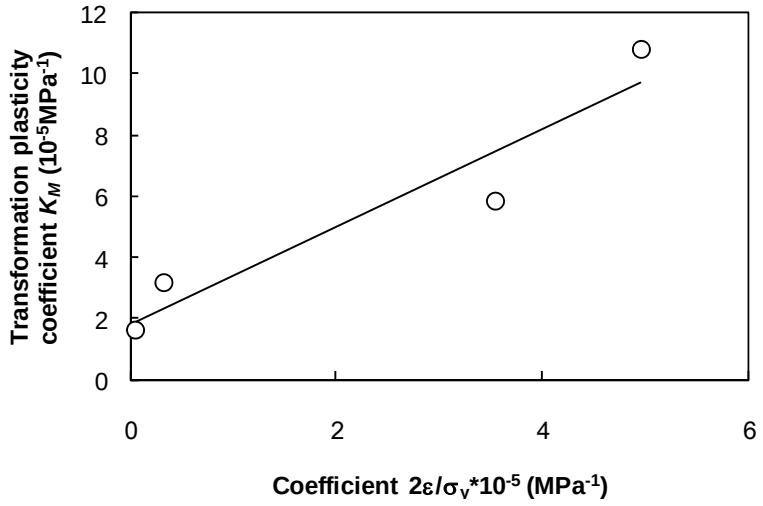

Fig. 14 Relation between parameter $-2\beta/\sigma_y^1$ and transformation plasticity coefficient.

All above tests have been done under tensile stress. Videau *et al*. [41] showed in their paper that there is dependence of transformation plasticity on the loading condition. By contrast, the experimental results by Miyao *et al*. [36] imply that there is no difference between tensile and compressive applied stress. The difference may occur depending on the steel grades and the conditions such as transformation type or cooling rates.

In fact, it has been observed the difference in transformation plastic strains between tensile and compressive applied stress on SUJ2 steel during martensitic phase transformation (see Fig. 15), although, not significant difference has been observed for S45C pearlitic phase transformation The mechanism of this phenomenon will be discussed together with numerical modelling in the later chapter.

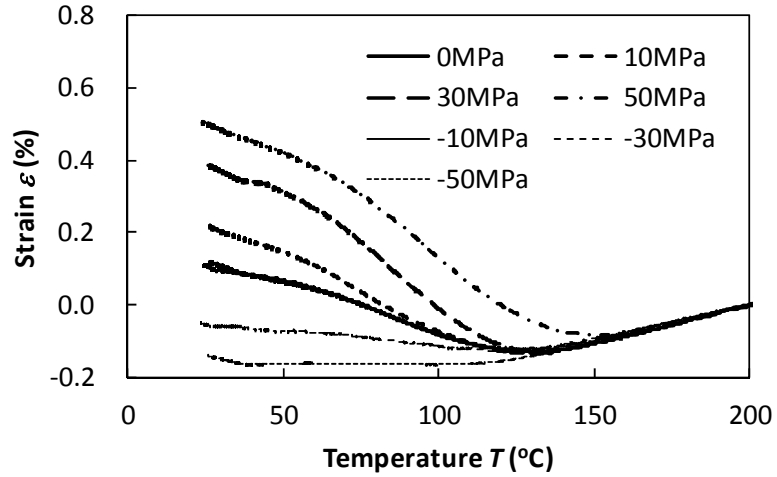

(a) Cooling curves

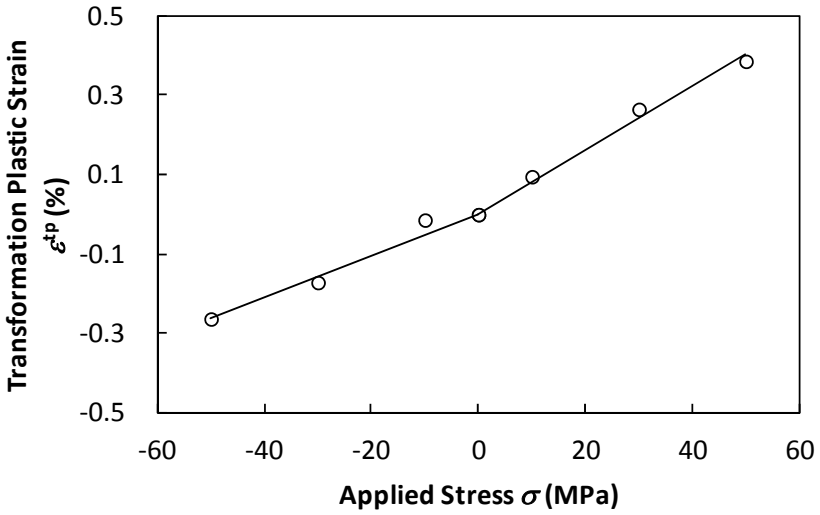

(b) Transformation plastic strain

Fig. 15 Experimental results of SUJ2 steel (tension/compression).

The calculated results of transformation plastic coefficients for SUJ2 are; $K_M^+ = 7.75 \times 10^{-5}$ for tensile applied stress and $K_M^- = 5.66 \times 10^{-5}$ for compressive applied stress. So it shows about 30 % difference between tensile and compressive applied stresses. The mechanism of this difference will be discussed in the following chapter.

The same tests are carried out on S45C materials for pearlitic phase transformation; the results are shown in Fig. 16. Although transformation start temperature are not consistent, the results appear to be enough accurate for transformation plasticity. In this case, it shows no significant difference between tensile and compressive conditions. This appears

to be inconsistent with the previous test results.

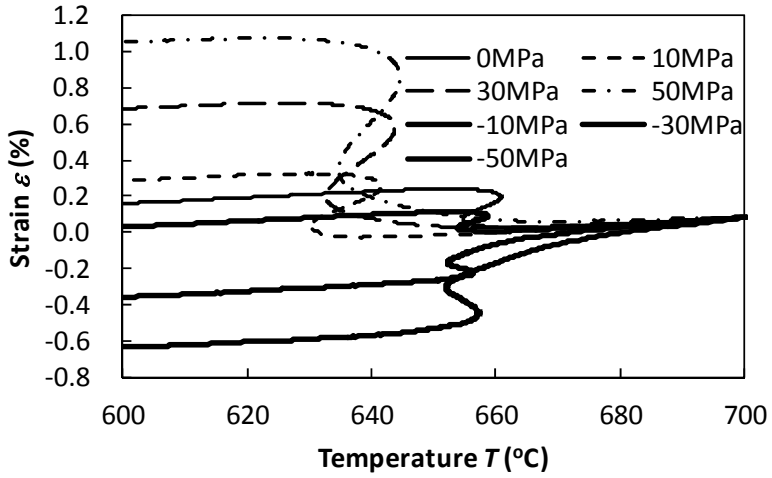

(a) Cooling curves

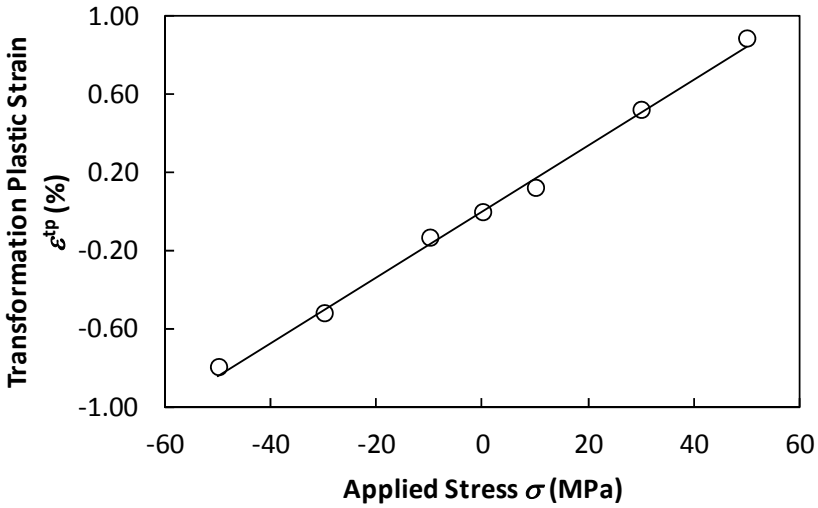

(b) Transformation plastic strain

Fig. 16 Experimental results of S45C steel (tension/compression).

3.3 Identification of transformation plasticity under high applied stress

The transformation plasticity test under relatively high applied stress has been performed. It is expected that the relation between applied stress and transformation plastic strain is nonlinear when applied stress is large. Tests have been carried out on SM490 steel of pearlitic phase transformation as shown in Fig. 17.

From Fig. 17, the nonlinearity appears between 30 MPa and 50 MPa. The yield stress of SM490 austenite phase before phase transformation is estimated as 63 MPa from Table 12. Our experimental results appear to be in good agreement with previous studies

[5][41].

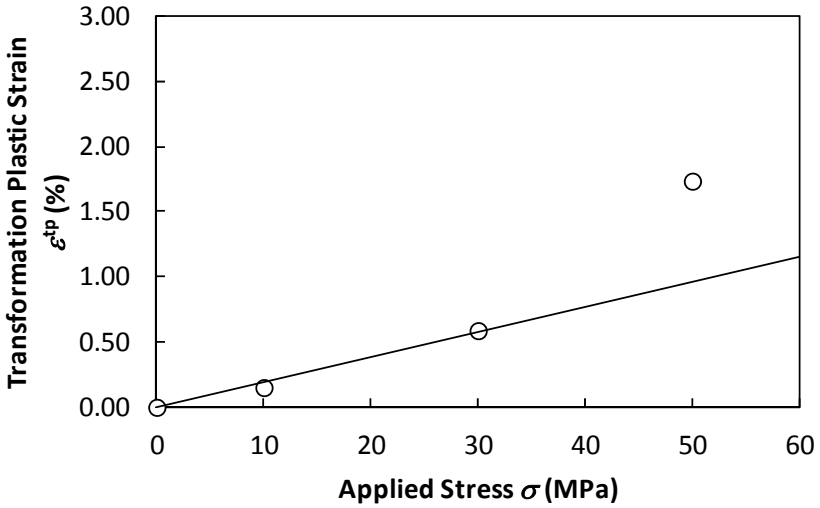

Fig. 17 Stress-Transformation plastic strain relation of SM490 pearlitic transformation.

3.4 Brief summary of experimental results

Several carbon steel grades and Invar alloys have been employed to identify the dependence of volume expansion on transformation plasticity for both diffusive and nondiffusive transformation.

For pearlite tranformation, the proportional relation between the parameter $2\beta/\sigma_y^1$ and transformation plasticity coefficient K_P is confirmed; however, the relation was not quantitatively correspond with Leblond's model.

For martensite transformation, the proportional relation is also confirmed. The parameter $2\beta/\sigma_y^1$ is slightly smaller than transformation plasticity coefficient K_M by experiments.

The experimental results for Invar alloys show that if the transformation volume expansion is significantly small, the transformation plastic strain becomes tremendously small accordingly. It is said that Magee effect (selective martensite variant) plays main role during martensite transformation. However, for several steel grades treated in this chapter, transformation volume change affects transformation plastic strain significantly. These results indicate that Greenwood-Johnson effect (transformation expansion) is not negligible during martensite transformation.

Chapter 4 Micromechanical modelling of transformation plasticity

4.1 Constitutive modelling of elastoplastic polycrystalline media

An efficient numerical scheme based on Fourier transforms [25] has been developed and applied to a wide range of problems [26] [28] [29] [30]. This numerical scheme can consider large polycrystalline aggregates with reasonable computation time and memory requirements. Besides, meshing of the microstructure is not necessary. These features are especially convenient to consider experimental microstructural data [32] [33] [34]. It also offers an attractive framework to consider microstructural evolution during phase transformatioin. In this section, a coupling model of elastoplasticity using FFT numerical scheme and phase transformation model will be developed.

4.1.1 Elastic case

For the elastic heterogeneous material, the local constitutive equation is expressed by linear relation,

$$\sigma_{ij}(x) = C_{ijkl}(x)\varepsilon_{kl}(x)\ , \tag{109}$$

where x represents local position and C is local elastic tensor.

For heterogeneous material, the elastic tensor C is not uniform throughout the medium. By introducing homogeneous elasticity C^0, we have:

$$\sigma_{ij}(x) = C^0_{ijkl}\varepsilon_{kl}(x) + \left(C_{ijkl}(x) - C^0_{ijkl}\right)\varepsilon_{kl}(x) = C^0_{ijkl}\varepsilon_{kl}(x) + \tau_{ij}(x)\ , \tag{110}$$

where τ is a polarisation tensor.

Equilibrium condition reads:

$$\sigma_{ij,j}(x) = 0\ . \tag{111}$$

Equations (110) and (111) in the Fourier space are:

$$\hat{\sigma}_{ij}(\xi) = iC^0_{ijkl}\xi_l\hat{u}_k(\xi) + \hat{\tau}_{ij}(\xi) \ \text{ and } \ i\hat{\sigma}_{ij}(\xi)\xi_j = 0\ . \tag{112}$$

Eliminating σ from equation (112), we obtain

$$\hat{u}_k(\xi) = \frac{i}{2}\left(N^0_{ki}\xi_j + N^0_{kj}\xi_i\right)\hat{\tau}_{ij}(\xi)\ , \tag{113}$$

where

$$N^0_{ij}(\xi) = K^0_{ij}(\xi)^{-1}\ ,\ \ K^0_{ij}(\xi) = C^0_{ijkl}\xi_k\xi_l\ , \tag{114}$$

$$\hat{\varepsilon}_{kl}(\xi) = \frac{i}{2}\left(\xi_l \hat{u}_k(\xi) + \xi_k \hat{u}_l(\xi)\right) = -\hat{\Gamma}^0_{klij}(\xi)\hat{\tau}_{ij}(\xi)\,, \tag{115}$$

$$\hat{\Gamma}^0_{klij} = \frac{1}{4}\left(N^0_{li}\xi_j\xi_k + N^0_{ki}\xi_j\xi_l + N^0_{lj}\xi_i\xi_k + N^0_{kj}\xi_i\xi_l\right). \tag{116}$$

In the case of isotropic material, the introduced tensors can be written with Lamé's constants λ^0 and μ^0 such that,

$$C^0_{ijkl} = \lambda^0\delta_{ij}\delta_{kl} + \mu^0\left(\delta_{ik}\delta_{jl} + \delta_{il}\delta_{jk}\right),\ K^0_{ij}(\xi) = (\lambda^0+\mu^0)\xi_i\xi_j + \mu^0|\xi|^2\delta_{ij}\,,$$
$$N^0_{ij}(\xi) = \frac{1}{\mu^0|\xi|^2}\left(\delta_{ij} - \frac{\lambda^0+\mu^0}{\lambda^0+2\mu^0}\frac{\xi_i\xi_j}{|\xi|^2}\right),\ |\xi|^2 = \sum_i \xi_i^2 \ \text{ and} \tag{117}$$

$$\hat{\Gamma}^0_{klij} = \frac{1}{4\mu^0|\xi|^2}\left(\delta_{ki}\xi_l\xi_j + \delta_{li}\xi_k\xi_j + \delta_{kj}\xi_l\xi_i + \delta_{ij}\xi_k\xi_i\right) - \frac{\lambda^0+\mu^0}{\mu^0(\lambda^0+2\mu^0)}\frac{\xi_k\xi_l\xi_i\xi_j}{|\xi|^4}\,. \tag{118}$$

The tensor $\hat{\Gamma}^0_{klij}$ is the Green periodic operator for homogeneous medium C^0. The local problem is a Lipmann-Schwinger integral equation for $\varepsilon_{ij}(x)$, and the iterative algorithm for finding stress/strain values in this problem can be written as follows.

Initialise, $\varepsilon^0_{ij}(x) = \bar{\varepsilon}_{ij},\ \forall x \in V$

Iteration n+1: $\varepsilon^n_{ij}(x)$ and $\sigma^n_{ij}(x)$ are already known

(a) $\hat{\sigma}^n_{ij} = FFT(\sigma^n_{ij})$

(b) Check convergence $e^n = \dfrac{\sqrt{\langle\|\sigma^n_{ii}\|^2\rangle}}{\langle\|\sigma^n_{ii}\|\rangle} = \dfrac{\sqrt{\langle\|\xi_i\hat{\sigma}^n_{ii}(\xi)\|^2\rangle}}{\langle\|\hat{\sigma}^n_{ii}\|\rangle} < 1.0\times10^{-4}$

(c) $\hat{\varepsilon}^{n+1}_{ij}(\xi) = \hat{\varepsilon}^n_{ij}(\xi) - \hat{\Gamma}^0_{ijkl}(\xi)\hat{\sigma}^n_{kl}(\xi) \quad \forall\xi \neq 0 \quad \text{and} \quad \hat{\varepsilon}^{n+1}_{ij}(0) = \bar{\varepsilon}$

(d) $\varepsilon^{n+1}_{ij} = FFT^{-1}(\hat{\varepsilon}^{n+1})$

(e) $\sigma^{n+1}_{ij}(x) = C^0_{ijkl}(x)\varepsilon^{(n+1)}_{kl}(x) \qquad \forall x \in V$

4.1.2 Elasto-(Visco)Plastic case

In the elastoplasticity, the stress strain relationship is nonlinear. In this case, the equation (109) is rewritten as:

$$\sigma_{ij}(x) = C^0_{ijkl}\varepsilon^e_{kl}(x) + \tau_{ij}(x) = C^0_{ijkl}\left(\varepsilon_{kl}(x) - \varepsilon^p_{kl}(x)\right) + \tau_{ij}(x) = C^0_{ijkl}\varepsilon_{kl}(x) + \tau'_{ij}(x)\,. \tag{119}$$

This equation can be solved almost as the same manner as elastic case thanks for the polarisation tensor τ. The iterative solution for the elastoplastic problem can be written as follows.

Iterative algorithm for the FFT numerical scheme

Initialise, $\varepsilon_{ij}^{0}(x) = \varepsilon_{ij}^{n} + \Delta\varepsilon_{ij},\ \forall x \in V$

Iteration n+1: $\varepsilon_{ij}^{n}(x)$ and $\sigma_{ij}^{n}(x)$ are already known

(b) Check convergence $e^{n} = \frac{\sqrt{\langle \|\sigma_{ii}^{n}\|^{2} \rangle}}{\langle \|\sigma_{ii}^{n}\| \rangle} = \frac{\sqrt{\langle \|\xi_i \hat{\sigma}_{ii}^{n}(\xi)\|^{2} \rangle}}{\langle \|\hat{\sigma}_{ii}^{n}(0)\| \rangle} < 1.0 \times 10^{-4}$

(c) $\hat{\varepsilon}_{ij}^{n+1}(\xi) = \hat{\varepsilon}_{ij}^{n}(\xi) - \hat{\Gamma}_{ijkl}^{0}(\xi)\hat{\sigma}_{kl}^{n}(\xi) \quad \forall \xi \neq 0 \quad \text{and} \quad \hat{\varepsilon}_{ij}^{n+1}(0) = \bar{\varepsilon}$

(d) $\varepsilon_{ij}^{n+1} = FFT^{-1}(\hat{\varepsilon}^{n+1})$

(e) $\sigma_{ij}^{n+1}(x) = g\left(\varepsilon_{kl}^{n+1}(x)\right) \qquad \forall x \in V$

The differences between elastic problem and elastoplastic problems are the initialisation step and the constitutive equation. For elastoplasticity an incremental procedure has to be considered.

4.1.3 Coupling of elastoplasticity using FFT numerical scheme and phase transformation model

Phase transformation imposes stress/strain heterogeneity because of the volumetric difference between two phases. Moreover, the plastic strain is significantly concentrated in the weaker phase because of the difference of hardness in two different phases. In this section, the mechanical behaviour of polycrystalline material under γ/α phase transformation will be modelled by using FFT numerical scheme coupled with a phase transformation model.

First of all, let us consider the periodic boundary media with elastic tensor C, such that:

$$\sigma_{ij}(x) = C_{ijkl}(x)\varepsilon_{kl}(x)\ , \tag{120}$$

Then, considering elastic heterogeneity, introducing C^{0}, the homogeneous elastic tensor, by C, we have:

$$\sigma_{ij}(x) = C_{ijkl}^{0}\varepsilon_{kl}(x) + \left(C_{ijkl}(x) - C_{ijkl}^{0}\right)\varepsilon_{kl}(x) = C_{ijkl}^{0}\varepsilon_{kl}(x) + \tau_{ij}(x)\ , \tag{121}$$

where τ_{ij} is a polarisation tensor.

If the material is subject to plastic, thermal and transformation strain, the equation (121) is given as:

$$\begin{aligned} \sigma_{ij}(x) &= C_{ijkl}^{0}\varepsilon_{kl}^{e}(x) + \tau_{ij}(x) \\ &= C_{ijkl}^{0}\left(\varepsilon_{kl}(x) - \varepsilon_{kl}^{p}(x) - \varepsilon_{kl}^{th}(x) - \varepsilon_{kl}^{m}(x)\right) + \tau_{ij}(x) \\ &= C_{ijkl}^{0}\varepsilon_{kl}(x) + \tau_{ij}''(x)\ , \end{aligned} \tag{122}$$

where, ε_{kl}^{p}, ε_{kl}^{th} and ε_{kl}^{m} are plastic, thermal and transformation strain respectively. Note that we intend to describe transformation plastic strain through the scale transition process., At the local scale, there is no transformation plastic strain term.

The thermal strain and transformation strain can be expressed as:

$$\varepsilon_{ij}^{th} = \alpha\delta_{ij}T\ ,\quad \varepsilon_{ij}^{m} = \beta\delta_{ij}\xi\ , \tag{123}$$

where, α is a coefficient of linear expansion, T is temperature difference from reference state, β is coefficient of transformation expansion and ξ is volume fraction difference from reference state.

Now we consider a cubic area constituted of austenitic (parent phase) grains. The division is performed with a Poisson-Voronoi tessellation process (Fig. 18).

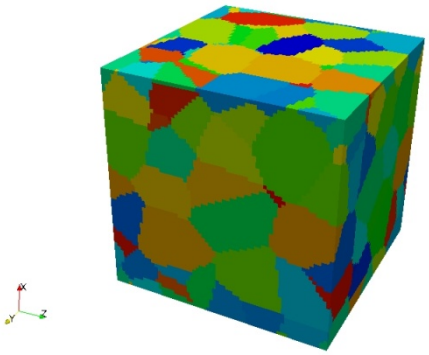

Fig. 18 Sample Voronoi tessellation; 100 grains in 64^3 cubic space.

The orientation of each grain is set randomly (each point has its Euler angle but the same grain is considered to share the same orientation). Bunge type Euler angle is adopted and the random orientation is calculated by following equation;

$$\phi_1 = 2\pi x_1\ ,\quad \Phi = \arccos(1-2x_2)\ ,\quad \phi_2 = 2\pi x_3\ , \tag{124}$$

where $x_i\ (0 \le x_i \le 1;\ i = 1,2,3)$ are random numbers. With the Euler angles given by equation (124), one obtains rotation matrix such that:

$$q_{ij} = \begin{pmatrix} \cos\phi_2\cos\phi_1 - \sin\phi_1\sin\phi_2\cos\Phi & \cos\phi_2\sin\phi_1 + \cos\phi_1\sin\phi_2\cos\Phi & \sin\Phi\sin\phi_2 \\ \sin\phi_2\cos\phi_1 - \sin\phi_1\cos\phi_2\cos\Phi & \sin\phi_1\sin\phi_2 + \cos\phi_1\cos\phi_2\cos\Phi & \cos\phi_2\sin\Phi \\ \sin\phi_1\sin\Phi & \sin\Phi\cos\phi_1 & \cos\Phi \end{pmatrix}, \tag{125}$$

So, if we initially set the slip systems (slip surface m_i^0 and slip direction s_i^0) according to Table 4, the vectors which is considered can be calculated as:

$$m_i = q_{ji}m_j^0\ ,\quad s_i = q_{ji}s_j^0\ . \tag{126}$$

4.1.4 Validation of the numerical implementation

In order to validate the FFT-based model, two kinds of calculations are carried out; first, macroscopic thermal strain is calculated following the method by Leblond *et al*. [15], and second, macroscopic transformation strain is calculated. These calculations are carried out with the FFT numerical scheme and compared with theoretical results. Then the results will be compared each other to verify the FFT-based polycrystalline model.

Starting with 100 parent grains, transformation begins and the macroscopic transformation strain is determined, which is assessed by following theoretical solution.

$$\bar{\varepsilon} = \bar{\varepsilon}^m = \beta z \,. \tag{127}$$

with z, the macroscopic volume fraction of daughter phase. The results obtained for an austenitic polycrystal composed of 100 grains with random orientations are shown in Fig. 19. The numerical response agrees with the exact result. The chosen numerical microstructure can thus be considered isotropic. It is noted that there is no macroscopic plastic strain hereas plastic deformation occurs at the crystal (microscopic) level.

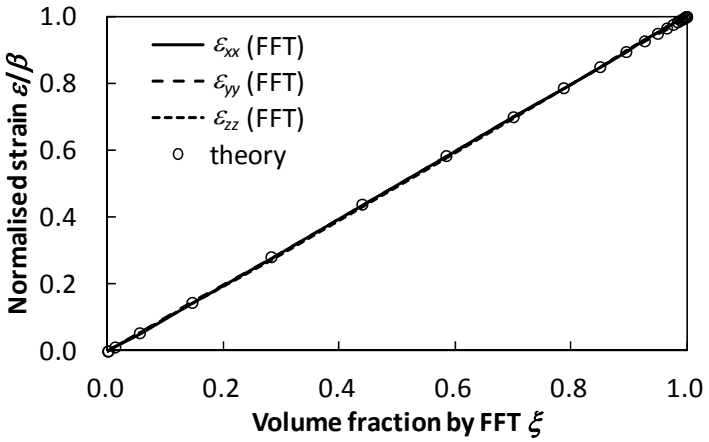

Fig. 19 Macroscopic thermal strain comparison between calculation and theory.

By the comparisons between FFT numerical model and theoretical ones, the model well describes the macroscopic homogeneity even though microscopically there are plastic strains in the microscopic scale.

Next, the following mixture law should be examined for validation of mixture model of polycrystalline material. The equation has been theoretically and numerically confirmed by Leblond *et al*. [79].

$$E^{th} = \langle \varepsilon^{th} \rangle_V = (1 - z)\varepsilon_1^{th} + z\varepsilon_2^{th} \,. \tag{128}$$

The calculation procedure is follows.

Thermal strain for phase 1 is set to -0.42 % and phase 2 0.42 %. So, if the volume fraction of phase 2 becomes 50 %, total macroscopic thermal strain E^{th} should equate 0.

The comparison of calculated results and theoretical results (by equation (128)) is written in Table 14. One can conclude with the results of Table 14 that the mixture law is well satisfied.

Table 14 Comparison of calculated and theoretical macroscopic strain.

Data from reference (FEM) [79]					Data obtained by FFT				
z	ε_x	ε_y	ε_z	theory	z	ε_x	ε_y	ε_z	theory
0.125	-0.319	-0.3	-0.317	-0.316	0.128	-0.314	-0.315	-0.308	-0.313
0.25	-0.219	-0.197	-0.195	-0.21	0.251	-0.213	-0.207	-0.210	-0.209
0.5	-0.045	0.015	0.003	0	0.504	0.011	-0.019	0.018	0.003
0.75	0.211	0.209	0.213	0.210	0.752	0.212	0.217	0.205	0.212

4.1.5 Comparison of Huntchinson and Anand-Kothari elastoplastic models

In the section 2.4.2.2, the two elastoplastic models have been introduced in this PhD thesis; Hutchinson [59] and Anand-Kothari [60]. These two approaches give slip rates for elastoplastic problems. In order to avoid a singular matrix, they make use of different techniques; Hutchinson's model restricts the number of active slip systems. By contraries, Anand-Kothari's model does not restrict the number of active slip systems but uses SVD technique for pseudo inverse matrices. In this case, it is important to compare the calculation results by these alternative methods.

The calculation is carried out in the 64^3 voxels cubic space with 100 austenitic grains. The f.c.c. slip systems shown in Table 4 (a) are used. The computational results of macroscopic stress/strain curves are depicted in Fig. 20. The macroscopic stresses and strains are calculated by volume averaging of the local values. The differences between two models are confirmed to be less than 10 % for the hardening materials and less than 5 % for the elasto-perfect plastic materials. In general, the austenite phase which is going to transform has material components similar to elasto-perfect plasticity. It means that the choice of models may bring little difference to the calculation of transformation plasticity.

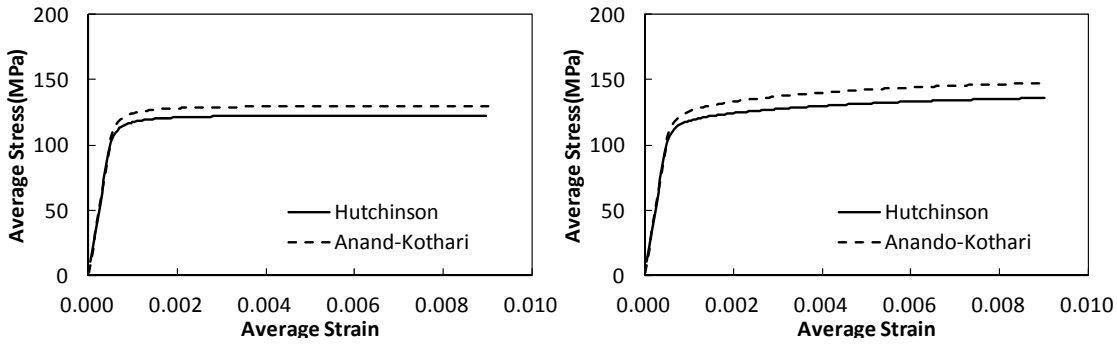

(a) $H_0 = 0$ (b) $H_0 = 550$

Fig. 20 Macroscopic stress/strain curve of 3 models with/without hardening.

4.1.6 Modified Hutchinson rate-independent model

Numerical solutions of elastoplastic problems of polycrystalline materials require a step by step procedure and the verification of the yield criteria and consistency condition. During iterations, newly calculated stresses are employed to judge whether the yield criteria are satisfied or not, and then the stress and strain will be updated according to the judgement.

If the previous state was elastic and the present state is also elastic, then one can use only elastic materials' constants to solve the stress/strain field. In the same manner, if previous and present states are elastoplastic, the condition allows one to use only elastoplastic constitutive relations. The condition that previous state was elastoplastic and the present one is elastic is rather tricky, for the case occurs not only unloading process but also loading process. The hardness of slip system can surpass resolved shear stress because of the slip on other slip systems. Contrary to above discussion, the cases of state change from elastic to elastoplastic condition is rather complicated and may provoke a problem because it is uncertain when the yield criterion is satisfied or not during one incremental step. For this kind of problem, we propose a methodology for crystalline elastoplasticity as follows.

The plastic strain rate is given by summation of each slip rate on the slip systems, such that

$$\dot{\varepsilon}_{ij}^{p} = \sum_{\alpha} \dot{\gamma}^{\alpha} p_{ij}^{\alpha} \ , \tag{129}$$

where α is slip system p_{ij}^{α} is a Schemid tensor. On the other hand, the stress rate of elastoplastic problem can be found as:

$$\dot{\sigma}_{ij} = C_{ijkl}(\dot{\varepsilon}_{kl} - \dot{\varepsilon}^{p}_{kl}) , \tag{130}$$

where $\dot{\varepsilon}_{kl}$ is total strain rate and C_{ijkl} is elastic stiffness tensor.
When resolved shear stress $\tau^{\alpha} = \sigma_{ij} p^{\alpha}_{ij}$ exceeds the value g^{α}, the material satisfies the yield condition and the problem becomes elastoplastic. The values g^{α} can be found according to the initial hardness of each slip system and their hardening law.

First of all, let us introduce Hutchinson method which allows to find the magnitude of slip rate on each slip system. Suppose that the work hardening and resolved stress increment of the α slip system during one step are equal as depicted inFig. 21.

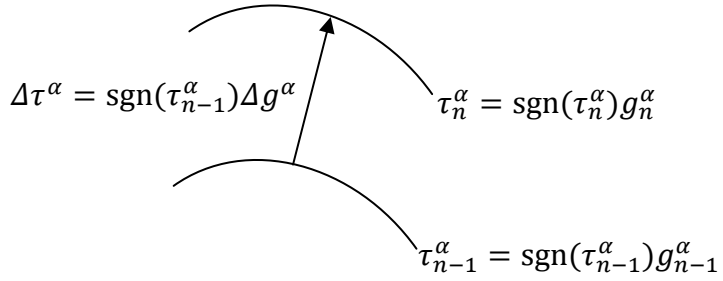

Fig. 21 Work hardening and resolved stress increment during plastic deformation.

It can also be expressed as:

$$\begin{aligned} \Delta\tau^{\alpha} &= \mathrm{sgn}(\tau^{\alpha}_{n-1})\Delta g^{\alpha} , \\ \Delta\sigma_{ij} p^{\alpha}_{ij} &= \sum_{\beta} h^{\alpha\beta}\Delta\gamma^{\beta} \ . \end{aligned} \tag{131}$$

When one introduces the matrix $X^{\alpha\beta}$, defined as:

$$X^{\alpha\beta} = h^{\alpha\beta} + p^{\alpha}_{ij} C_{ijkl} p^{\beta}_{kl} , \tag{132}$$

the following relation is obtained.

$$\begin{aligned} \sum_{\beta} X^{\alpha\beta}\Delta\gamma^{\beta} &= \sum_{\beta} h^{\alpha\beta}\,\Delta\gamma^{\beta} + \sum_{\beta} p^{\alpha}_{ij} C_{ijkl} p^{\beta}_{kl}\,\Delta\gamma^{\beta} \\ &= \Delta\sigma_{ij} p^{\alpha}_{ij} + p^{\alpha}_{ij} C_{ijkl}\varepsilon^{p}_{kl} \\ &= C_{ijkl}\left(\Delta\varepsilon_{kl} - \Delta\varepsilon^{p}_{kl}\right) p^{\alpha}_{ij} + p^{\alpha}_{ij} C_{ijkl}\varepsilon^{p}_{kl} \\ &= C_{ijkl}\Delta\varepsilon_{kl} p^{\alpha}_{ij} \end{aligned} \tag{133}$$

Thus, the slip increment is calculated by using matrix $Y^{\alpha\beta}$, the inverse matrix of $X^{\alpha\beta}$:

$$Y^{\alpha\beta} = \left(X^{\alpha\beta}\right)^{-1} , \tag{134}$$

such that,

$$\Delta\gamma^{\alpha} = \sum_{\beta} Y^{\alpha\beta} C_{ijkl} \Delta\varepsilon_{kl} p_{ij}^{\beta} \ . \tag{135}$$

Second, let us consider the situation where the state of α slip system of previous increment was elastic and presently elastoplastic. Here, the trajectory of one step can be divided in two paths as depicted in Fig. 22; one is elastic and the other is elastoplastic.

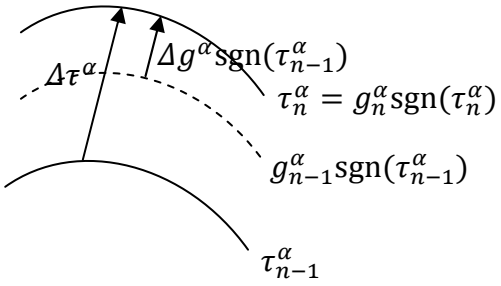

Fig. 22 Division of trajectory in one step into two paths (elastic and elastoplastic).

In this case, (131) can be rewritten as:

$$\begin{aligned} \tau_{n-1}^{\alpha} + \Delta\tau^{\alpha} &= \mathrm{sgn}(\tau_{n-1}^{\alpha}) g_{n-1}^{\alpha} + \mathrm{sgn}(\tau_n^{\alpha}) \Delta g^{\alpha} \ , \\ \sigma_{ij} p_{ij}^{\alpha} + \Delta\sigma_{ij} p_{ij}^{\alpha} &= \mathrm{sgn}(\tau_{n-1}^{\alpha}) g_{n-1}^{\alpha} + \sum_{\beta} h^{\alpha\beta} \Delta\gamma^{\beta} \ . \end{aligned} \tag{136}$$

Following Hutchinson model, we obtain the final form of slip increment.

$$\Delta\gamma^{\alpha} = \sum_{\beta} Y^{\alpha\beta} \left(\sigma_{ij} p_{ij}^{\beta} + C_{ijkl} \Delta\varepsilon_{kl} p_{ij}^{\beta} - \mathrm{sgn}(\tau_{n-1}^{\alpha}) g_{n-1}^{\alpha} \right) \ . \tag{137}$$

We have performed FFT computations of uniaxial tensile tests to compare the two approaches; (135) and (137).

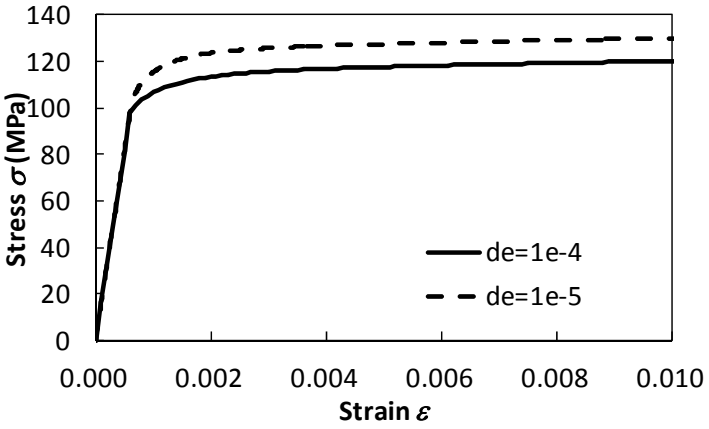

Fig. 23 Calculated stress-strain curves with different strain increment par step.

Fig. 23 shows calculated stress/strain curves with strain increment per step of 10^{-4} and 10^{-5} with relation (135). The case of large strain increment per step shows softer relation. This is because large strain increment causes rapid plasticisation even though previous stress condition remains elastic. This occurs when elastic-plastic test is done implicitly; the current stress value is employed to judge if elastic or elastoplastic. If it is explicit, the relation becomes contrary consequence (large strain increment causes harder relation).

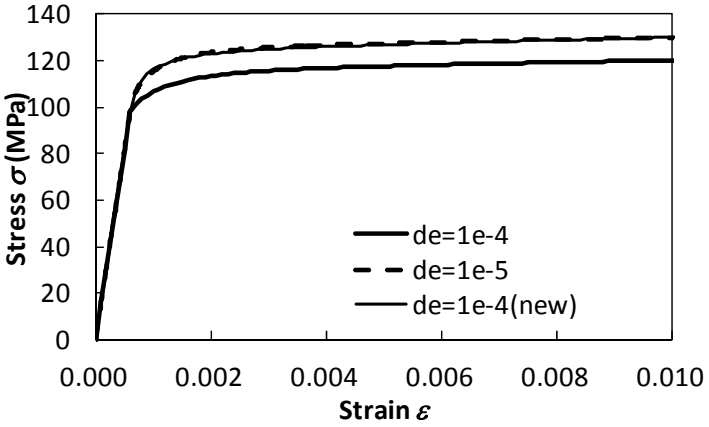

Fig. 24 Calculated stress-strain curves taken into consideration of case 1 and 2.

Fig. 24 is a comparison among two different strain increments (10^{-4} and 10^{-5}) in one step with using equation (135) and the case of increment 10^{-4} using equation (137). The result is in good agreement with the reference solution even though the strain increment is rather large. These comparisons point out the efficiency of the proposed procedure.

This kind of procedure may be indispensable for the stress concentration problems, etc, where strain increment cannot be controlled to be enough small.

4.1.7 Identification of material parameters for S45C carbon steel

In order to simulate the transformation plasticity of S45C material, parameters are fitted to reproduce the experimental data (Fig. 12). In this calculation, the Hutchinson model [59] and a hardening model by Peirce *et al*. [48] are applied (see 2.4).

When τ^α is equal to CRSS, the slip system activates. Let γ^α a strain value along α slip surface, then the plastic strain rate can be expressed as a summation of plastic shear strain rate on each slip system such that

$$\dot{\varepsilon}_{ij}^p = \sum_\alpha \dot{\gamma}^\alpha p_{ij}^\alpha \ . \tag{138}$$

Thus, we obtain the local constitutive equation of crystalline materials.

$$\dot{\sigma}_{ij} = C_{ijkl}\dot{\varepsilon}_{kl} - \sum_\alpha \dot{\gamma}^\alpha C_{ijkl} p_{kl}^\alpha \ , \tag{139}$$

$$\begin{cases} \tau^\alpha = g^\alpha \\ \tau^\alpha < g^\alpha \end{cases} \quad \text{with} \quad \begin{matrix} \dot{\gamma}^\alpha \geq 0 \\ \dot{\gamma}^\alpha = 0 \end{matrix} . \tag{140}$$

Because materials harden with plastic deformation, the CRSS of α slip system is considered to be associated with shear strain rate [47], such that

$$\dot{g}^\alpha = \sum_\beta h^{\alpha\beta} \left|\dot{\gamma}^\beta\right| \ , \tag{141}$$

where $h^{\alpha\beta}$ is hardening coefficient. If $\alpha = \beta$, $h^{\alpha\beta}$ is called self hardening. Otherwise, it is called latent hardening. If $h^{\alpha\beta}$ is zero, the model describes elasto-perfect plastic material. For the hardening materials, hardening parameter can be expressed by following equation.

$$h^{\alpha\alpha} = h = H_0 \operatorname{sech}^2 \left[\frac{H_0 \sum_\beta \gamma^\beta}{\tau_s - \tau_0}\right] \ , \tag{142}$$

$$h^{\alpha\beta} = qh + (1-q)h\delta_{\alpha\beta} \ , \tag{143}$$

where H_0 is a coefficient, τ_0 is an initial yield stress value and τ_s is a saturate stress value. The parameter q takes values from 1.0 to 1.4 depending on the material. Here, γ^α takes values to accommodate continuum body.

The set of optimised parameters is shown in Table 15. The macroscopic stress/strain relation of parent phase (f.c.c.) and daughter phase (b.c.c.) are depicted in Fig. 25.

Table 15 Parameters for crystal plasticity calculation.

	parent phase	daughter phase
Bulk modulus (GPa)	135,833	150,000
Shear modulus (GPa)	62,692	69,231
H_0 (MPa)	10	550
τ_0 (MPa)	30	100
τ_s (MPa)	40	130
q	1.0	1.0
Constitutive model	Hutchinson	
Number of grains	100	100

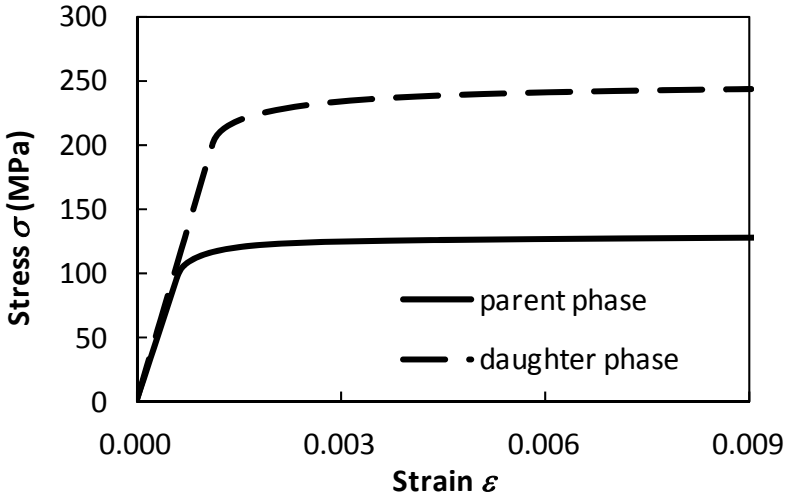

Fig. 25 Macroscopic stress/strain curve of parent and daughter phases.

4.1.8 Phase transformation model

Here we consider the isothermal phase transformation. In this case, there will be no thermal strain; it simplifies the problem and it provides the basic results of transformation plasticity.

The local transformation expansion coefficient is defined to be $\beta = 1.536 \times 10^{-3}$. New phase seeds are spread randomly and then start to grow isotropically. For computational reasons, very fine intermediate area, where the volume fraction of new phase takes values $0 \leq \xi \leq 1$, is defined surrounding the surface of new phase. The sample image of new grains (red coloured circles) which are spread and expanding is shown in Fig. 26.

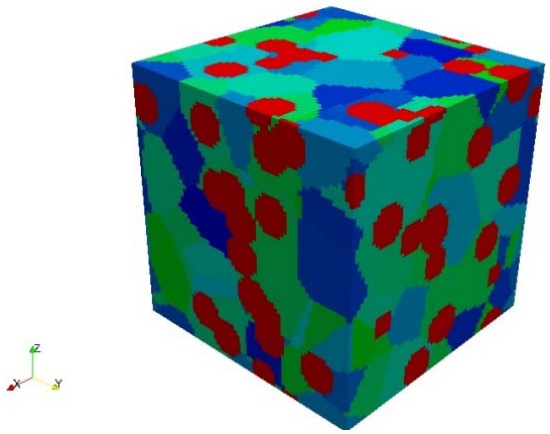

Fig. 26 Austenite grains and transformed new grains (red coloured circles).

Within the intermediate area, the volume fraction of new phase yields following KJMA type equation [44]:

$$\xi = 1 - \exp(-bt^n) \ . \tag{144}$$

The calculations start with 100% original grains which are subsequently loaded at the stress values vary from -90MPa to 90MPa. The applied stress will be hold until phase transformation is complete, i.e. 100% daughter phase.

When the volume fraction exceeds 50%, the constitutive relation in the intermediate zone takes the value of new b.c.c. phase. At the same time, the crystallographic orientation will be changed according to Kurdjumow-Sachs relation [68] expressed in Fig. 27. The accumulated plastic strain is considered not to inherit to a daughter phase. Thus, the hardness of daughter phase is independent of plastic deformation before phase transformation.

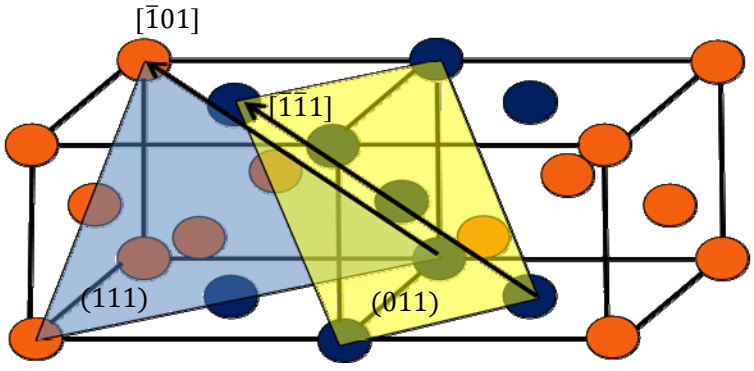

Orange points: f.c.c., Blue points: b.c.c.

Fig. 27 Kurdjumow-Sachs relation for f.c.c to b.c.c. phase transformation.

According to this relation, (111) and $[\bar{1}01]$ of f.c.c. phase are parallel to (011) and $[\bar{1}\bar{1}1]$ of first variant of b.c.c.. The corresponding rotation is $45^{\cdot}$ around the axis $< 110 >$. Thus, the rotation matrix $A^{\gamma\to\alpha}$ can be found by inserting $(n_1, n_2, n_3) = (1,1,0)$ and $\theta_i = 45^{\cdot}$ into following rotation matrix:

$$V_i = \begin{pmatrix} n_1^2(1-\cos\theta_i)+\cos\theta_i & n_1n_2(1-\cos\theta_i)-n_3\sin\theta_i & n_1n_3(1-\cos\theta_i)+n_2\sin\theta_i \\ n_2n_1(1-\cos\theta_i)+n_3\sin\theta_i & n_2^2(1-\cos\theta_i)+\cos\theta_i & n_2n_3(1-\cos\theta_i)-n_1\sin\theta_i \\ n_3n_1(1-\cos\theta_i)-n_2\sin\theta_i & n_3n_2(1-\cos\theta_i)+n_1\sin\theta_i & n_3^2(1-\cos\theta_i)+\cos\theta_i \end{pmatrix}. \quad (145)$$

It is known that there are 24 possible variants that b.c.c. materials take after phase transformation [68]. When we call the first variants obtained by Fig. 27, the relation between the variant 1 (V_1) and the other variants are given in Table 16.

Table 16 Crystallographic relation between V_1 and other variants [75].

Variant No.	Parallel surface	Parallel direction	Rotation axis	Angle(deg)
1	$(111)_\gamma//(011)_\alpha$	$[\bar{1}01]_\gamma//[\bar{1}\bar{1}1]_\alpha$	-	-
2		$[\bar{1}01]_\gamma//[\bar{1}1\bar{1}]_\alpha$	[0.5774,0.5774, −0.5774]	60.00
3		$[01\bar{1}]_\gamma//[\bar{1}\bar{1}1]_\alpha$	[0.0000,0.7071,0.7071]	60.00
4		$[01\bar{1}]_\gamma//[\bar{1}1\bar{1}]_\alpha$	[0.0000, −0.7071, −0.7071]	10.53
5		$[1\bar{1}0]_\gamma//[\bar{1}\bar{1}1]_\alpha$	[0.0000, −0.7071, −0.7071]	60.00
6		$[1\bar{1}0]_\gamma//[\bar{1}1\bar{1}]_\alpha$	[0.0000,0.7071,0.7071]	49.47
7	$(1\bar{1}1)_\gamma//(011)_\alpha$	$[10\bar{1}]_\gamma//[\bar{1}\bar{1}1]_\alpha$	[−0.5774, −0.5774,0.5774]	49.47
8		$[10\bar{1}]_\gamma//[\bar{1}1\bar{1}]_\alpha$	[0.5774,0.5774, −0.5774]	10.53
9		$[\bar{1}\bar{1}0]_\gamma//[\bar{1}\bar{1}1]_\alpha$	[−0.615,0.1862, −0.7667]	50.51
10		$[\bar{1}\bar{1}0]_\gamma//[\bar{1}1\bar{1}]_\alpha$	[−0.7387, −0.4625,0.4904]	50.51
11		$[011]_\gamma//[\bar{1}\bar{1}1]_\alpha$	[0.9329,0.3543,0.0650]	14.88
12		$[011]_\gamma//[\bar{1}1\bar{1}]_\alpha$	[−0.3568,0.6029,0.7136]	57.21
13	$(\bar{1}11)_\gamma//(011)_\alpha$	$[0\bar{1}1]_\gamma//[\bar{1}\bar{1}1]_\alpha$	[0.3543, −0.9329, −0.0650]	14.88
14		$[0\bar{1}1]_\gamma//[\bar{1}1\bar{1}]_\alpha$	[−0.4904,0.4625, −0.7387]	50.51
15		$[\bar{1}0\bar{1}]_\gamma//[\bar{1}\bar{1}1]_\alpha$	[−0.7384, −0.2461,0.6278]	57.2
16		$[\bar{1}0\bar{1}]_\gamma//[\bar{1}1\bar{1}]_\alpha$	[0.6589, −0.6589, −0.3628]	20.61
17		$[110]_\gamma//[\bar{1}\bar{1}1]_\alpha$	[−0.6589,0.3628, −0.6589]	51.73
18		$[110]_\gamma//[\bar{1}1\bar{1}]_\alpha$	[−0.7193, −0.3022,0.6255]	47.11
19	$(11\bar{1})_\gamma//(011)_\alpha$	$[\bar{1}10]_\gamma//[\bar{1}\bar{1}1]_\alpha$	[−0.1862,0.7667,0.6145]	50.51
20		$[\bar{1}10]_\gamma//[\bar{1}1\bar{1}]_\alpha$	[0.3568,0.714, −0.6029]	57.21
21		$[0\bar{1}\bar{1}]_\gamma//[\bar{1}\bar{1}1]_\alpha$	[0.9551,0.0000, −0.2962]	20.61
22		$[0\bar{1}\bar{1}]_\gamma//[\bar{1}1\bar{1}]_\alpha$	[−0.3022,0.626,0.7193]	47.11
23		$[101]_\gamma//[\bar{1}\bar{1}1]_\alpha$	[−0.2461, −0.6278, −0.7384]	57.21
24		$[101]_\gamma//[\bar{1}1\bar{1}]_\alpha$	[0.9121, −0.4100,0.0000]	21.06

Let V_i the *i*-th variant rotation matrix from V_1, the rotation matrix from f.c.c. to b.c.c. can be written as follows:

$$A_i^{\gamma\to\alpha} = A^{\gamma\to\alpha}V_i \ . \tag{146}$$

Note that equation (145) gives the 7-th variant shown in Table 16.

In this calculation, these 24 variants are taken randomly.

4.1.9 Results and discussions

During phase transformation, because of the difference in volume between two phases,

stress and plastic strain occurs at the grain scale. Fig. 28 shows the evolution of volume fraction of new phase, equivalent stress and equivalent plastic strain during phase transformation. The volume fraction of parent phase increases with time (a-1) as randomly spread new germination grows forming spherical grains. When two or more grains come across each other, the surface separating grains will be frontiers of those grains (b-1). Along with the growth of new grains, local stress occurs because of the volumetric difference between two phases (a-2). The equivalent stress is higher in daughter phase than in parent phase (a-2). This is because yield stress of daughter phase is larger than that of parent phase. Although the equivalent stress is smaller in parent phase, equivalent plastic strain value is larger in parent phase than in daughter phase when average transformed phase are 3% and 50% (a-3), (a-4), (b-3) and (b-4). Apart from 99 % transformed condition (c-3), the equivalent plastic strain in parent phase shows that it has relatively large value when the transformed new particles (daughter phase) are located in its neighbour (for 99% transformed condition, the equivalent plastic strain in parent phase disappears because of the absence of parent phase.).

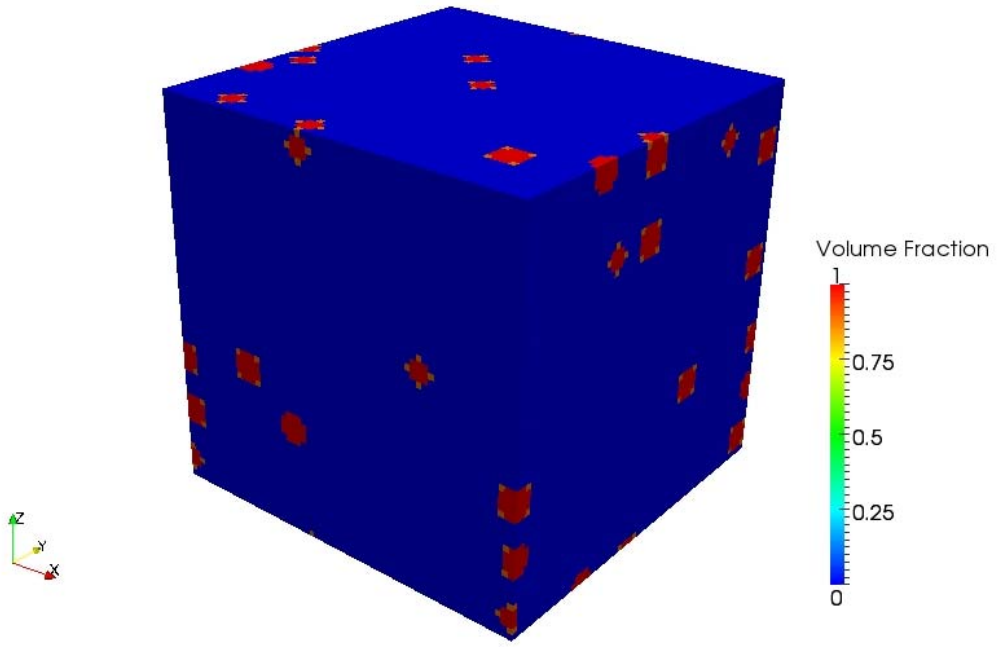

(a-1) Volume fraction of parent phase (3% transformed)

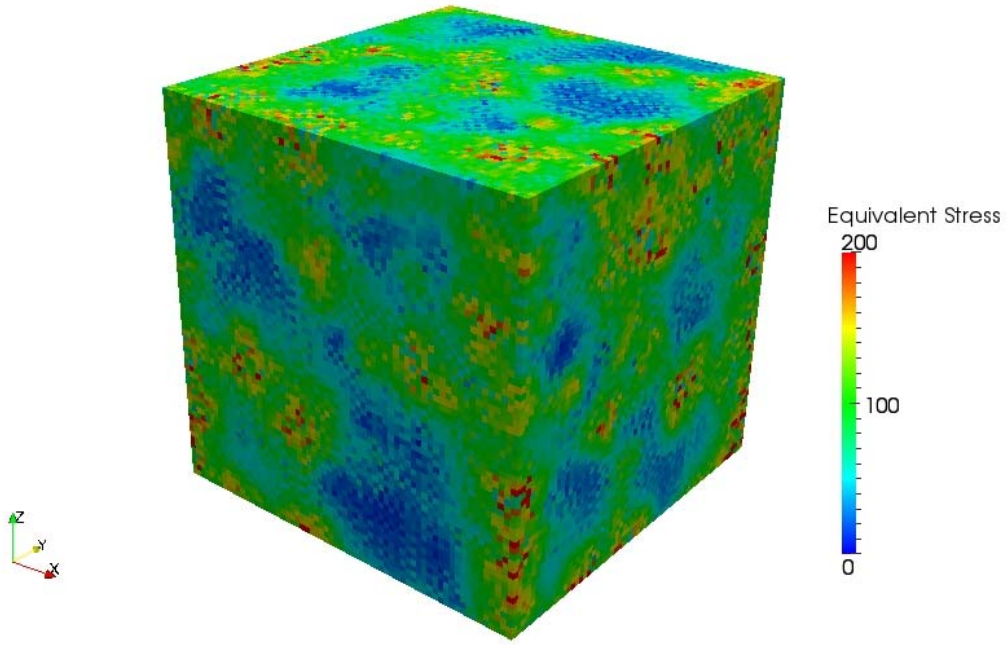

(a-2) Equivalent stress (3% transformed)

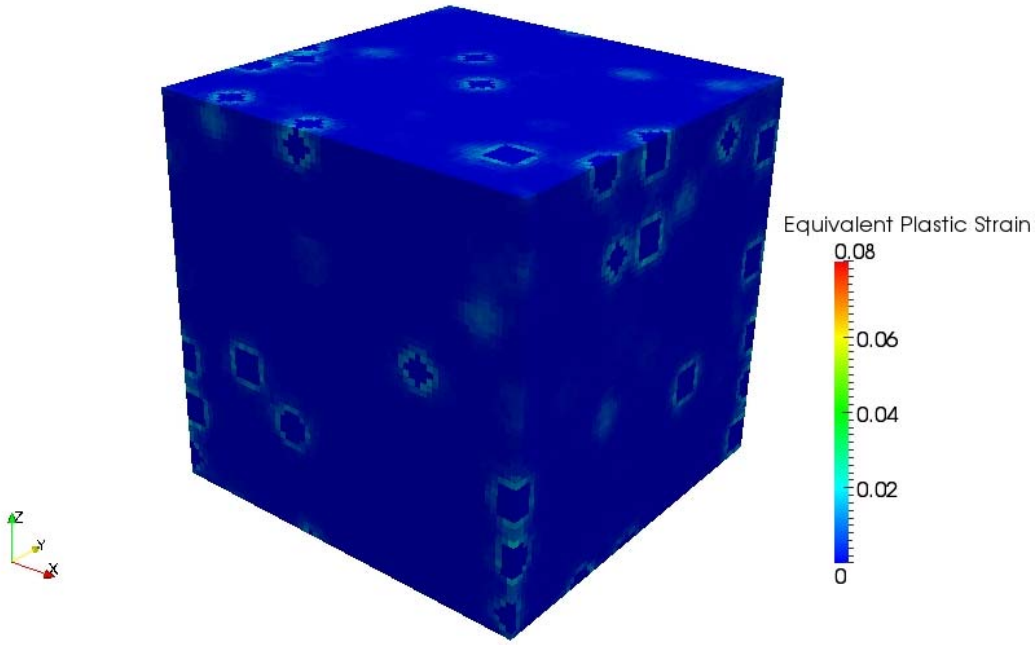

(a-3) Equivalent plastic strain of parent phase (3% transformed)

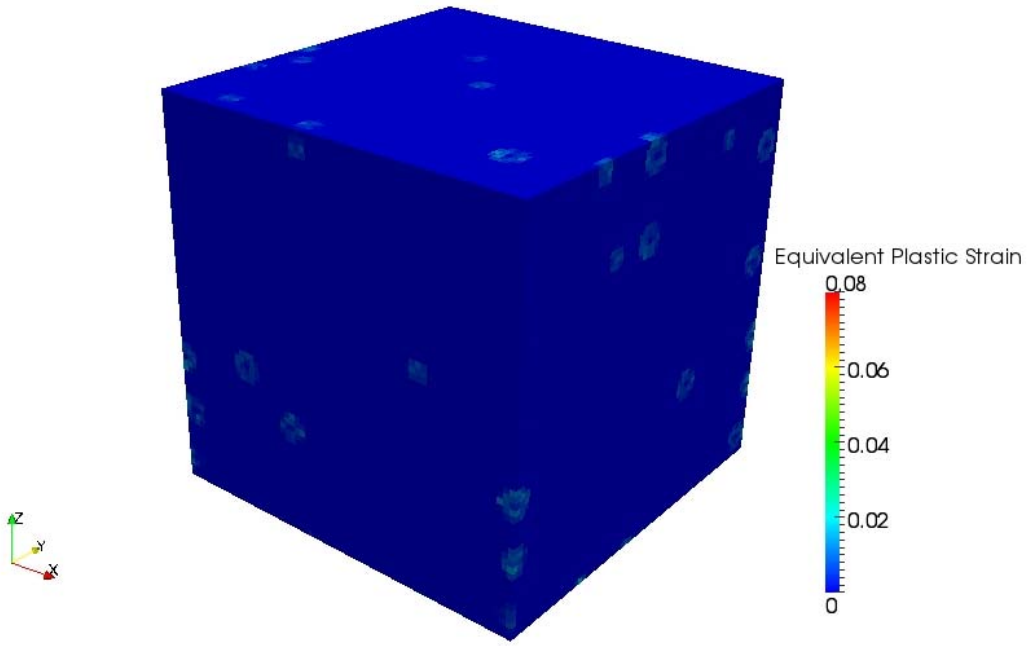

(a-4) Equivalent plastic strain of daughter phase (3% transformed)

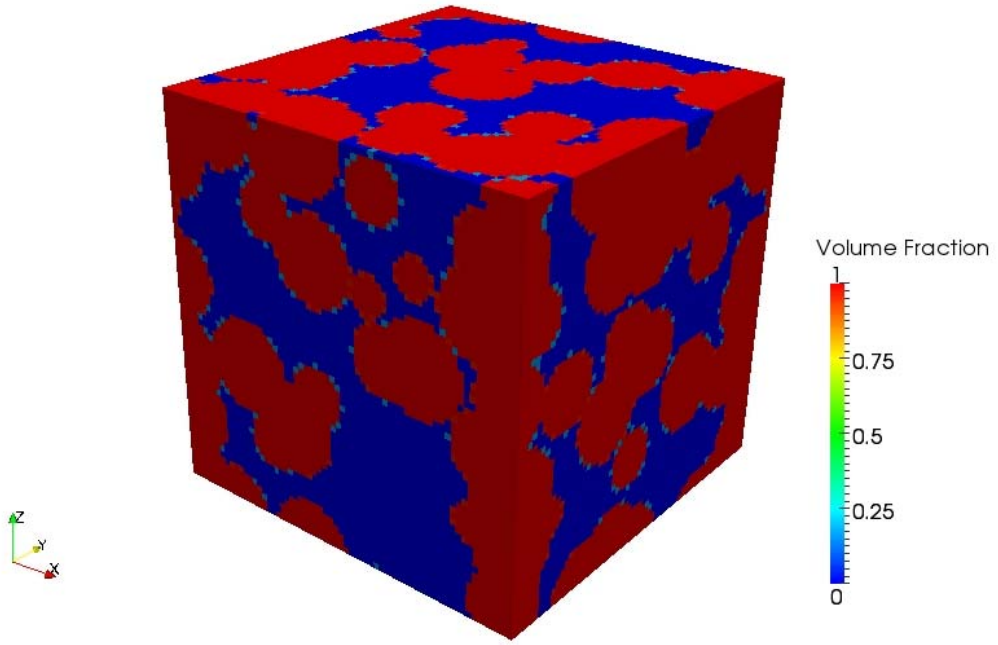

(b-1) Volume fraction of parent phase (50% transformed)

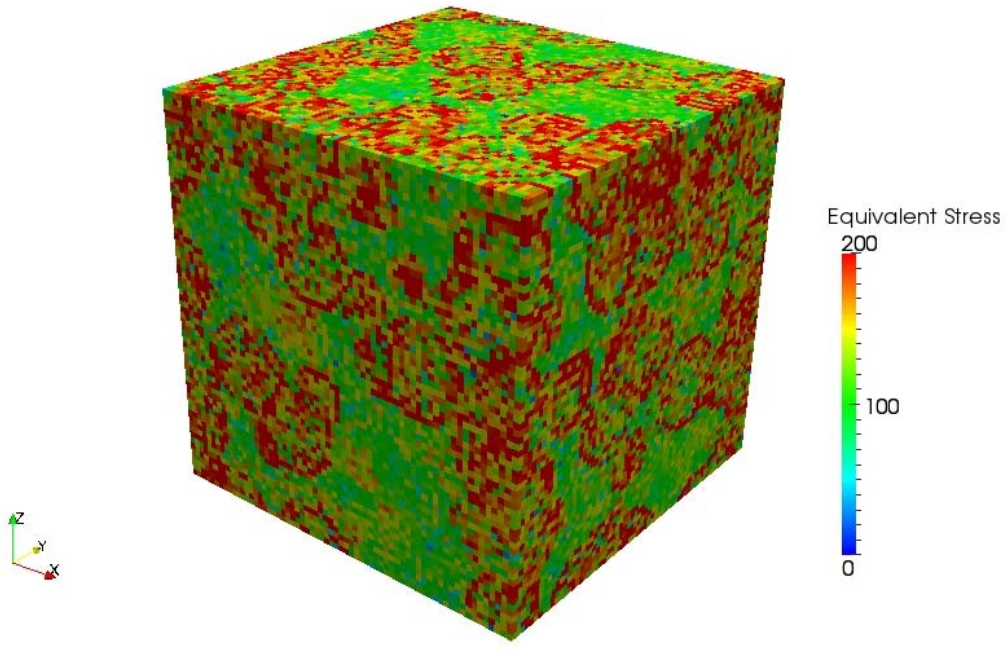

(b-2) Equivalent stress (50% transformed)

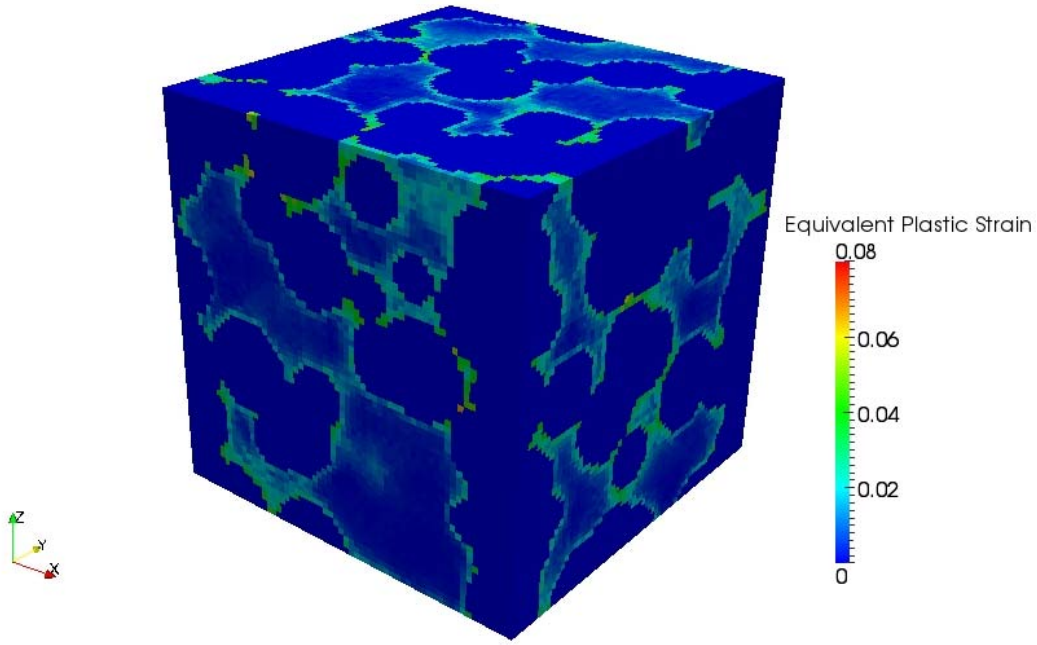

(b-3) Equivalent plastic strain of parent phase (50% transformed)

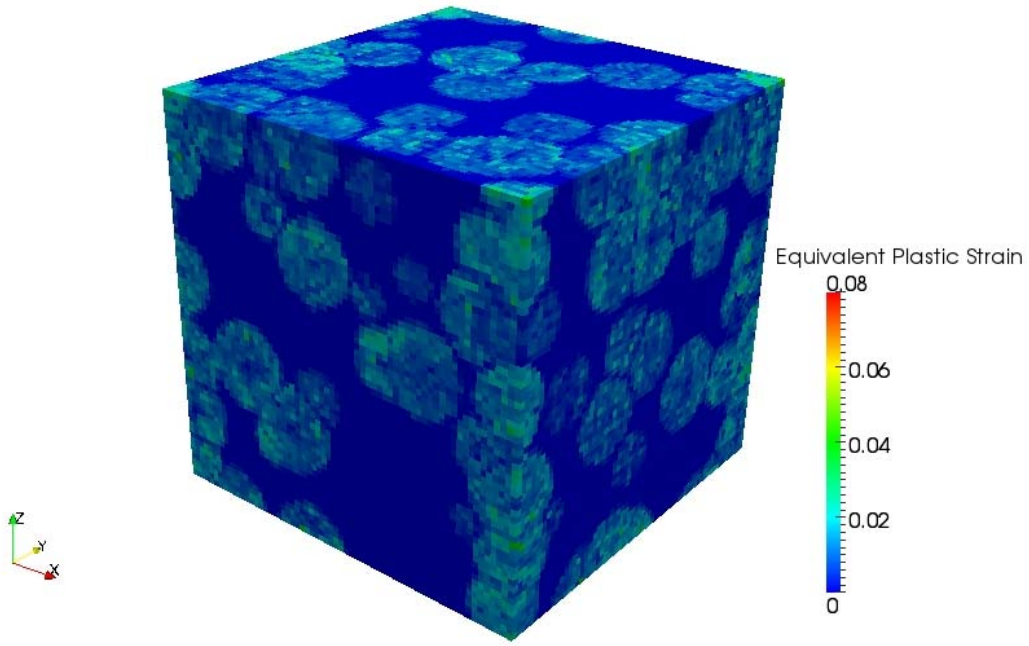

(b-4) Equivalent plastic strain of daughter phase (50% transformed)

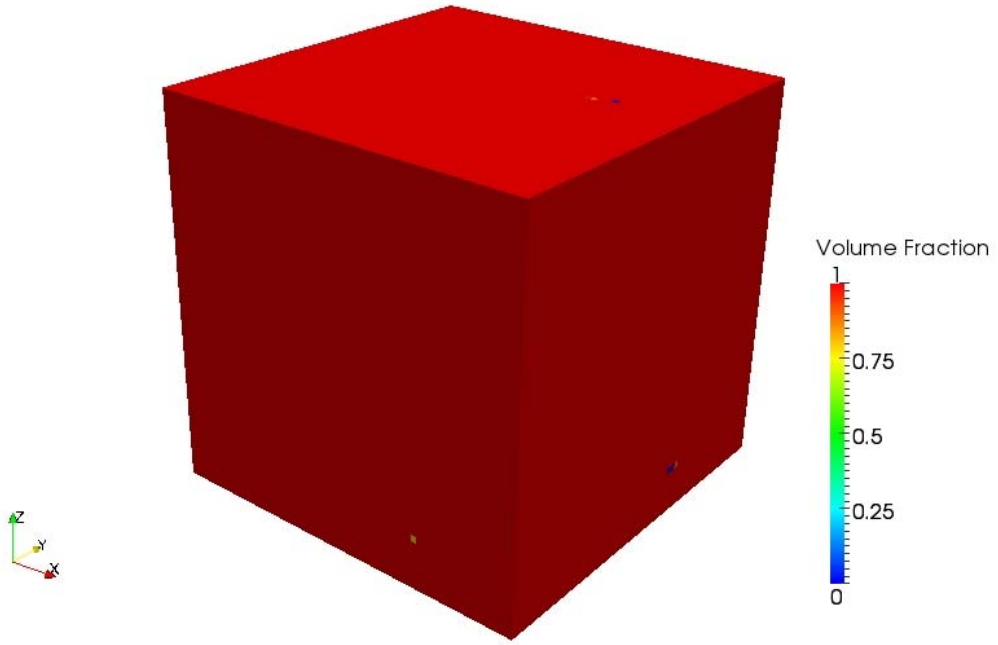

(c-1) Volume fraction of parent phase (99% transformed)

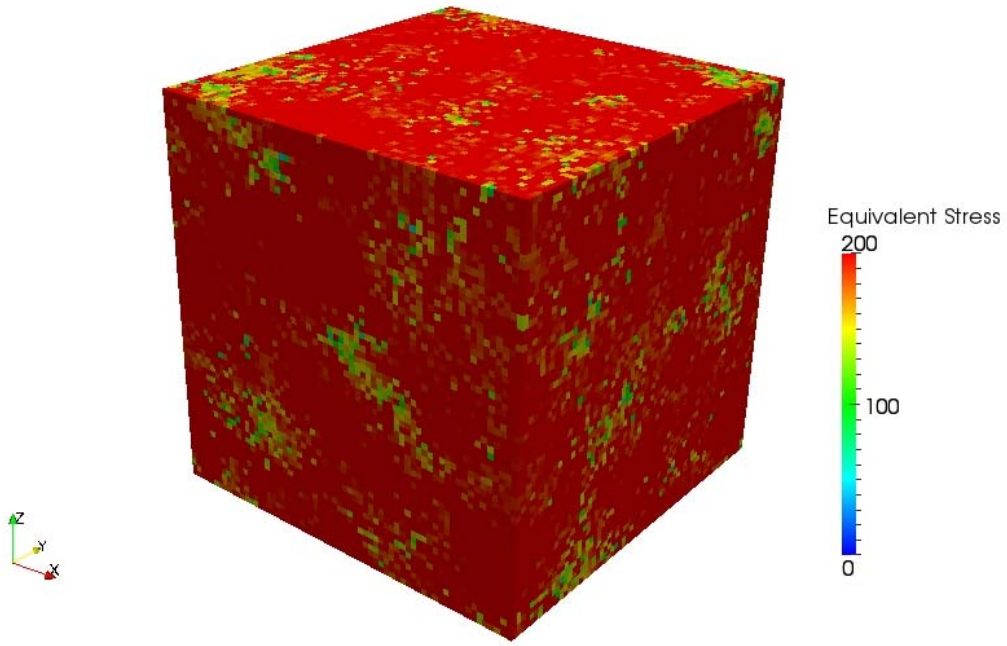

(c-2) Equivalent stress (99% transformed)

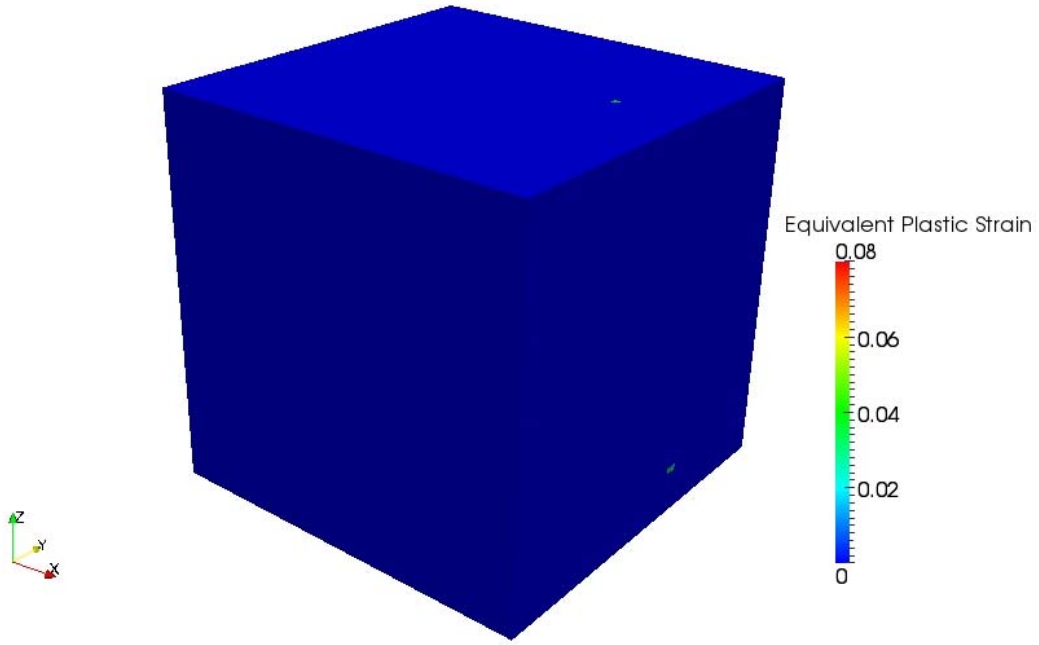

(c-3) Equivalent plastic strain of parent phase (99% transformed)

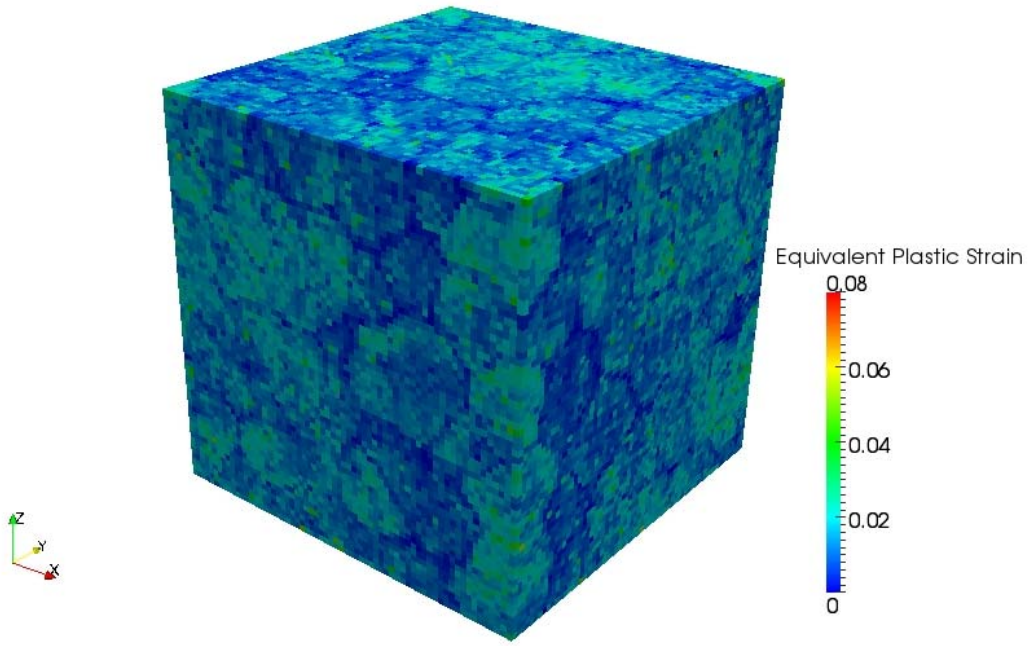

(c-4) Equivalent plastic strain of daughter phase (99% transformed)

Fig. 28 Evolution of macroscopic plastic strain caused by phase transformation.

The evolution of the average volume fraction of new phase under stress free condition is shown in Fig. 29 (a). During the phase transformation, the strain values change according to the magnitude of applied stress. This evolution of strain is depicted in Fig. 29 (b). As the applied stress value increases, the resultant total strain value also increases. As seen above, transformation plasticity is naturally obtained along with evolution of phase transformation without any artificial term like macroscopic transformation plastic strain.

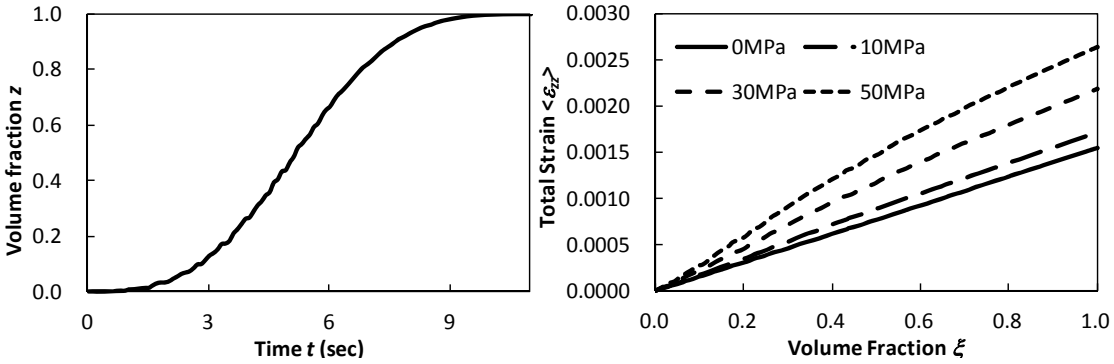

(a) Evolution of volume fraction (b) Evolution of total strain

Fig. 29 Evolution of volume fraction of new phase and macroscopic total strain.

The relation between total strain evolution during phase transformation and volume fraction is almost linear when applied stress is not so large.

4.2 Numerical investigation of metallurgical and mechanical interaction effects on transformation plasticity

The difference of conditions between industrial and experimental ones sometimes causes significant effect. In fact, the phenomena of industrial processes are generally so dynamic and severe that one fails to duplicate the equivalent conditions in spite of many efforts. For example, the mode and rapidness of deformation are much faster in the real processes than those in the laboratories. It should be noted that the perturbation in mass production conditions can be also significant because it may result in thermal, metallurgical and mechanical heterogeneity of materials.

To take some examples, hot rolling processes introduce high dislocation density inside materials, which causes mechanical hardening. At the same time, crystallographic orientations change because of rigid body rotation of lattice during rolling, which results in texture. Subsequently, the rolled materials will be subject to cooling. In the very short time period between rolling and cooling, important metallurgical events occur, such as static recovery, recrystallisation, and grain growth.

In this context, it is absolutely important to know the sensitivity of each effect which arises from the differences in order to minimise the discrepancies among experimental results and real processes. The numerical simulations allow to distinguish individual parameters and to know their relative effect.

4.2.1 Texture

Almost all the existing experimental results concerns transformation plasticity of fully annealed materials. Although austenitic phase transformation inherits crystallographic orientation on certain conditions, the texture of specimen is expected to be different from those of industrial ones.

The calculation results of transformation plasticity presented above were obtained for isotropic polycrystals. This assumption is, on the whole, in good agreement with Leblond's model [15] (ideal cases). In contrast, it is known that materials such as sheets and plates after rolling have texture so that they have anisotropic mechanical component. In this section, the texture of hot rolled sheet is observed, which will be taken into account to the transformation plasticity calculations, and compared with the results of random orientations.

4.2.1.1 Texture observation of hot rolling sheet products

The classical low carbon hot rolled steel sheet is investigated in order to determine the

texture effect on transformation plasticity. The crystallographic orientation can be detected by taking advantage of the EBSD (Electron Back Scattering Diffraction) technique. The data are taken every 5 micro metre that will count 98213 points in total. The inverse pole figures of planes perpendicular to normal direction and rolling direction are shown in Fig. 30. Although a slight difference of texture between surface and centre is observed from Fig. 30, for the simplicity, it is not taken into account.

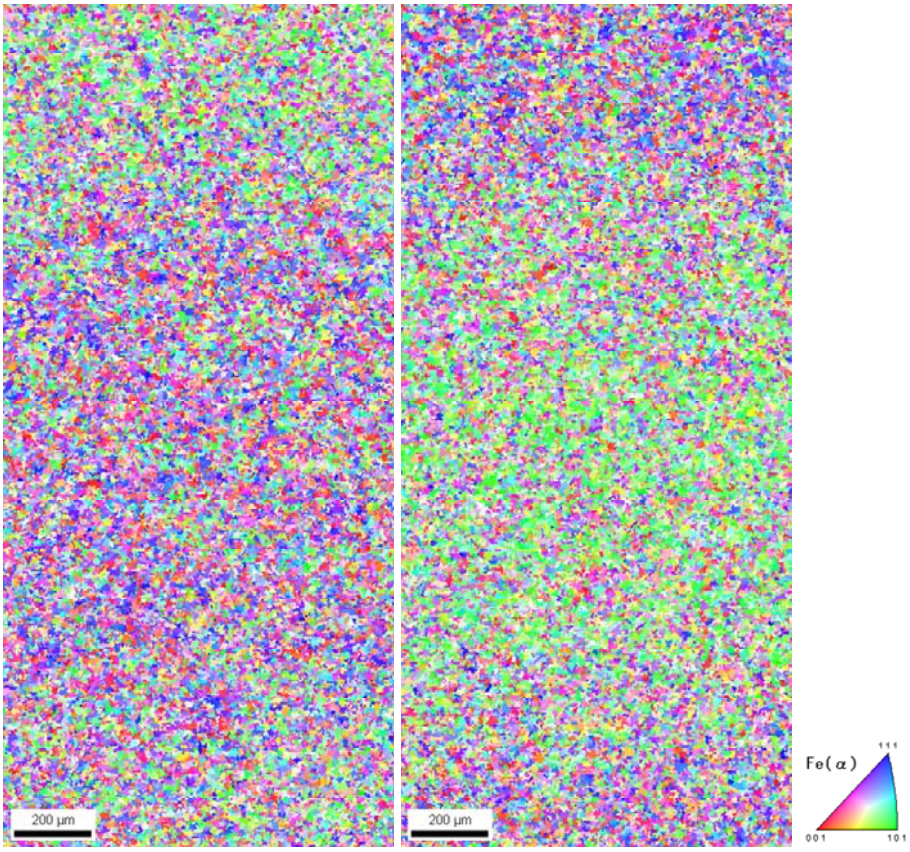

(a) ND (b) RD

Fig. 30 Inverse Pole Figure of hot rolled low carbon steel sheet.

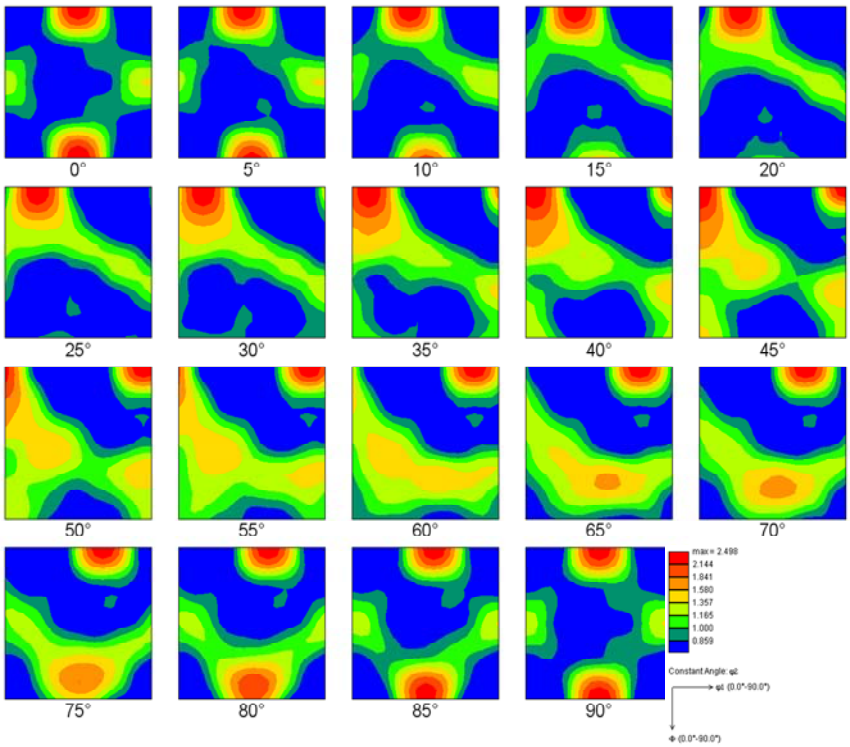

Fig. 31 ODF of hot rolled sheet after phase transformation (Ferrite).

For the same specimen, ODF is depicted in Fig. 31. Note that this is the texture at room temperature. It means that the material experienced phase transformation after rolling from austenitic phase to ferritic phase. Thus, in order to know initial austenitic orientations, these ferritic orientations have to be inversed into austenitic ones. Cabus [68] has proved in her PhD thesis that the initial texture is predictable from final texture by adopting inverse K-S relation.

By using this theory, the initial austenite texture is calculated and depicted in Fig. 32. Both ferrite and austenite texture are similar to those of experimental observations by Cabus [68].

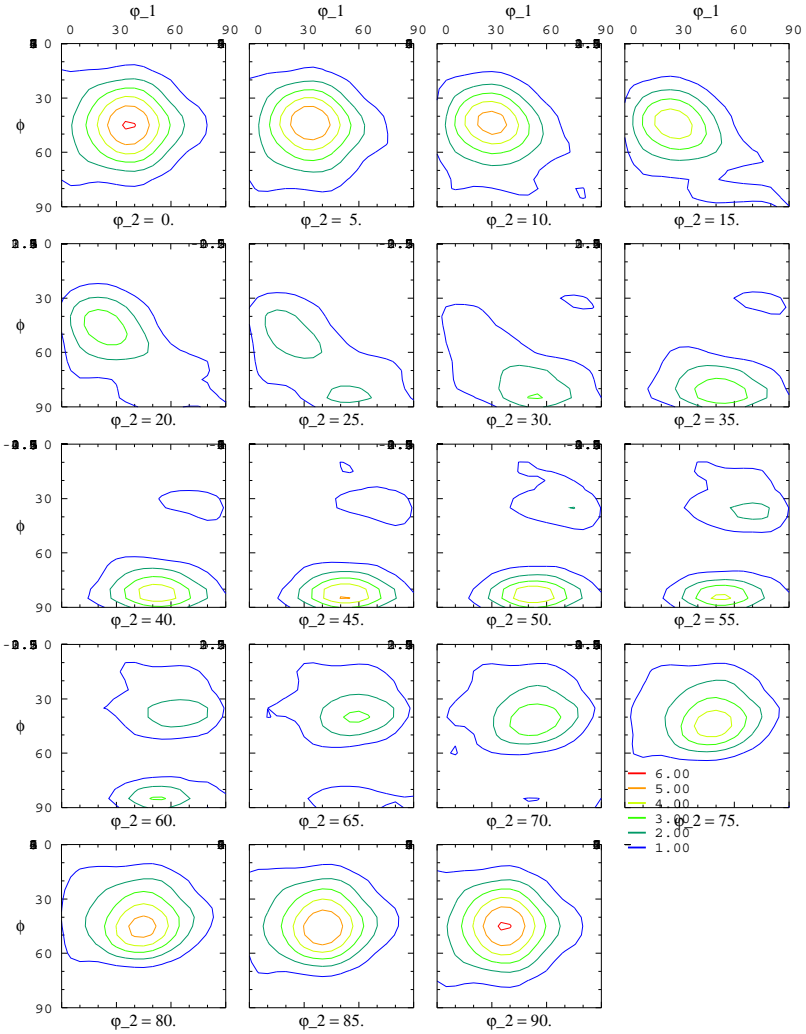

Fig. 32 ODF prediction of hot rolled sheet before phase transformation (austenite).

4.2.1.2 Incorporation of texture effect into transformation plasticity calculation

To perform transformation plasticity calculations, the obtained texture results for austenite phase have to be incorporated. To clarify sole texture effect, we consider an isotropic morphologic texture with uniform grain size.

First, the number of orientations is reduced with the volume fraction information into one set which is feasible for calculations (1645 orientations).

Second, crystalline orientation is assigned to each grain according to the volumetric fraction information.

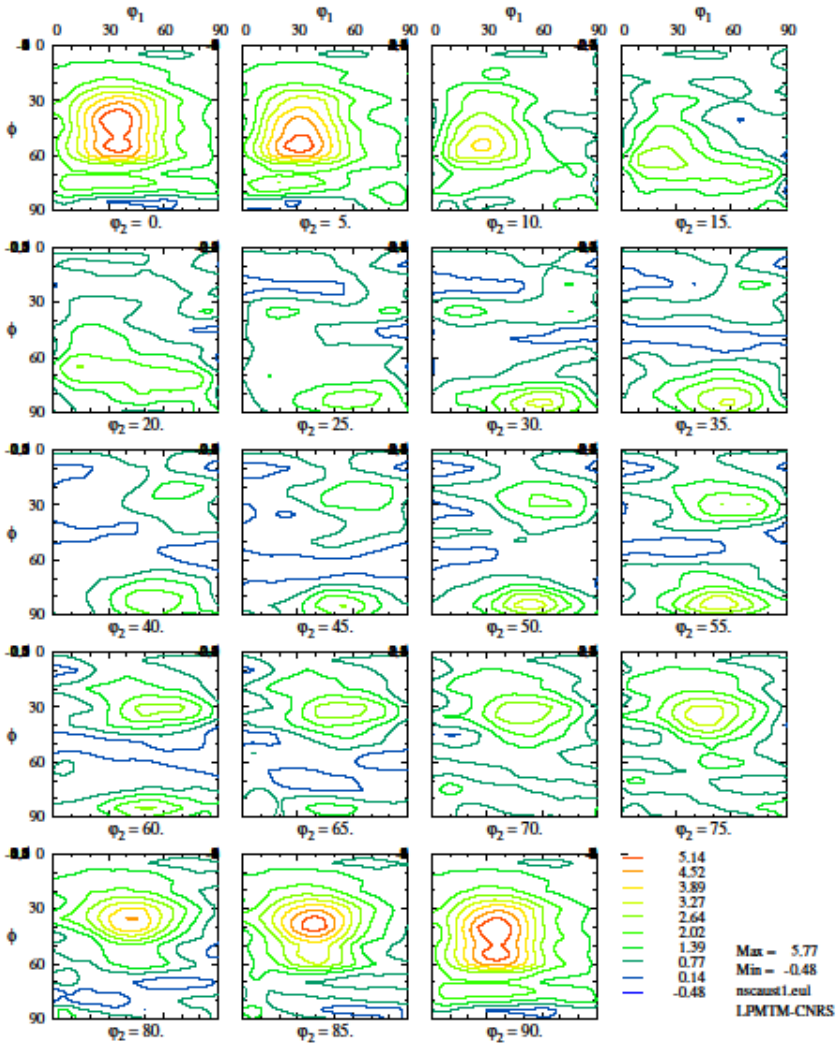

Fig. 33 ODF of reduced number of orientations (1645 orientations with volume fraction).

The sample ODF figure of the Voronoi microstructure obtained by using this methodology is shown in Fig. 34. By comparing Fig. 33 with Fig. 34, the reduced texture well matches original texture information (Fig. 32). The more grains is introduced, the more precise is the texture. The maximum number of grains is defined by the memory space and calculation time.

In this calculation, the following case is adopted; 2000 grains inside a unit-cell of 128^3 voxels.

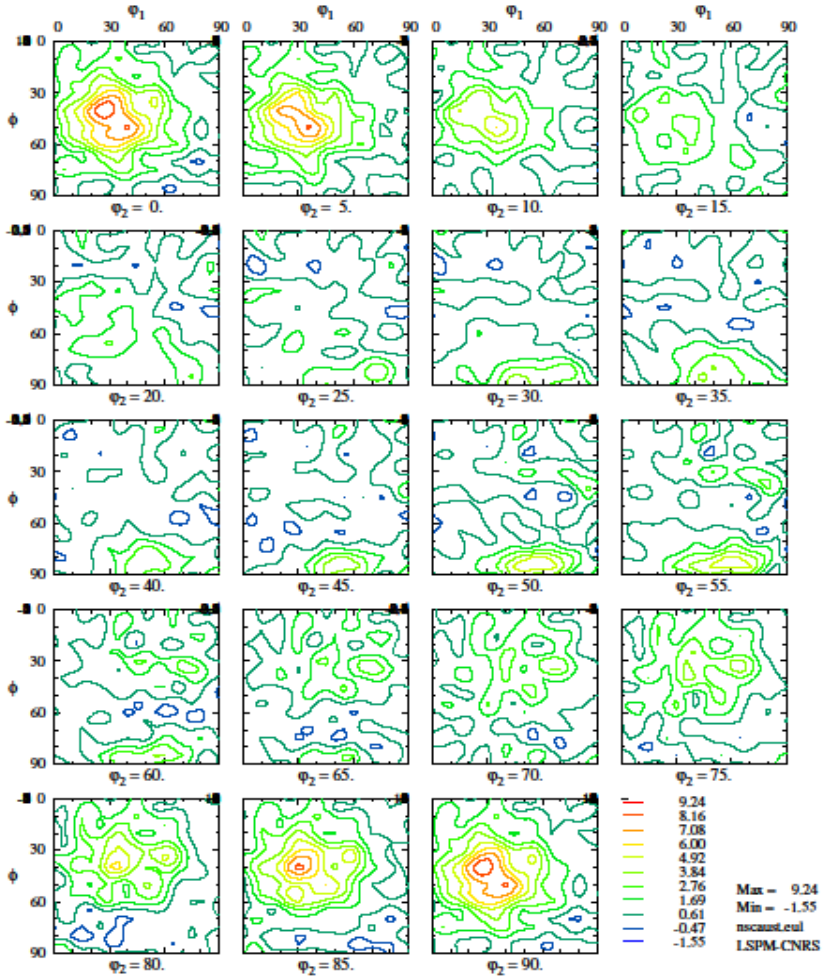

Fig. 34 ODF of reduced number of grains (2000 grains).

4.2.1.3 Results and discussions

The calculated transformation plastic strains versus applied stresses are shown in Fig. 35 and Fig. 36 for isotropic and textured polycrystals. Note that the isotropic computations have been performed with a Voronoi tessellation of 2000 cells for an accurate comparison. In order to evaluate the anisotropy effect on transformation plasticity, simulations have been performed for three different uniaxial applied stress conditions; rolling direction (RD), normal direction (ND) and transverse direction (TD).

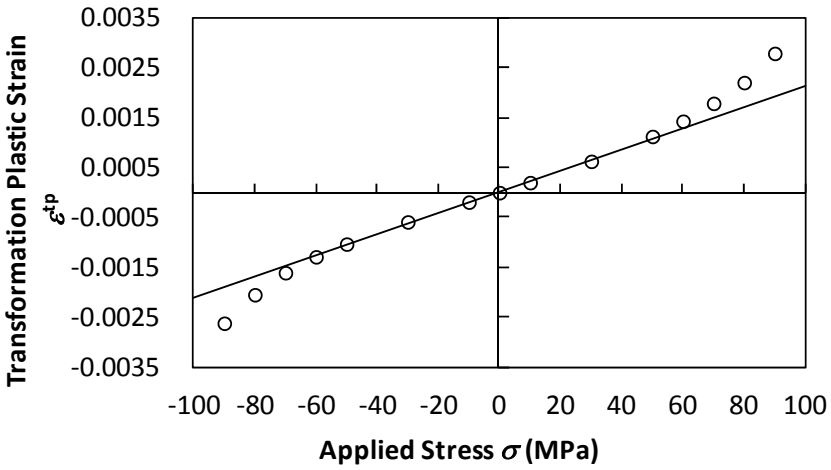

Fig. 35 Transformation plasticity of random orientations (2000 grains in 128^3 voxels).

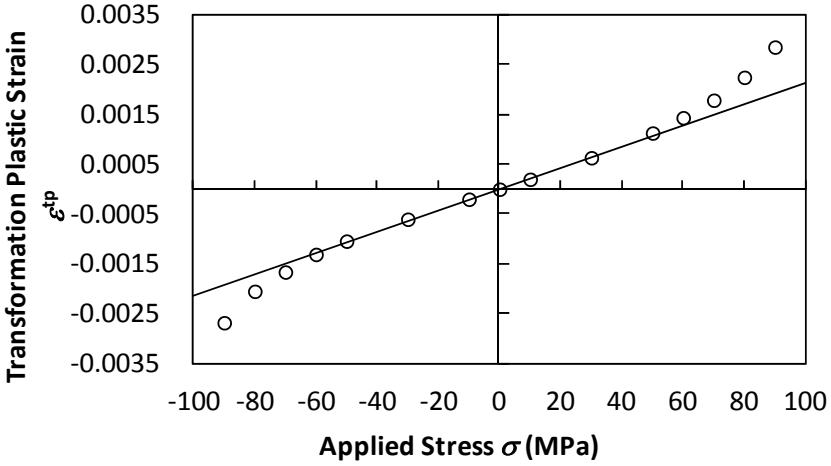

(a) Applied stress – Normal direction (equivalent to *z*-direction)

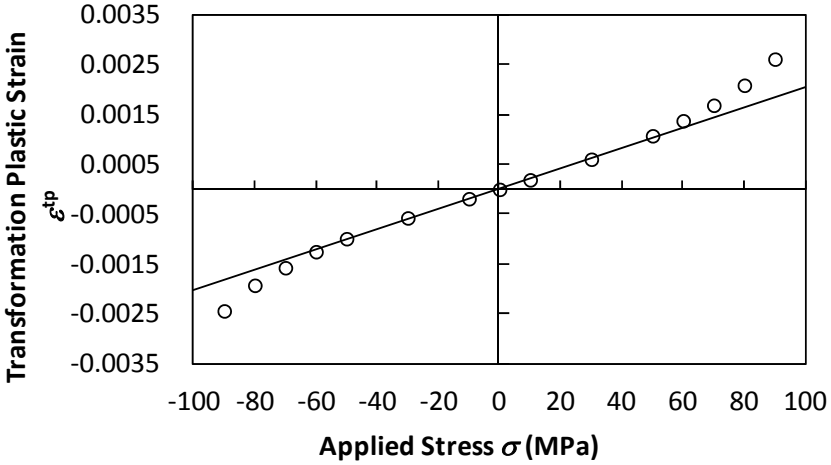

(b) Applied stress – Rolling direction (equivalent to *x*-direction)

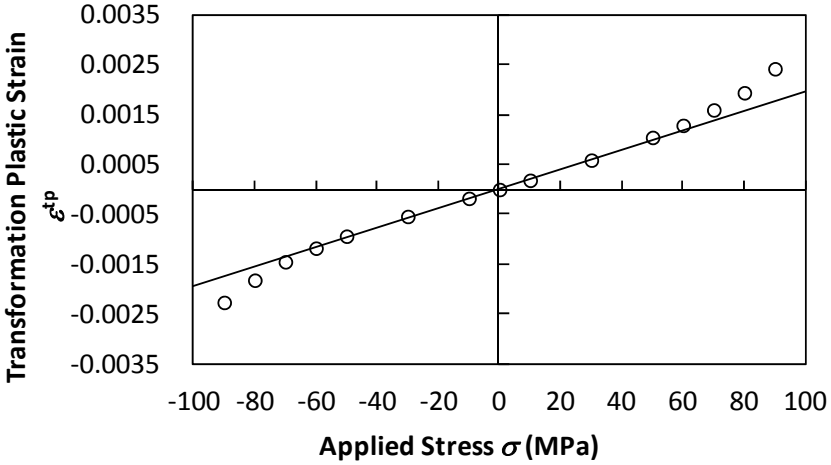

(c) Applied stress – Transverse direction (equivalent to *y*-direction)

Fig. 36 Transformation plasticity of textured polycrystals.

Random : $K_P^+ = 2.25 \times 10^{-5}$ (MPa^{-1}), $K_P^- = 2.06 \times 10^{-5}$ (MPa^{-1})
Texture (RD) : $K_P^+ = 2.15 \times 10^{-5}$ (MPa^{-1}), $K_P^- = 1.98 \times 10^{-5}$ (MPa^{-1})
Texture (ND) : $K_P^+ = 2.25 \times 10^{-5}$ (MPa^{-1}), $K_P^- = 2.08 \times 10^{-5}$ (MPa^{-1})
Texture (TD) : $K_P^+ = 2.09 \times 10^{-5}$ (MPa^{-1}), $K_P^- = 1.87 \times 10^{-5}$ (MPa^{-1})

The results for the random orientation case show no significant difference with our previous results. This means that the number of grains and the discretisation allows to reproduce the transformation plasticity phenomena.
According to the results for ND are the largest transformation plastic coefficient which is equivalent to those of Random case. The RD results are slightly smaller than ND results and TD results are the smallest. These results can be explained by stress/strain curves for each applied stress direction (Fig. 37). The ND direction and Random case (Fig. 25) show the hardest and the TD shows softest, which is the same tendency with transformation plasticity. Thus, it can be concluded that the transformation plasticity of textured polycrystals has the same trend with their yield stresses. This coincides with the claim by Leblond [15].

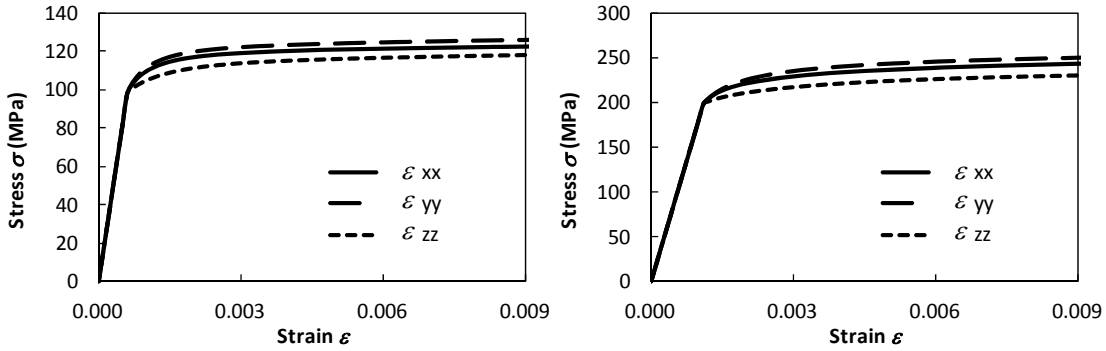

(a) Parent phase (b) Daughter phase

Fig. 37 Stress/strain curves in three directions of each phase (anisotropy effect).

4.2.2 Grain morphology effect

In the previous discussion, the phase transformation is assumed to expand isotropically. In contrast, in the steel producing process, the final grain shape is anisotropic because of plastic deformation such as rolling. In this case, it is expected that the stress field surrounding phase transformation front differs from the one for isotropic growth. In order to analyse the grain morphology effect, two cases of grain growth are examined; a preferential growth along the tensile direction or along a direction perpendicular to it. The final microstructures are shown in Fig. 38. The average aspect ratio is set to be 10:1.

The corresponding transformation plasticity results are presented in Fig. 39.

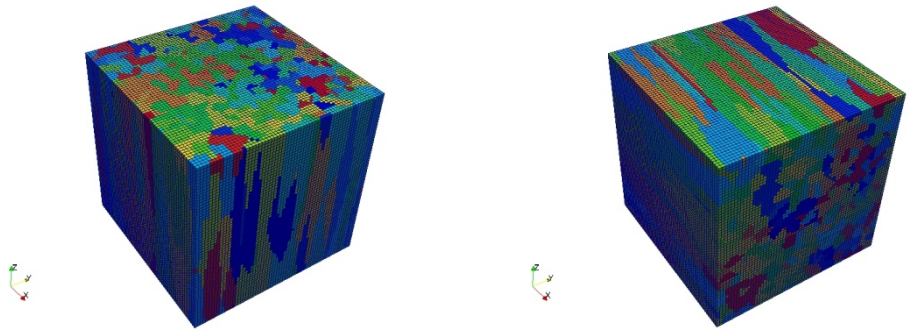

(a) *z*-direction growth (b) *x*-direction growth

Fig. 38 Ellipsoidal Grain morphology of daughter phase.

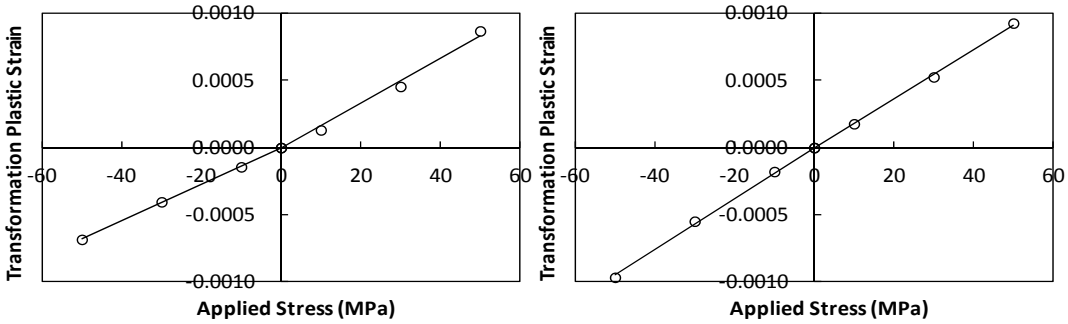

(a) *z*-direction growth (b) *x*-direction growth

Fig. 39 Calculated transformation plasticity with spheroidal daughter grains. (aspect ratio 10:1)

Transformation plastic coefficients along the tensile direction for both cases are calculated for tensile and compressive applied stress.

z direction growth: $K_P^+ = 1.74 \times 10^{-5}$ (MPa^{-1}), $K_P^- = 1.36 \times 10^{-5}$ (MPa^{-1})

x direction growth: $K_P^+ = 1.84 \times 10^{-5}$ (MPa^{-1}), $K_P^- = 1.92 \times 10^{-5}$ (MPa^{-1})

The results indicate that if the preferential grain growth direction is parallel to the direction of applied stress, transformation plastic strains are larger for tensile stress than compressive ones. This is because the transformation is expanding process and hence tensile stress parallel to the direction of applied stress arises during phase transformation. The applied stress enhances the local tensile stress, whereas macroscopic compressive stress decreases the local tensile stress. In this case, difference of transformation plastic coefficients between under tensile and compressive stress is about 20%.

In comparison, when applied stress is normal to preferential grain growth direction, no significant difference of transformation plastic coefficients between tensile and compressive has been observed with the numerical simulation.
The results strongly suggest that the behaviour of transformation plasticity can be affected by grain morphology of daughter phase. It means that the metallurgical effect (e.g. microsegregations) which results in non-equiaxed grain shape influences the subsequent transformation plasticity.

4.2.3 Effect of band structure

Among the processes of steel production, the concentration of chemical species occurs mainly in the casting process. For example, Mn segregation is formed during casting process and it changes its form during subsequent rolling process. It is known to create a band structure after phase transformation.
Kop *et al*. [80] have experimentally found that the microstructure with banded form of Pearlite phase causes anisotropic dilatation during phase transformation. They have measured the dilatations for two directions and compared between them. They have found that the anisotropic dilatation is strongly affected by the shape and direction of banded structure; the dilatation is approximately two times larger in the direction of perpendicular to the bands than normal to them (Fig. 40 (a)). In contrast, the other microstructure, which has less clear banded structure, shows less anisotropic dilatation.
In order to confirm this phenomenon by FFT-based numerical scheme, pearlite band structure, which forms an infinite number of layers of pearlite and ferrite phases, is modelled as follows.
During ferrite and pearlite phase transformation, at first, ferrite phase starts to be produced and then, pearlite transformation starts. Because ferrite phase cannot contain as much carbon as austenite, carbon is brought out from ferrite phase and austenite absorbs it. The austenite phase with much carbon contents transforms into pearlite phase, which shows very higher strength than ferrite phase. In order to simulate this phenomenon, a dual phase transformation procedure is modelled. In this procedure, the ferrite phase transformation start at first, followed by pearlite transformation, and at the end ferrite and pearlite dual phase is obtained. It should be noted that the geometrical importance of banded structure should also be considered. The banded structure is often formed by the microsegregations, which is initially formed during casting and elongated by subsequent rolling.

For the modelling, a band-shaped pearlite phase with two different layer thicknesses are

adopted in the computations. These structures are depicted in Fig. 41. It is obvious that the pearlite phase transformation starts later than ferrite one. Another parameter considered here is the delay time of pearlite transformation. Three delay times are employed in this paper; 0, 4 and 8sec after ferrite transformation start.

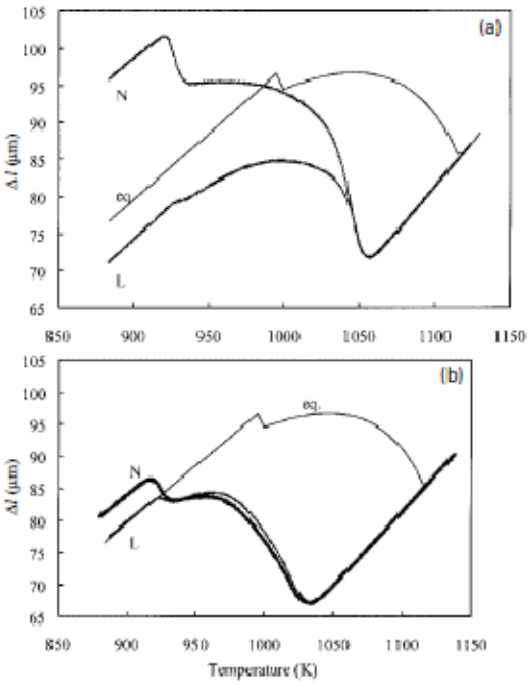

a 1123 K; *b* 1323 K

5 Dilatation curves measured on normal N and longitudinal L specimens austenitised at given temperatures: calculated dilatation curve based on equilibrium transformation and isotropic dilatation behaviour is also shown

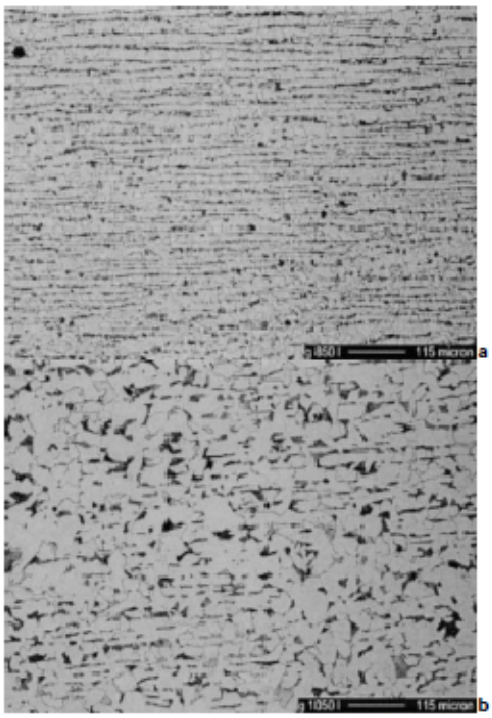

a 1123 K; *b* 1323 K

6 Microstructures showing ferritic–pearlitic band structure after austenitisation at given temperatures and subsequent cooling

Fig. 40 Dilatation curves and banded microstructure. [80]

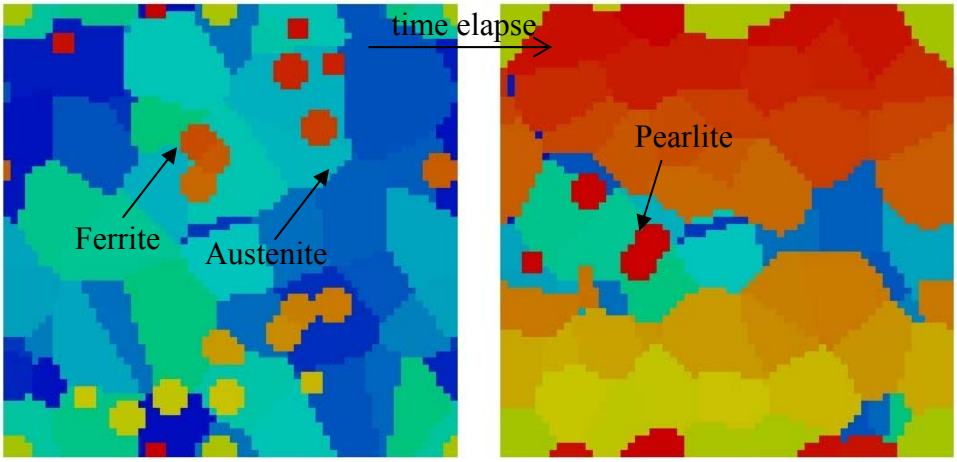

(a) Case1: thin layer

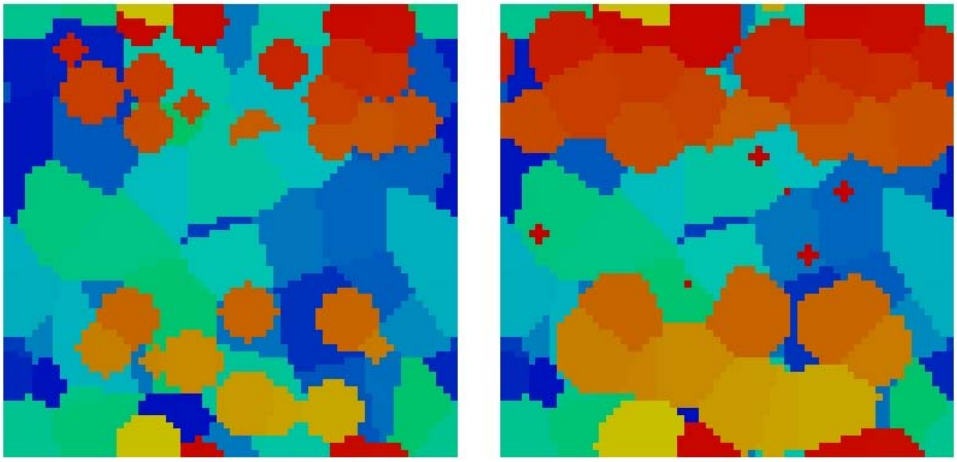

(b) Case2: thick layer

Fig. 41 Pearlite banded structure with two different band widths.

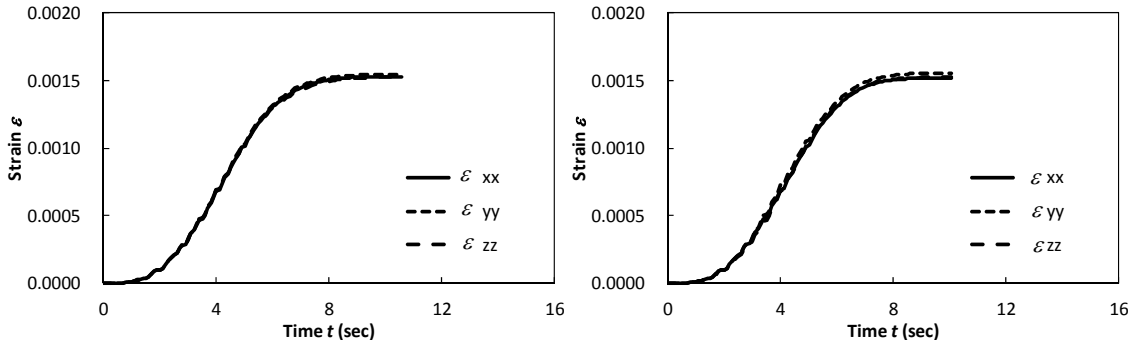

(a) thin layer (pearlite start at 0sec) (b) thick layer (pearlite start at 0sec)

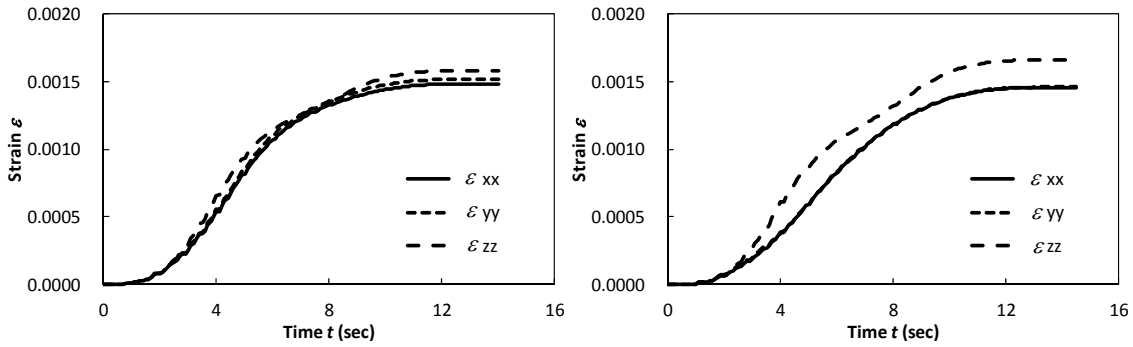

(c) thin layer (pearlite start at 4sec) (d) thick layer (pearlite start at 4sec)

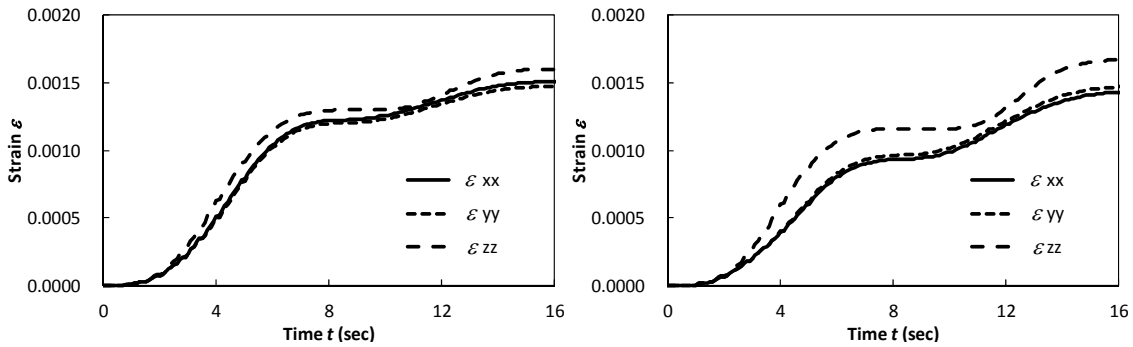

(e) thin layer (pearlite start at 8sec) (f) thick layer (pearlite start at 8sec)

Fig. 42 Strain evolution during ferrite-pearlite dual phase transformation.

The strain evolutions of these cases are shown in Fig. 42. It is clear that the strains in *z*-direction (perpendicular to the band) are larger than those of other directions (figures (c), (d), (e) and (f)). Obviously, the banded structure causes the difference since the larger the layer thickness, the larger the difference in strain (figures (c) and (d)). On the other hand, when the pearlite phase transformation starts at the same time with ferrite transformation, there is no significant anisotropic effect even though the pearlite phase is much harder than that of ferrite.

With these results, it can be concluded that both transformation start order and pearlite band thickness are important parameters influencing the anisotropic dilatation. However the anisotropic effect reported in [80] is much larger than the one obtains with our calculations.

4.2.4 Grain size effect

The calculation results throughout this thesis cannot reflect the grain size effect even though the cases with both plenty grains and few grains are performed. In fact, the hardening law such as equation (141) is independent of grain size.

In contrast, it is well known that the hardness increases along with decreasing mean grain size. Historically, this fact is claimed by Hall (1951) [81] and Petch (1953) [82]. The mechanism is often explained by grain boundaries preventing the penetration of dislocations into neighbouring grains. Thus, the smaller grain size the shorter distance dislocation can travel and consequently, the material gets harder than larger grain size.

The dislocation can be divided into Statistically Stored Dislocation (SSD) and Geometrically Necessary Dislocation (GND) [54]. The SSD represents dislocations from Frank-Read source. The SSD describe well the dislocation dynamics. On the other hand, GND compensates geometrical incompatibility between neighbouring regions [83]. In order to incorporate the grain size effect on FFT-based numerical scheme, GND is taken into account.

4.2.4.1 Hardening model by dislocation density

Dislocation density and material's hardness can be related by following extended Bailey-Hirsch equation [84].

$$g^{\alpha} = \tau_0 + a\mu\tilde{b}\sqrt{\sum_{\beta} d^{\alpha\beta}\rho^{\beta}} \ , \tag{147}$$

where a, μ, $\tilde{b}$ are dimensionless parameter, Young's modulus and Burgers vector respectively. If we define the total dislocation density to be a summation of statistically stored dislocation (SSD) and geometrically necessary dislocation (GND) [53], the total dislocation density can be written as:

$$\rho^{\alpha} = \rho_S^{\alpha} + \|\rho_G^{\alpha}\| \ , \tag{148}$$

where SSD is:

$$\dot{\rho}_S^{\alpha} = \frac{1}{\tilde{b}}\left(\frac{1}{L^{\alpha}} - 2y_c\rho^{\alpha}\right)|\dot{\gamma}^{\alpha}| \ , \tag{149}$$

and GND is[84]:

$$\dot{\rho}_G^{\alpha} = \dot{\rho}_{G,\text{edge}}^{\alpha} + \dot{\rho}_{G,\text{skrew}}^{\alpha} = -\frac{1}{\tilde{b}} s_i^{\alpha} \dot{\gamma}_{,i}^{\alpha} + \frac{1}{\tilde{b}} e_{ijk} s_j^{\alpha} m_k^{\alpha} \dot{\gamma}_{,i}^{\alpha} \,. \tag{150}$$

y_c is mean distance of annihilation of dislocation and L^{α} is a mean free path whose evolution is determined by a power law:

$$\frac{L^{\alpha}}{L_0^{\alpha}} = \left(\frac{\rho^{\alpha}}{\rho_0^{\alpha}}\right)^{-n} , \tag{151}$$

where L_0^{α} ρ_0^{α} are initial free path distance and dislocation density. The rate form of equation (147) can be obtained as:

$$\dot{g}^{\alpha} = \sum_{\beta} \frac{d^{\alpha\beta} a \mu \tilde{b}}{2\sqrt{\rho^{\beta}}} \left(\frac{1}{L^{\beta}} - 2 y_c \rho^{\beta}\right) \left|\dot{\gamma}^{\beta}\right| \,. \tag{152}$$

In this case, the hardening parameter takes following form.

$$h^{\alpha\beta} = \frac{d^{\alpha\beta} a \mu \tilde{b}}{2\sqrt{\rho^{\beta}}} \left(\frac{1}{L^{\beta}} - 2 y_c \rho^{\beta}\right) \,. \tag{153}$$

By these formulations, dislocation density is explicitly connected with mechanical hardening and crystal plasticity regime.

Note that the slip rate derivative can be directly calculated using the slip rate in the Fourier space:

$$\dot{\gamma}_{,i}^{\alpha} = FFT^{-1}(\mathrm{i}\xi_i \hat{\dot{\gamma}}^{\alpha}) \,. \tag{154}$$

This is yet another advantage of the FFT numerical scheme over FEM in terms of efficiency and simplicity.

4.2.4.2 Effect of grain size on stress/strain curve

According to Hall (1951) [81] and Petch (1953) [82], the relation between square root of grain diameter and yield stress is inverse proportional (sometimes, depending on the material, the p number of p-times root changes). Here, uniaxial tensile test simulations are carried out to determine the relation between grain size and hardness. The material parameters which are adopted in the calculations are shown in Table 17. The parameters are set to be the same values for austenite and ferrite phase without initial τ_0 which is already defined in Table 15.

Table 17 Material parameters for both parent and daughter phases.

a	$\tilde{b}$ (m)	L_0 (m)	ρ_0 (m^{-2})	y_c (m)	n
0.2	2.56×10^{-10}	1.0×10^{-3}	1.0×10^{-10}	4.0×10^{-10}	0.72

In Fig. 43, (a) 0.2% strength and (b) 1.0% strength are plotted with several inverse square root of grain diameters.

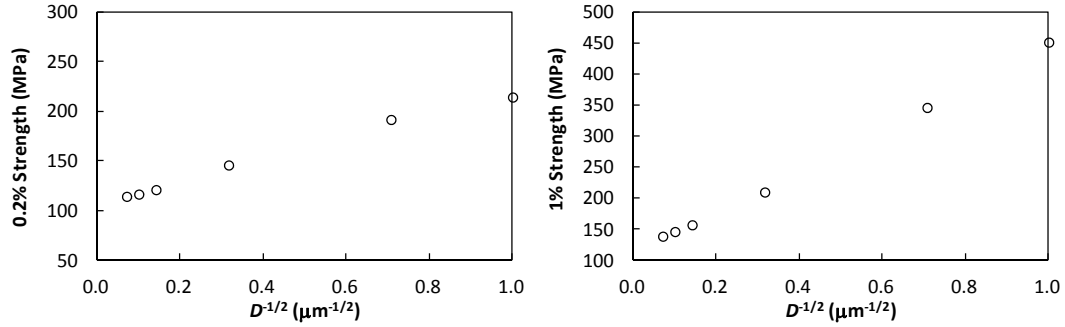

(a) 0.2% strength (b) 1.0% strength

Fig. 43 Relation between flow stress and grain size (100 gains in 64^3 voxels).

An increase of the yield stress is described when the grain size decreases by our FFT computation. Moreover, the relation between inverse square root of grain diameter and both 0.2% and 1.0% yield strength is linear.

In the sequel, two grain sizes are selected (10μm and 100μm) and the evolution of dislocation density distribution during tensile procedure will be investigated. During tension, dislocations develop from Frank-Read source (SSD) and annihilate after a free path or trapped into precipitates or grain boundaries. On the other hand, dislocations must be exist where the strain incompatibility exists (GND) such as grain boundaries. The macroscopic stress-strain relations are shown in Fig. 44.

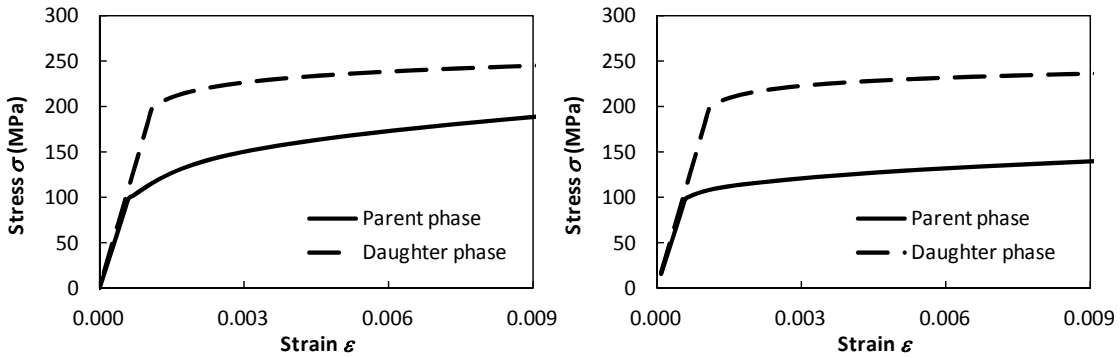

(a) D=10μm (b) D=100μm

Fig. 44 Calculated stress-strain curves (100 gains in 64^3 voxels).

The parameters of the constitutive law are the same. It is observed that the work hardening is much stronger for small grain size because of GND evolution.

The evolutions of SSD, GND and total dislocation density are depicted in Fig. 45 and Fig. 46. These figures show a cross section of whole 3D calculation.

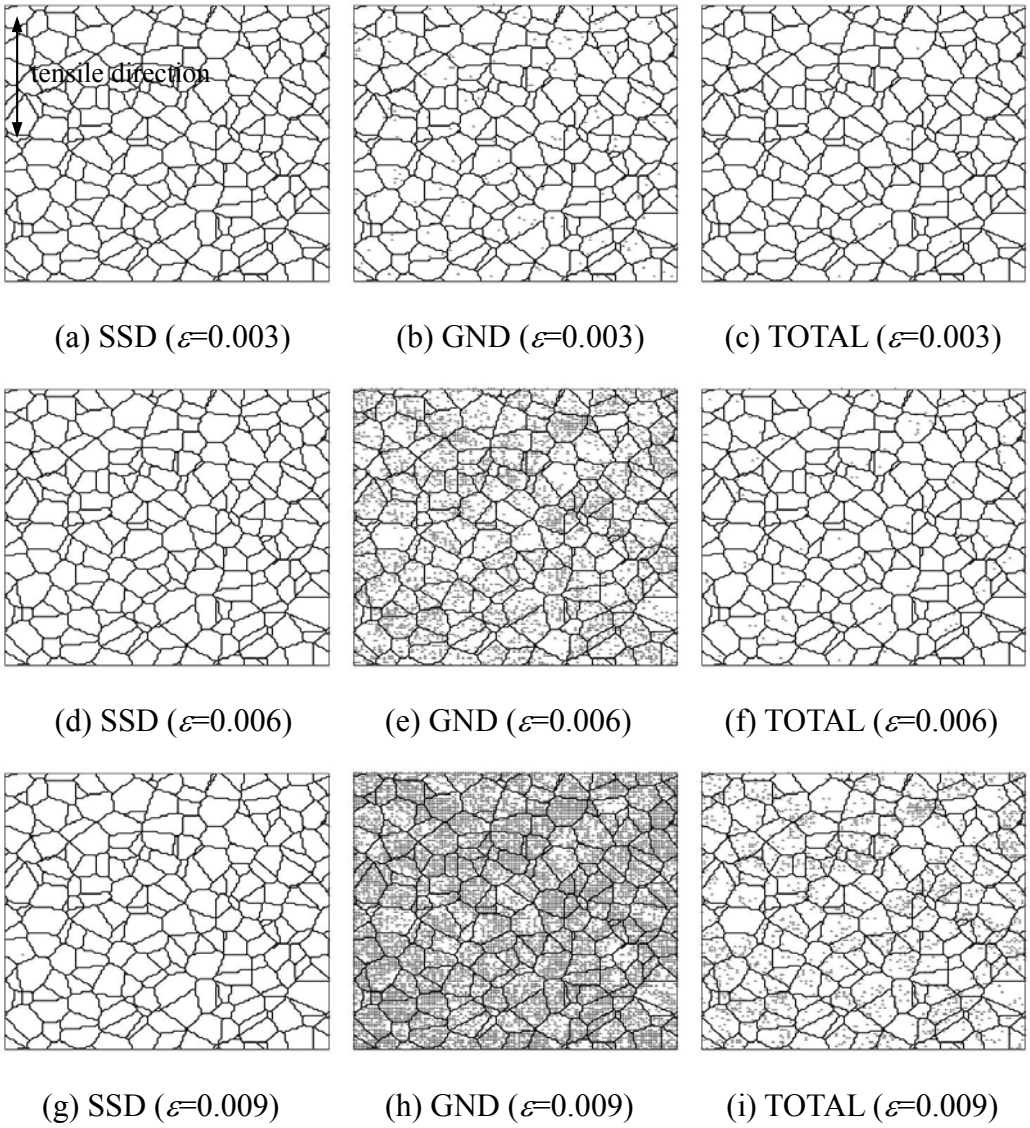

(a) SSD (ε=0.003) (b) GND (ε=0.003) (c) TOTAL (ε=0.003)

(d) SSD (ε=0.006) (e) GND (ε=0.006) (f) TOTAL (ε=0.006)

(g) SSD (ε=0.009) (h) GND (ε=0.009) (i) TOTAL (ε=0.009)

Fig. 45 Dislocation density distribution during tension
(D=10μm, 2000 gains in 128^3 voxels).
$\perp$ represents dislocation density:
$\rho > 5\times10^{13}$ (SSD), $\rho > 5\times10^{13}$ (GND), $\rho > 10^{14}$ (TOTAL)

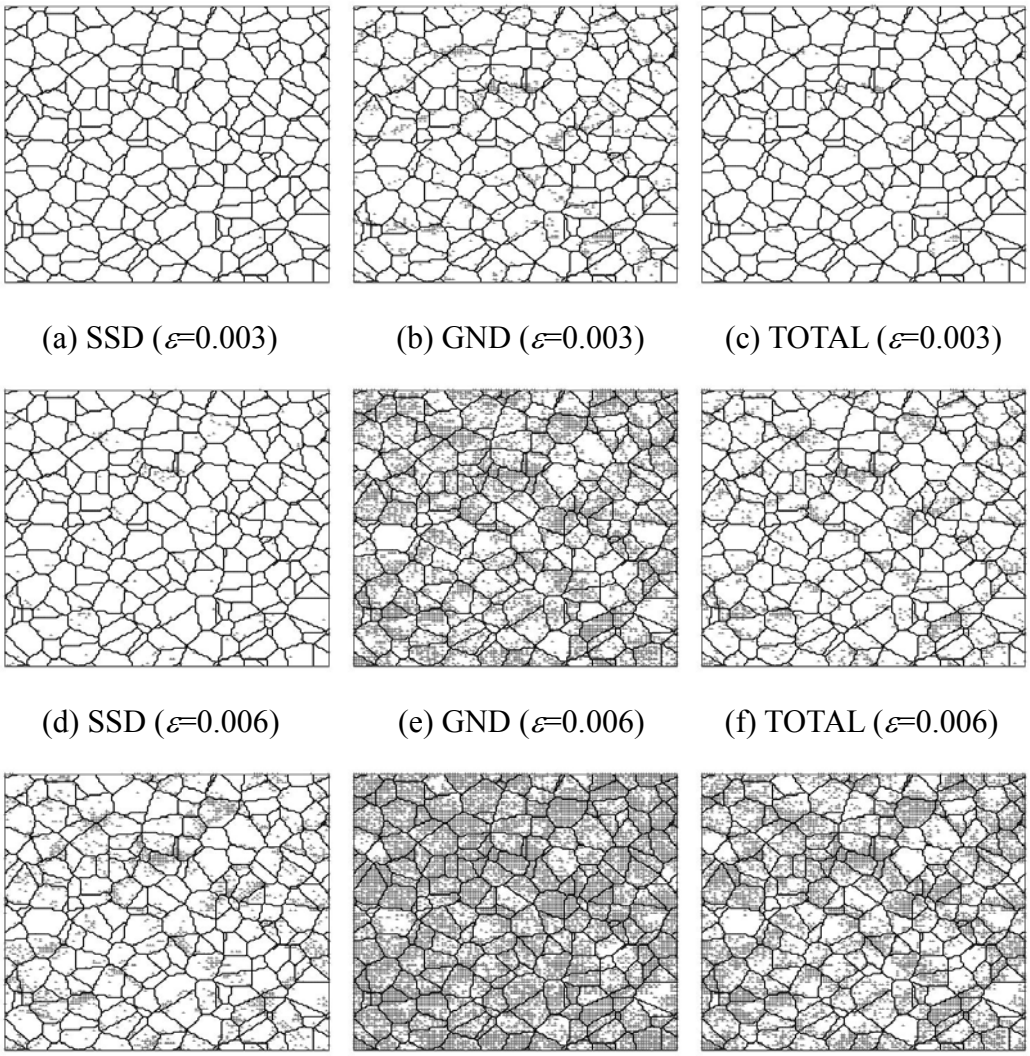

(a) SSD (ε=0.003) (b) GND (ε=0.003) (c) TOTAL (ε=0.003)

(d) SSD (ε=0.006) (e) GND (ε=0.006) (f) TOTAL (ε=0.006)

(g) SSD (ε=0.009) (h) GND (ε=0.009) (i) TOTAL (ε=0.009)

Fig. 46 Dislocation density distribution during tension
(D=100μm, 2000 gains in 128^3 nodes).
$\perp$ represents dislocation density:
$\rho>5\times10^{12}$ (SSD), $\rho>5\times10^{12}$ (GND), $\rho>10^{13}$ (TOTAL)

For 10μm case (Fig. 45), GND density is much more important than SSD density. GND starts to accumulate mainly along with the grain boundaries (there exist the dislocations inside the grains but it may be caused by 2D cross section image out of 3D and thus the grain boundaries for normal to the sheet direction are not presented).

For 100μm case (Fig. 46), similar to 10μm case, GND is higher than SSD. But in this case, comparing to 10μm, SSD is rather dense. This is because GND develops near grain boundaries and hence it is stronger in smaller grains. SSD and GND densities show a

pattern with bands at $\pm 45^{\circ}$.

4.2.4.3 Effect of grain size on transformation plasticity

Following above discussion, the grain diameters of 10μm and 100μm are selected to investigate the grain size effect on transformation plasticity. The parameter set of Table 17 is again used. The phase transformation is studied under constant applied stresses (from -90MPa to 90MPa). Fig. 47 shows cross sections during phase transformation of average grain diameter of 10μm (black colour is parent and red represents daughter phase) under stress free condition. Starting with 2000 grains germination, they grow isotropically.

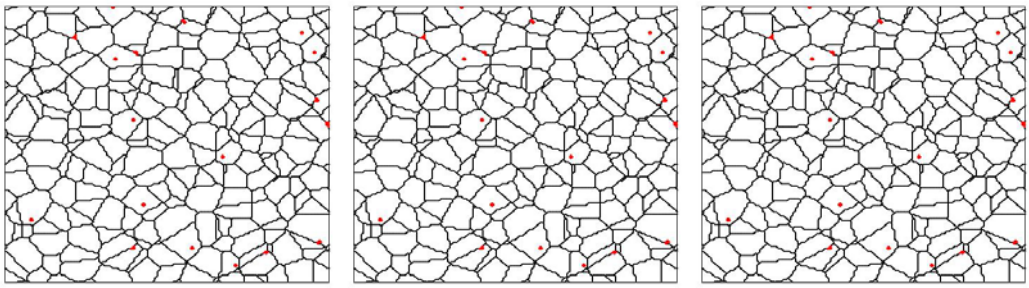

(a) SSD (ξ=0.0) (b) GND (ξ=0.0) (c) TOTAL (ξ=0.0)

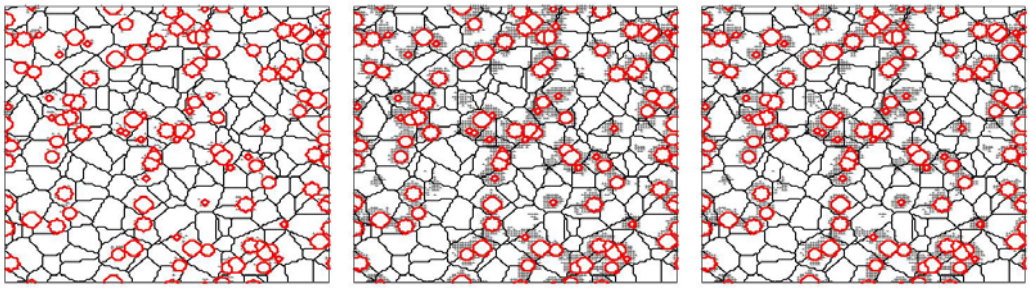

(d) SSD (ξ=0.1) (e) GND (ξ=0.1) (f) TOTAL (ξ=0.1)

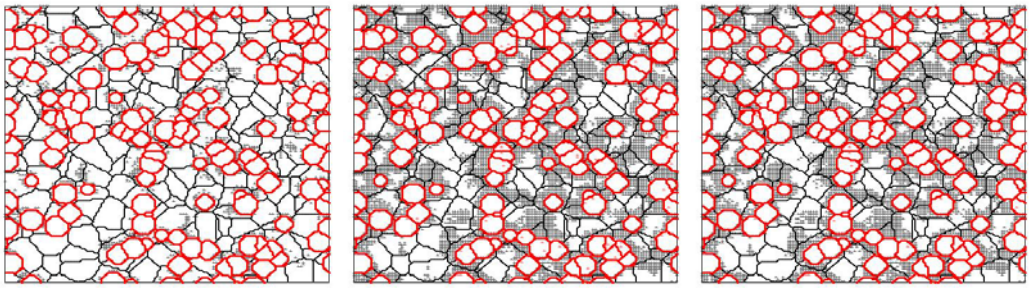

(g) SSD (ξ=0.3) (h) GND (ξ=0.3) (i) TOTAL (ξ=0.3)

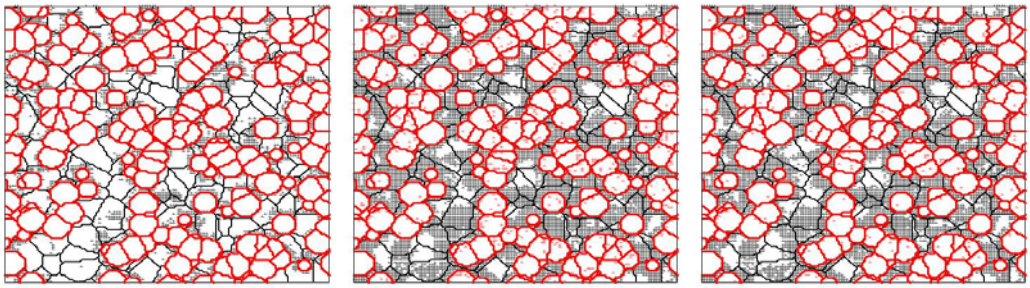

(j) SSD (ξ=0.5) (k) GND (ξ=0.5) (l) TOTAL (ξ=0.5)

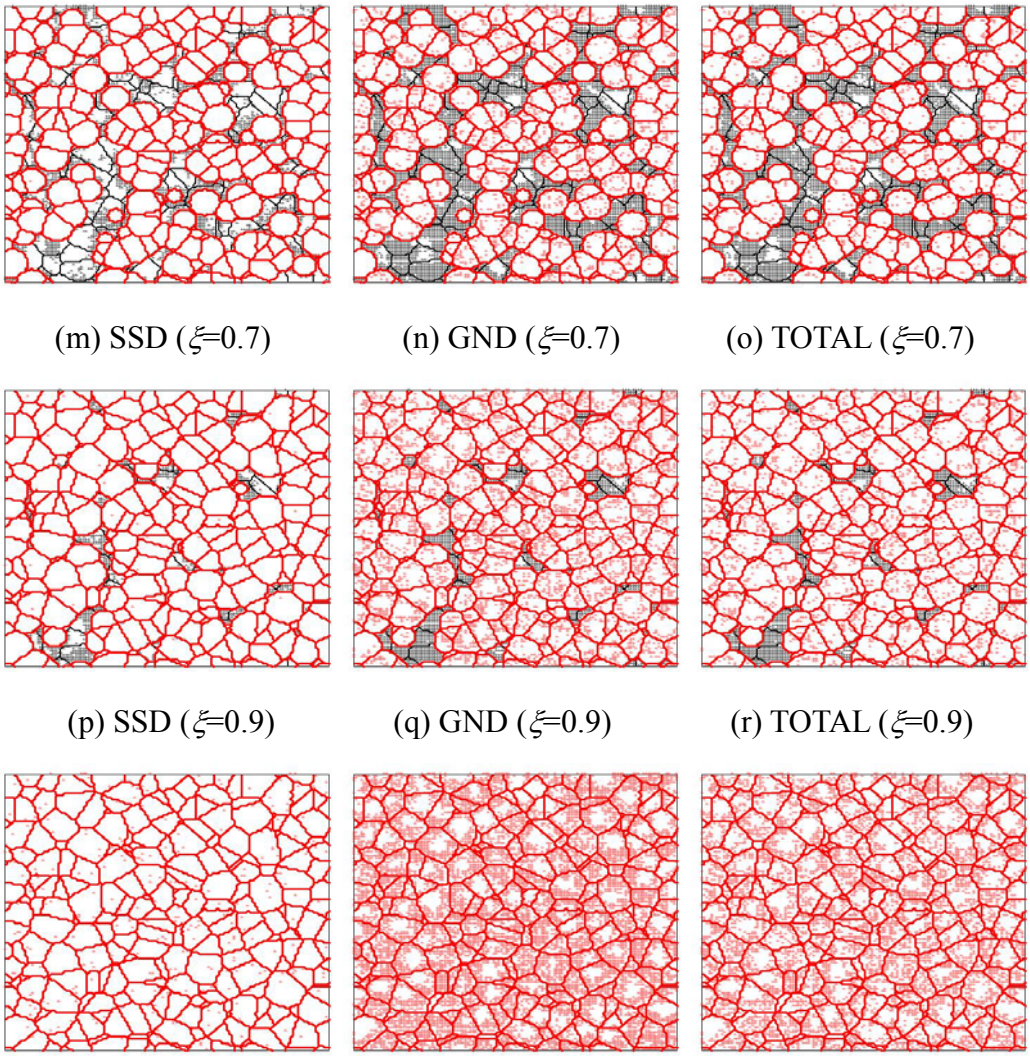

(m) SSD (ξ=0.7) (n) GND (ξ=0.7) (o) TOTAL (ξ=0.7)

(p) SSD (ξ=0.9) (q) GND (ξ=0.9) (r) TOTAL (ξ=0.9)

(s) SSD (ξ=1.0) (t) GND (ξ=1.0) (u) TOTAL (ξ=1.0)

Fig. 47 Dislocation density distribution during phase transformation (D=10μm, 2000 gains in 128^3 nodes, black colour : parent phase, red colour : daughter phase).
⊥ parent phase: $\rho>10^{11}$ (SSD), $\rho>10^{11}$ (GND) , $\rho>2\times10^{11}$ (TOTAL)
⊥ daughter phase: $\rho>10^{12}$ (SSD), $\rho>10^{12}$ (GND) , $\rho>2\times10^{12}$ (TOTAL)

In this case, GND is much greater than SSD in parent phase. It is clear that GND in the parent phase develops around the daughter grains. It means that the transformation strain causes strong incompatibility between the two phases, and consequently, GND in parent phase accumulates at the vicinity of the daughter grain spheres. Furthermore, when two or more daughter grains approach each other, parent grains in between these daughter grains have considerable high dislocation density.

GND density in daughter phase is also more important than SSD density. Similar to GND in parent phase, it is strong near their grains' surface.

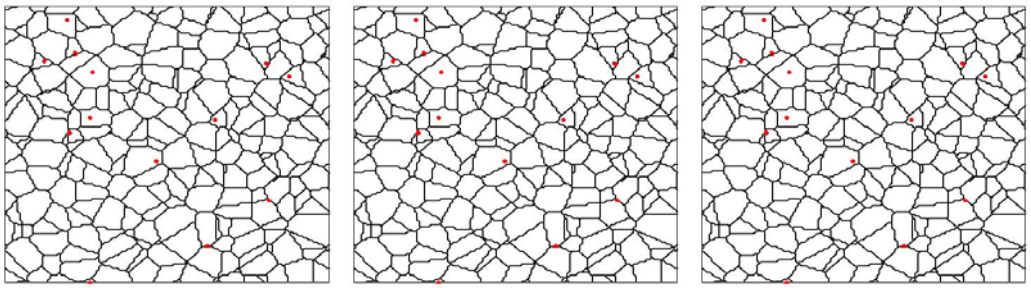

(a) SSD (ξ=0.0) (b) GND (ξ=0.0) (c) TOTAL (ξ=0.0)

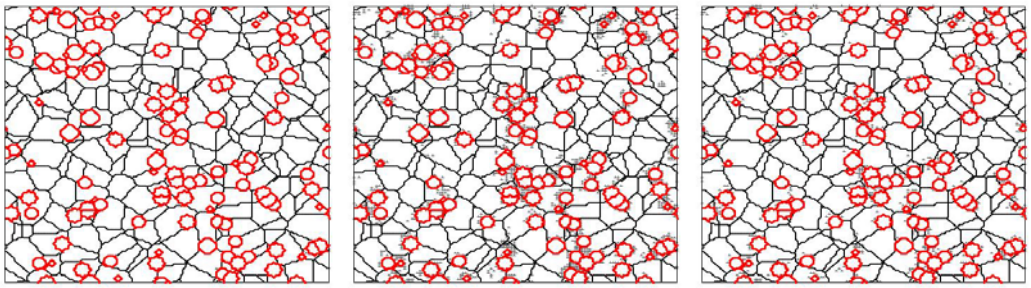

(d) SSD (ξ=0.1) (e) GND (ξ=0.1) (f) TOTAL (ξ=0.1)

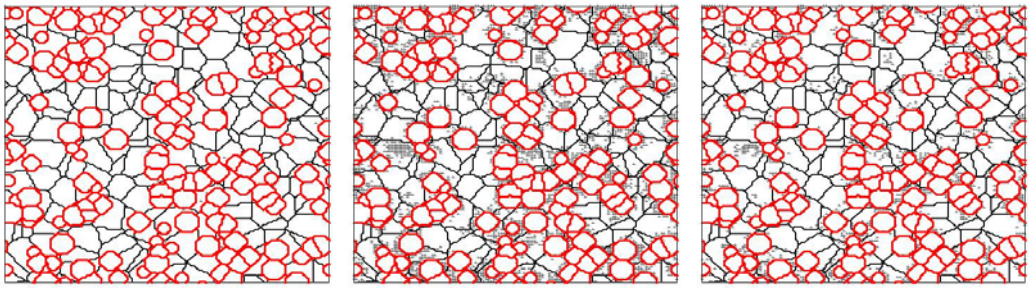

(g) SSD (ξ=0.3) (h) GND (ξ=0.3) (i) TOTAL (ξ=0.3)

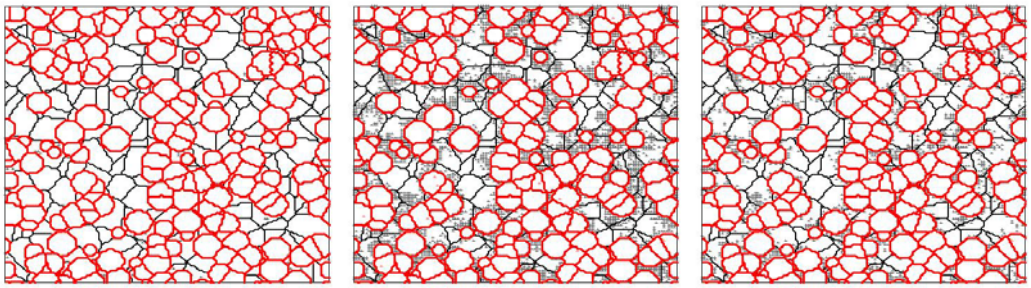

(j) SSD (ξ=0.5) (k) GND (ξ=0.5) (l) TOTAL (ξ=0.5)

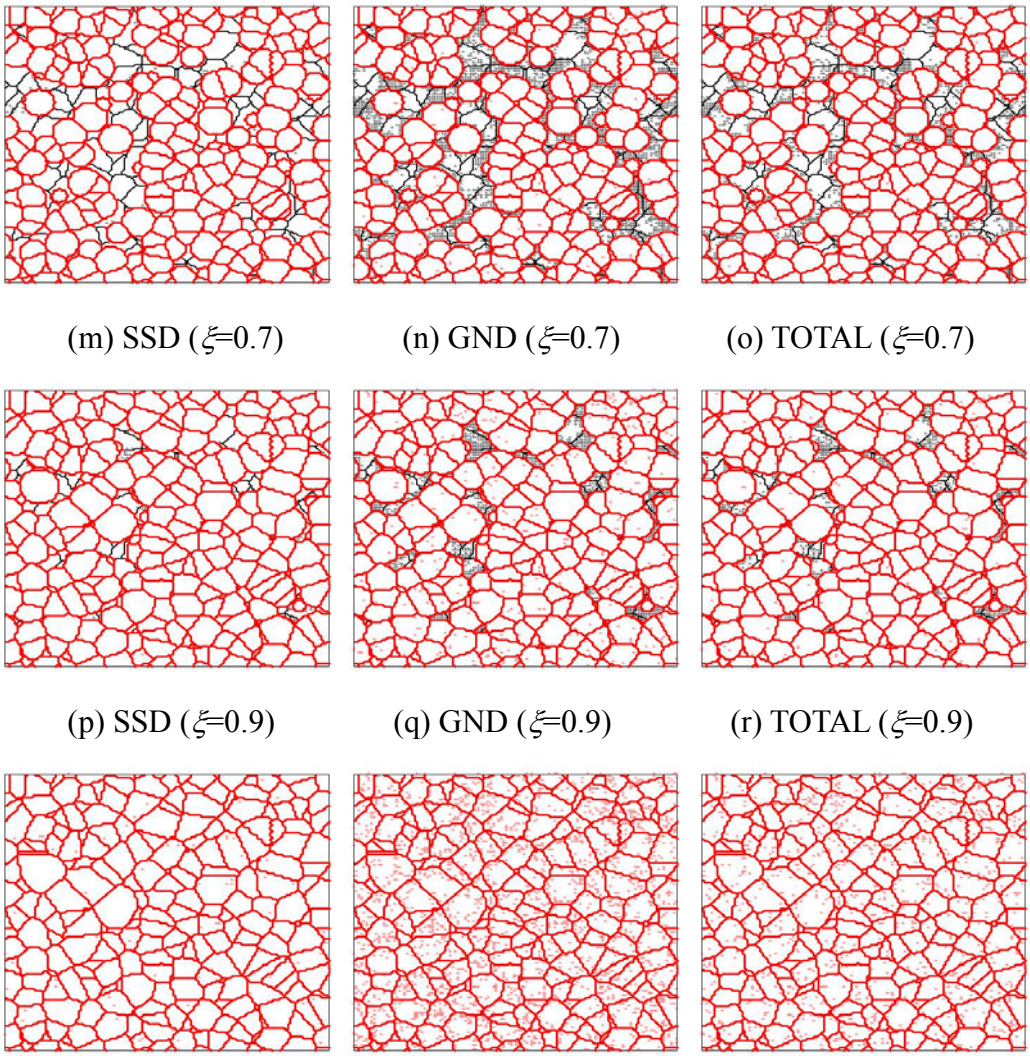

(m) SSD (ξ=0.7) (n) GND (ξ=0.7) (o) TOTAL (ξ=0.7)

(p) SSD (ξ=0.9) (q) GND (ξ=0.9) (r) TOTAL (ξ=0.9)

(s) SSD (ξ=1.0) (t) GND (ξ=1.0) (u) TOTAL (ξ=1.0)

Fig. 48 Dislocation density distribution during phase transformation (D=100μm, 2000 gains in 128^3 nodes, black colour : parent phase, red colour : daughter phase).

⊥ parent phase : $\rho>10^{11}$ (SSD), $\rho>10^{11}$ (GND) , $\rho>2\times10^{11}$ (TOTAL)

⊥ daughter phase : $\rho>10^{12}$ (SSD), $\rho>10^{12}$ (GND) , $\rho>2\times10^{12}$ (TOTAL)

Fig. 48 shows dislocation densities for average grain diameter of 100μm case under stress free condition. Similar to 10μm grain size case, GND is more dense than SSD in both parent and daughter phase. Comparing to 10μm grain size case, both SSD and GND densities are less important, while the difference in SSD between both grain sizes is much less important than that in GND. This is because the grain size effect is much more important on GND density than SSD density, for GND dislocations accumulate at

the vicinity of grain boundaries and the smaller grain size, the more grain boundaries the material contains.

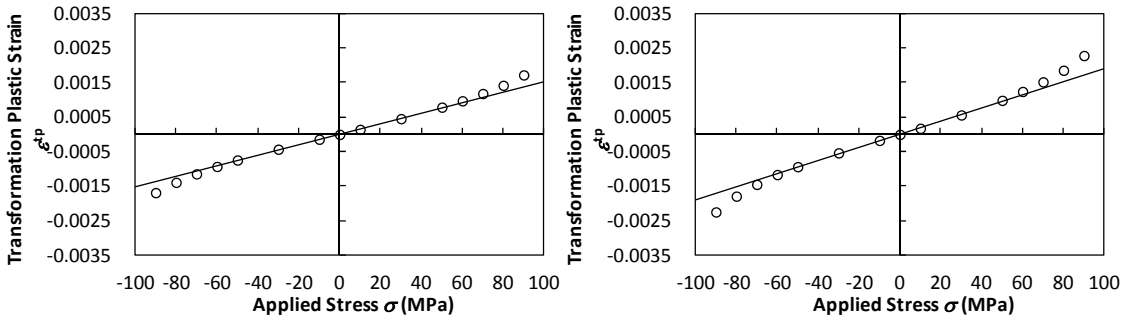

(a) D=10μm (b) D=100μm

Fig. 49 Transformation plasticity results.

Fig. 49 reports the comparison of transformation plasticity between 10μm and 100μm average grain diameters. The slopes of applied stress and transformation plastic strain curve is calculated as $K_P = 1.51 \times 10^{-5}$ (MPa^{-1}) for 10μm diameter and $K_P = 1.89 \times 10^{-5}$ (MPa^{-1}) for 100μm. This dependence can be easily predicted by the notion that the transformation plastic strain is inverse proportional of yield stress of parent phase.

4.2.5 Kinematic hardening

Back stress effects on transformation plasticity are reported. Taleb *et al*.[39] revealed that the pre-hardening affects significantly on the subsequent transformation plastic strains. They have observed transformation plastic strain even under stress free condition, if the material is preliminarily deformed. Even more, the reverse transformation plastic strains (compressive TP strain under tensile stress, or tensile TP strain under compressive stress) have been observed.

Nagayama *et al*. [85] also confirmed the pre-hardening effect by their experiments. They claimed that the effect differs with the modes of applied stress, i.e. tension, compression and shear.

These effects have been observed with experimental approach and all those effects have been manifested under bainitic or martensitic phase transformation. To the author's knowledge, pre-hardening effect (or back stress effect) on ferritic or pearlitic phase transformation remains an open question. Thus, back stress effect during diffusive phase transformation, i.e. Greenwood-Johnson effect, is investigated in the sequel.

4.2.5.1 Back stress model for crystal plasticity

Previous discussions considered only isotropic hardening models. The yield surface centre remains at its original position. In this section, we introduce following effective resolved shear stress $\tau^{*(\alpha)}$.

$$\tau^{*(\alpha)} = \tau^{(\alpha)} - a^{(\alpha)}, \tag{155}$$

where $\tau^{*(\alpha)}$ is the effective resolved shear stress and $a^{(\alpha)}$ is the back stress on the α slip system. Now let the evolution of $a^{(\alpha)}$ be described by Armstrong-Frederick type model [86], such that:

$$\dot{a}^{(\alpha)} = C\dot{\gamma}^{(\alpha)} - da^{(\alpha)}\left|\dot{\gamma}^{(\alpha)}\right| \tag{156}$$

where C and d are material constants.

The compression calculation until -0.2% strain following 0.3% tension is operated with several set of material constants; $(C, d) = (0, 0), (840, 120), (1400, 200)$. The calculated results are depicted in Fig. 50. Note that pre-deformation is always carried out in *z*-direction.

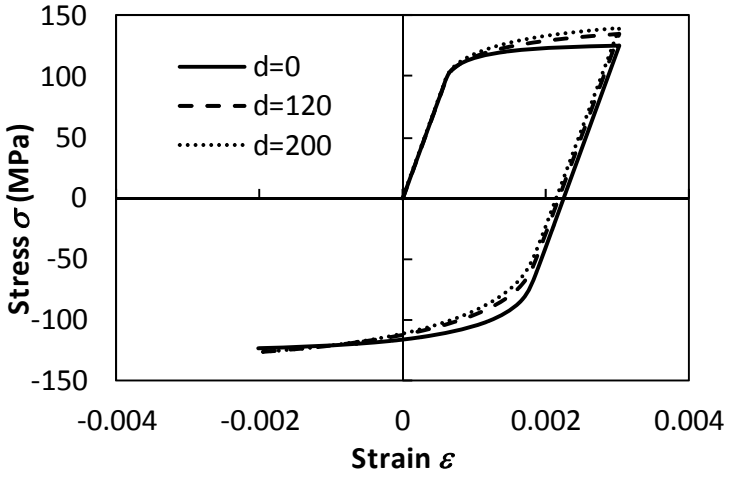

Fig. 50 Calculated stress/strain curve during cyclic deformation.

As increasing d value, work hardening effect as well as back stress effect becomes significant. The difference between the cases $(C, d) = (840, 120)$ and $(C, d) = (1400, 200)$ is enough small so that the difference may not affect the transformation plasticity.

Finally, the material constants are chosen $(C, d) = (840, 120)$ for the following transformation plasticity calculations. Since the results depend on the value of these coefficients, the following discussion will provide only qualitative trends.

4.2.5.2 Back stress effect on transformation plasticity

For the purpose of examining the back stress effect on transformation plasticity, computations of pre-hardening along z-direction (up to 10% strain for tensile case and -10% for compressive case) followed by phase transformation under several applied stresses are carried out in a 64^3 voxels unit-cell with 100 grains. The schematic illustration of this sequence is depicted in Fig. 51. Results obtained for a free dilatation condition are reported in Fig. 52.

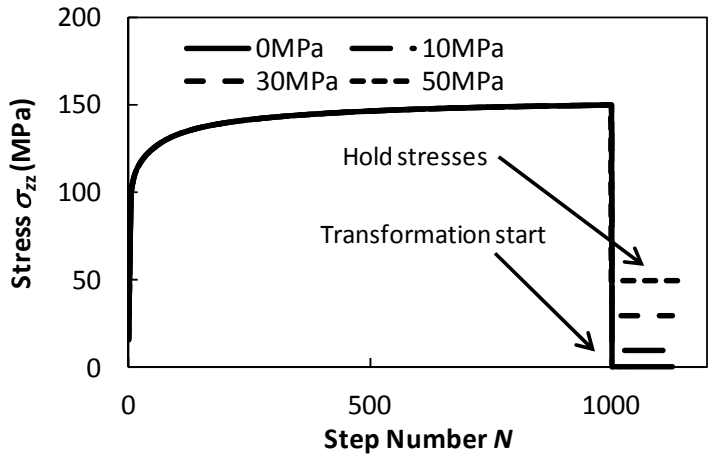

Fig. 51 Schematic illustration of calculation sequence.

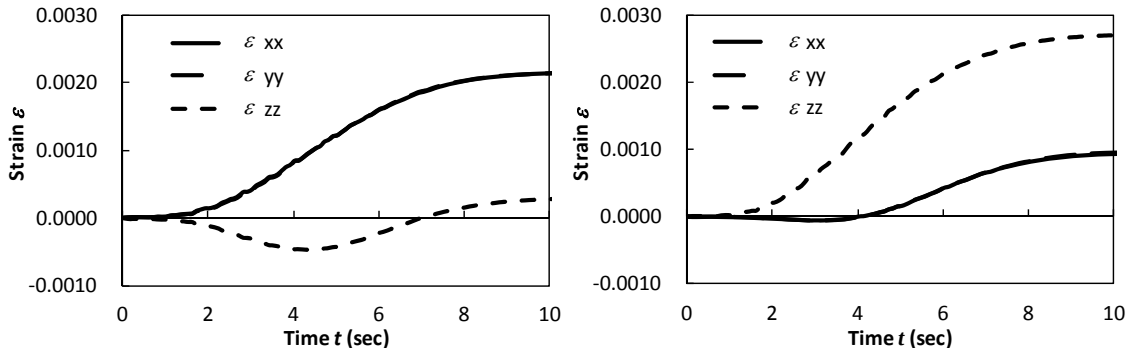

(a) pre-tension (b) pre-compression

Fig. 52 Transformation strain for pre-tensioned material.

They strongly differ from the isotropic case (Fig. 19). The pre-hardened sample (Fig. 52 (a)) shows minimum value of transformation strain in the *z*-direction and the strain along the other directions *x* and *y* have the same value. The overall response is thus

transversely isotropic. It is worth mentioning that it has been checked that the overall volume change is not affected, as expected. That is $\mathrm{tr}(\bar{\varepsilon}^m) = 3\beta$ with β the dilatation coefficient. This means that the anisotropic strain during phase transformation is caused by plastic deformation. The explanation of this phenomenon can be given as follows.

During pre-hardening process, the centre of yield surface moves toward the loading direction, and thus material gets hardened in the loading direction. During subsequent phase transformation, plastic strain mainly occurs in parent phase in order to accommodate the volume difference between parent and daughter phases. If the material is totally isotropic, this plastic strain is cancelled at the overall scale [79]. Though, if the material is anisotropic, the plastic strain is not cancelled. In the present case, due to the hardness in *z*-direction, parent phase preferably deform along *x* and *y* directions during phase transformation and it causes macroscopic anisotropic deformation and even negative strain for *z*-direction. It can be remarked that negative plastic strain occurs along *z*-direction at the beginning. During phase transformation, it is counterbalanced by volume expansion.

The above explanation is also valid for the pre-compressed case (Fig. 52 (b)). To confirm this, -10% pre-compressed followed by phase transformation calculations are carried out. It is clear that the *z*-direction is compressed in advance and which eased the tensile plastic deformation because the transformation strain is positive. In this case, only *z*-direction strain accelerates during phase transformation and other strain components are smaller.

Experimental evidence with bainitic phase transformation can be found in the work by Taleb *et al*. [39]. They have performed pre-hardening tests followed by transformation plasticity. They observed similar results to those shown in this thesis (see Fig. 53).

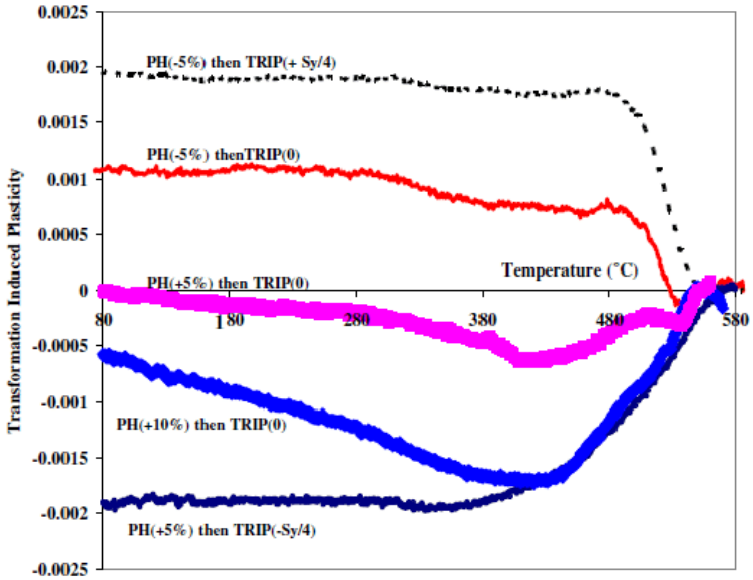

Fig. 7. Transformation induced plasticity $E^{tp}(T)$ in the pre-hardening tests.

Fig. 53 Pre-hardening effect on transformation plasticity for bainitic phase transformation. (Experimental results taken from [39])

For example, 5% tensile pre-deformation followed by phase transformation under free applied stress shows negative transformation strain at the beginning, which is similar to Fig. 52.

Calculated pre-tension results with applied stresses (compression and tension) are reported in Fig. 54.

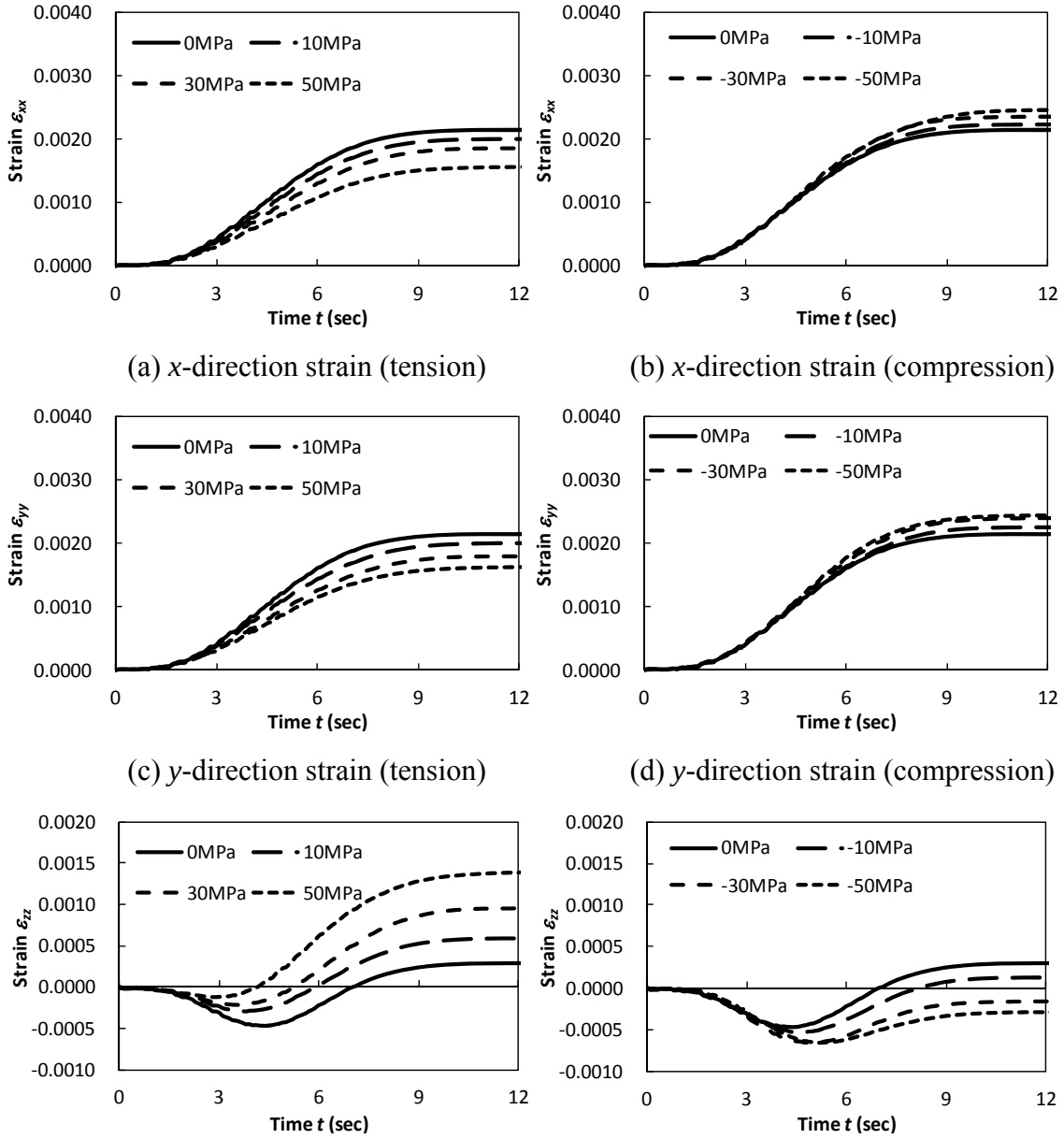

(a) *x*-direction strain (tension) (b) *x*-direction strain (compression)

(c) *y*-direction strain (tension) (d) *y*-direction strain (compression)

(e) *z*-direction strain (tension) (f) *z*-direction strain (compression)

Fig. 54 Transformation plastic strain for pre-tensioned material.

Analogous to the stress free dilatation with pre-tensioning, the negative dilatations for *z*-direction are observed at the beginning of phase transformation. As increase the applied stress, the obtained transformation plastic strain increase as well. It can be also observed that as increase the transformation plastic strain for *z*-direction, the strains for other directions decrease.

On the other hand, for the pre-compression case (Fig. 55), the transformation plastic

strains of compressive pre-deformed case in *x*-direction and in *y*-direction, i.e. ε_{xx} and ε_{yy}, are smaller than those of tensile pre-deformed case. The transformation plastic strains in *z*-direction (ε_{zz}), however, are much larger. These results can also support the notion that the back stress which is introduced during pre-deformation causes the anisotropic transformation plastic strain evolutions. This tendency is found to be similar to the transformation strains evolution under stress free conditions as well as pre-tensioned case.

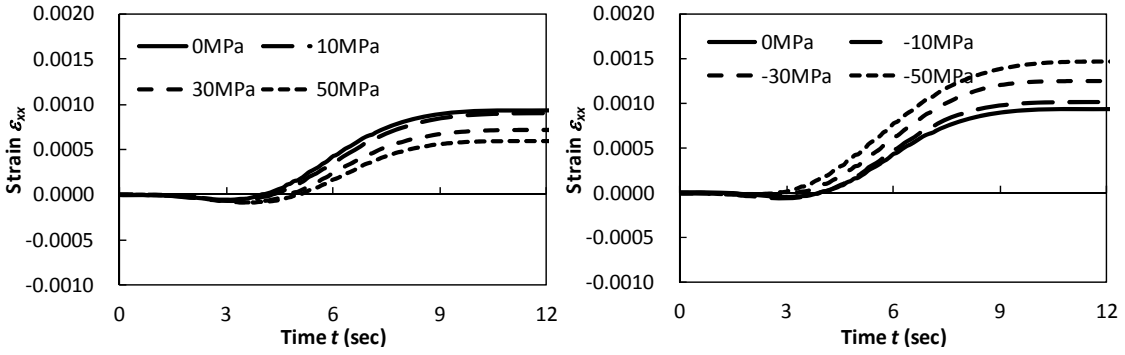

(a) *x*-direction strain (tension)

(b) *x*-direction strain (compression)

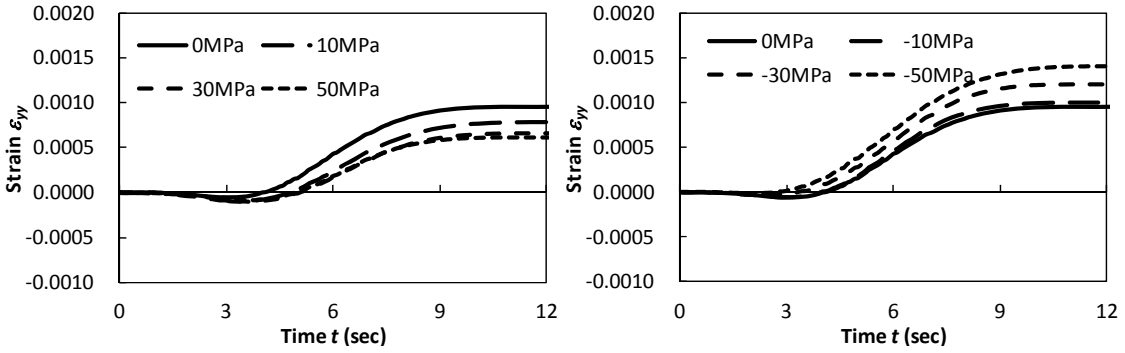

(c) *y*-direction strain (tension)

(d) *y*-direction strain (compression)

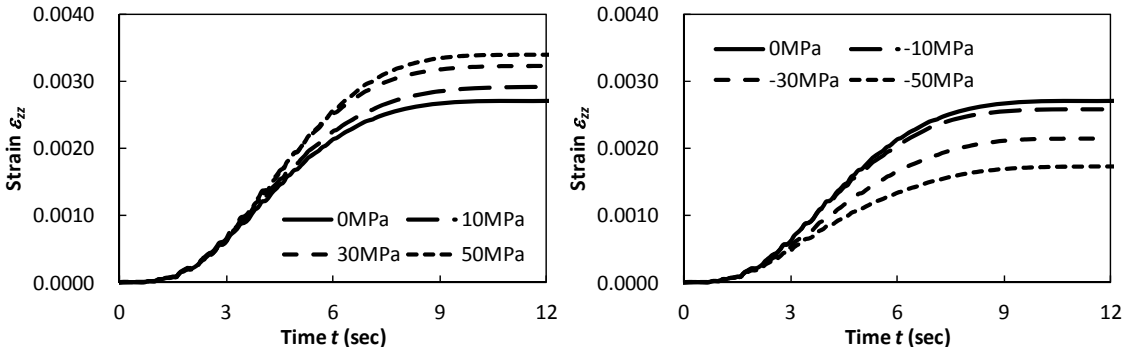

(e) *z*-direction strain (tension)

(f) *z*-direction strain (compression)

Fig. 55 Transformation plastic strain for pre-compressed material.

Transformation plastic strains in *z*-direction versus applied stresses are plotted in Fig. 56. Note that figures (b) and (d) are enlarged views of (a) and (b) with respect to the applied stresses.

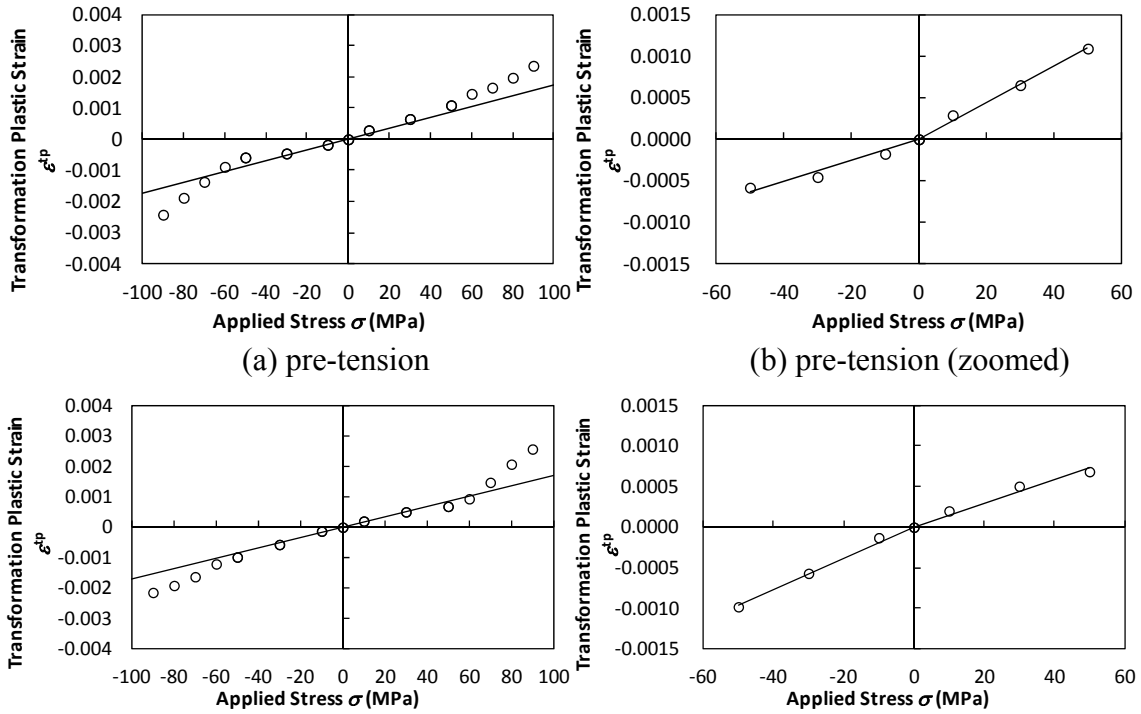

(a) pre-tension (b) pre-tension (zoomed)

(c) pre-compression (d) pre-compression (zoomed)

Fig. 56 Relation between transformation plastic strain and applied stress in *z*-direction.

The quantitative descriptions of these trends are given by following transformation plastic coefficients values.

Pre-tension: $K_P^+ = 2.12 \times 10^{-5}$ (MPa^{-1}), $K_P^- = 1.17 \times 10^{-5}$ (MPa^{-1})

Pre-compression: $K_P^+ = 1.36 \times 10^{-5}$ (MPa^{-1}), $K_P^- = 2.01 \times 10^{-5}$ (MPa^{-1})

For relatively small applied stress case (between -50 and 50MPa applied stress) with pre-tension, the slope for tensile stress K_P^+ is larger than for compressive stress K_P^- (Fig. 56 (b)). Inversely, for the case with pre-compression, the slope for tensile stress K_P^+ is smaller than for tensile stress K_P^- (Fig. 56 (d)).

For large applied stress case, the transformation plastic strains for negative applied stress in pre-tension case accelerate faster than those of positive (Fig. 56 (a)). And one can see the contrary behaviour in pre-compression case (Fig. 56 (c)).

Obviously, these phenomena are linked to the back stress which was introduced by

precedent deformation. For example, the pre-tension hardens the parent phase in z-direction, and it hinders the deformation of parent phase toward z-direction during phase transformation. In contrast, it enhances plastic deformation of daughter phase, which results in large K_P^+ in (Fig. 56 (b)). As it enhances plastic deformation in daughter phase even under small applied stress, we observe less nonlinearity under high applied stress (Fig. 56 (a)). The inverse explanation can be given to (Fig. 56 (c) and (a)).

4.2.5.3 Back stress effect on secant modulus of elasticity

Back stress can affect not only transformation plasticity but also secant modulus of elasticity (pseudo elasticity). Secant modulus of elasticity is important material component especially for the spring back analyses during forging processes of the automobile applications.

It is well known that the secant modulus of elasticity in steel can be decrease after plastic deformation. However, there are not so many data have been given and even more, the mechanism of this phenomenon remains unclear. Thus, the secant moduli of elasticity after several pre-deformation strain values are analysed. Fig. 57 is a representation of secant modulus of elasticity after deformation.

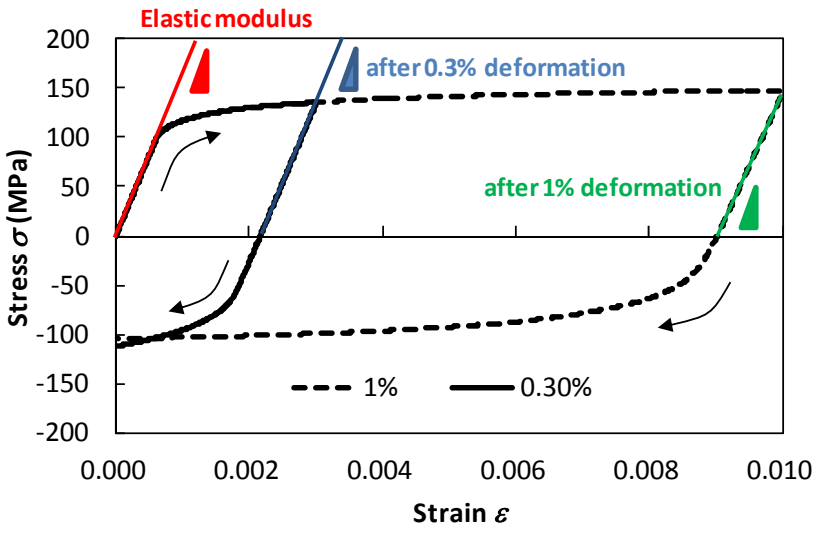

Fig. 57 Schematic illustration of tangent modulus of elasticity after deformation.

The cyclic loading simulations by using back stress model (treated throughout in this section) are carried out. After deformation, with strain values of 0.3, 1.0, 10.0%, the secant moduli of elasticity during unloading process are calculated. The results are plotted in Fig. 58.

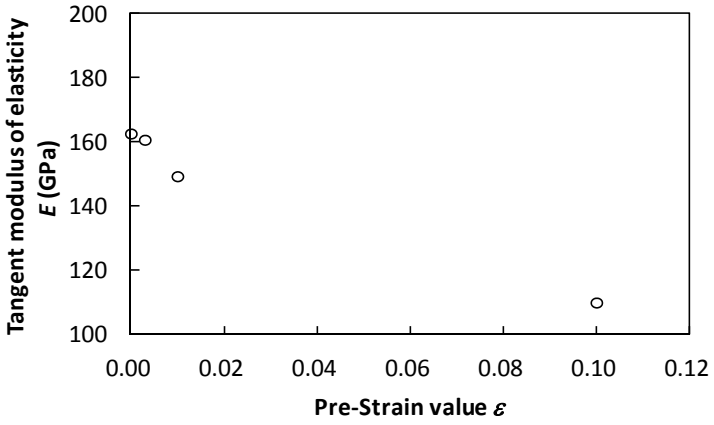

Fig. 58 Relation pre-strain value and tangent modulus of elasticity.

It is shown that the secant modulus of elasticity decreases along with increasing pre-strain value (about 30% decrease by 10% strain). These calculation results agree qualitatively with the experimental results. During unloading process, plastic deformation occurs because of the back stress effect and it results in the difference in nominal secant modulus of elasticity.

It is also interesting to look at the anisotropy of secant modulus of elasticity after the deformation. Thus, 1% uni-axial pre-tension and complete unloading process calculation is followed by uniaxial tensile deformation along other two directions (i.e. *x*-direction and *y*-direction) examining their secant moduli of elasticity.

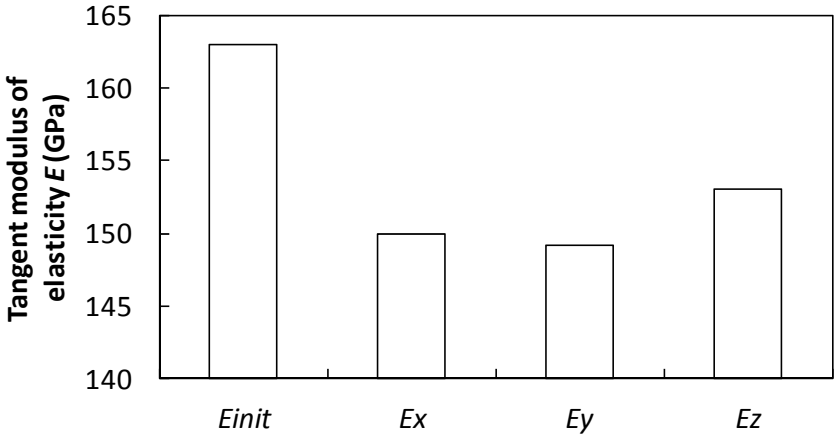

Fig. 59 Anisotropic tangent modulus of elasticity (the values in three directions after unloading).

The results (Fig. 59) show that the secant moduli of elasticity in all three directions are decreased from initial state after the deformation. The pre-tension is loaded in *z*-direction and so the secant modulus of elastic in *x* and *y* directions found to be almost the same value. These values are found to be smaller than the one in *z*-direction. This fact means that after deformation, it is easier to induce plastic deformation scale in *x* and *y* directions than in *z*-direction because *z*-direction was pre-deformed and the yield surface has already moved forward this direction. This is consistent with previous analysis on transformation plasticity.

4.2.6 Effect of cementite phase

Because pearlite is a composite material composed of ferrite and cementite lamellar, the real transformation plasticity can differ from the calculation using average material components. To confirm this fact., the volumetric difference between ferrite and cementite is calculated by Miettinen's model[5]. Transformation volume expansion ratio of cementite and ferrite is shown in Table 18.

Table 18 Calculated transformation volume change of Cementite and Ferrite.

Temp.(C)	ρ_F Ferrite	ρ_C Cementite	ξ_F Ferrite	ξ_C Cementite	ratio β_C/β_F
300	7676	7533	0.74	0.26	1.0063
400	7643	7505	0.74	0.26	1.0061
500	7609	7470	0.74	0.26	1.0061
600	7573	7430	0.74	0.26	1.0064
700	7536	7383	0.74	0.26	1.0069

According to the model, the volumetric difference is not so significant that it cannot significantly affect transformation plasticity.

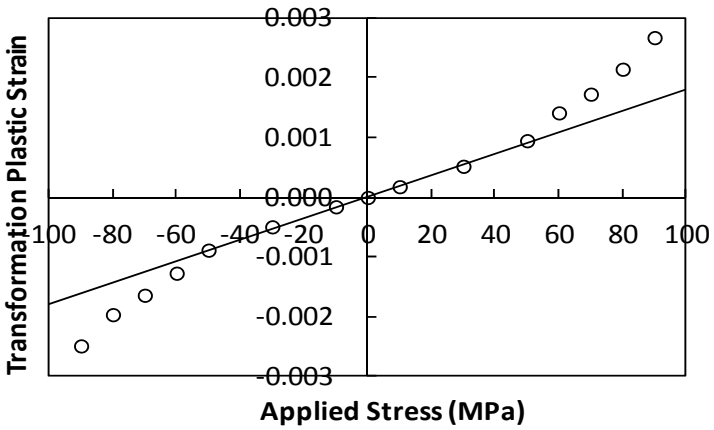

Fig. 60 Calculated results of transformation plasticity with effect of Cementite.

The transformation plastic coefficients can be calculated as follows.

$K_P = 1.79 \times 10^{-5}$ (MPa^{-1})

$K_P^+ = 1.88 \times 10^{-5}$ (MPa^{-1}), $K_P^- = 1.76 \times 10^{-5}$ (MPa^{-1})

They are not so different from those of austenite-ferrite phase transformation which are presented in the above discussion.

4.2.7 Transformation plasticity at high temperature (viscoplasticity)

Up to now, we have considerate rate-independent elastoplastic behaviour. However, the diffusive phase transformations in steels often occur at high temperature during cooling processes comparing to displacive phase transformations. In this case, viscoplastic deformation or creep deformation should be taken into account. Viscoplasticy at the slip systems scale is usually modelled as a power law between resolved shear stress and slip rate, such that

$$\dot{\gamma}^\alpha = \dot{\gamma}_0 \left(\frac{\tau^\alpha}{g^\alpha}\right) \left|\frac{\tau^\alpha}{g^\alpha}\right|^{\frac{1}{m}-1} \tag{64}$$

In order to examine the sensitivity of parameters reproducing the stress/strain relation in Fig. 12, the following properties are used (four sets of materials constants are chosen; ❶ indicates set number 1 and so on).

Table 19 Parameters for viscoplastic crystal plasticity calculation.

Materials parameters 1	parent phase	daughter phase
Bulk modulus (GPa)	135.8	150.0
Shear modulus (GPa)	62.7	69.2
H_0 (MPa)	❶50 ❷50 ❸50 ❹ 50	❶2400 ❷2400 ❸4400 ❹3000
τ_0 (MPa)	❶41 ❷37 ❸37 ❹ 37	❶195 ❷195 ❸350 ❹100
τ_s (MPa)	❶55 ❷51 ❸51 ❹ 51	❶290 ❷290 ❸590 ❹350
q	1.0	1.0
m	❶0.2 ❷0.5 ❸0.5 ❹ 0.5	❶0.2 ❷0.2 ❸0.3 ❹ 0.1
$\dot{\gamma}_0$	0.001	0.001
Constitutive model	Hutchinson-Peirce-Pan and Rice (viscoplastic)	
Number of grains	100	100

In these calculations, the parent phase has f.c.c. crystal lattice parameters whereas daughter phase has b.c.c.. For the simplicity, we limit the f.c.c. slip systems to {110} and {112} (see Table 4). Stress/strain curves are reported on (Fig. 61).

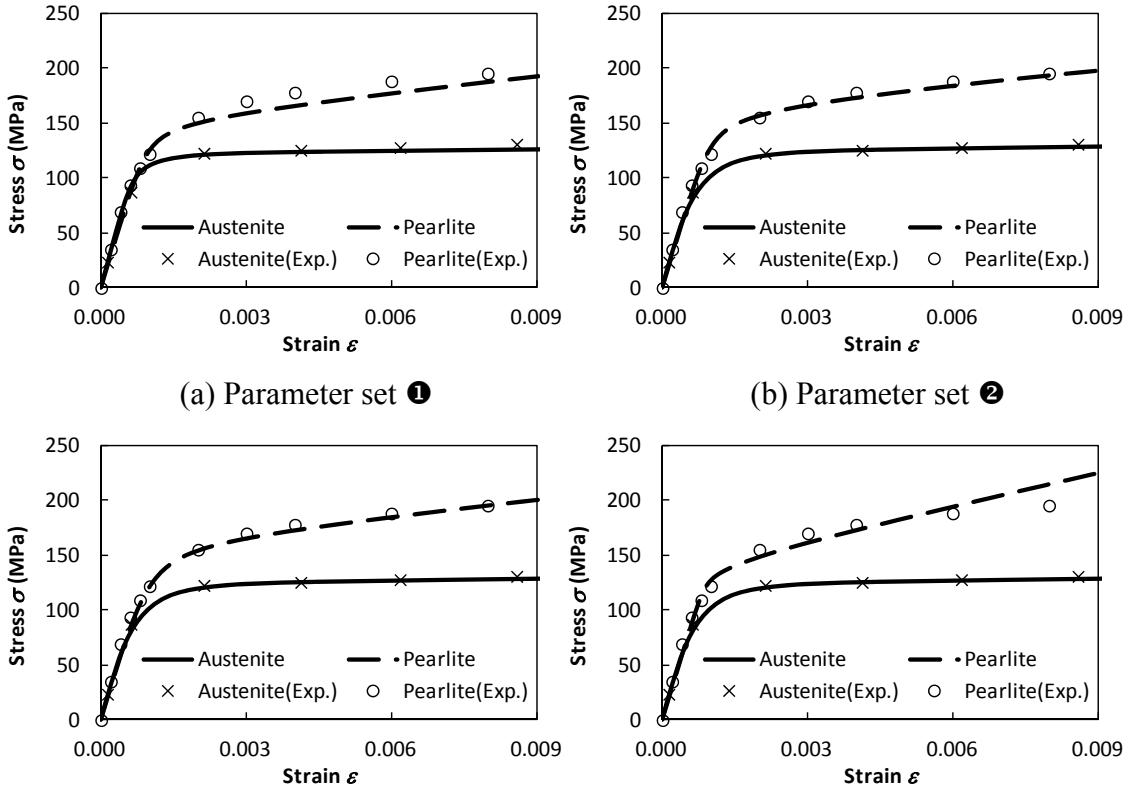

(a) Parameter set ❶ (b) Parameter set ❷

(c) Parameter set ❸ (d) Parameter set ❹

Fig. 61 Stress-strain curves by viscoplastic model.
Parent phase[42]: $\dot{\varepsilon} = 1.0 \times 10^{-2}$ (sec^{-1})
Daughter phase[1]: $\dot{\varepsilon} = 3.3 \times 10^{-5}$ (sec^{-1}) for $\varepsilon < 0.002$,
$\dot{\varepsilon} = 3.3 \times 10^{-4}$ (sec^{-1}) for $\varepsilon \geq 0.002$

The transformation plasticity has also been calculated by the FFT viscoplastic model with these parameter sets. The transformation duration is defined according to the experimental results of S45C pearlitic phase transformation [42]. The calculated evolution of strain in case ❸ is shown in Fig. 62. Others show the similar results; the transformation lasts about 20 seconds for all cases.

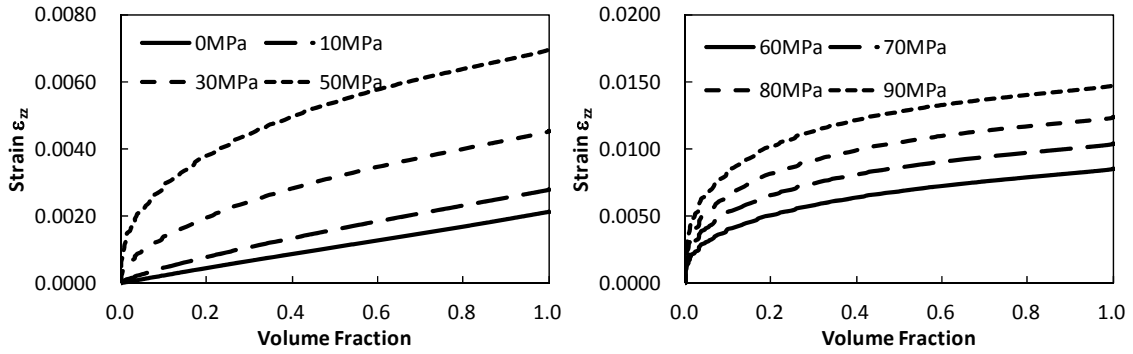

(a) Small applied stress (b) Large applied stress

Fig. 62 Evolution of strain when case ❸.

The strain evolutions in Fig. 62 have more nonlinearity than in Fig. 29 (rate-independent case). It is remarked that the strain evolution is more significant in rate-dependent case especially at the beginning of phase transformation than in rate-independent case. This is caused by the difference of creep resistance in two phases; the parent phase is softer than daughter phase. In fact the strain evolutions when parameters ❸ (Fig. 63) show higher nonlinearity than those of ❶. It is because the m value of parent phase (austenite) in the parameters ❸ is larger than in parameters ❶, and hence more sensitive to the applied stress.

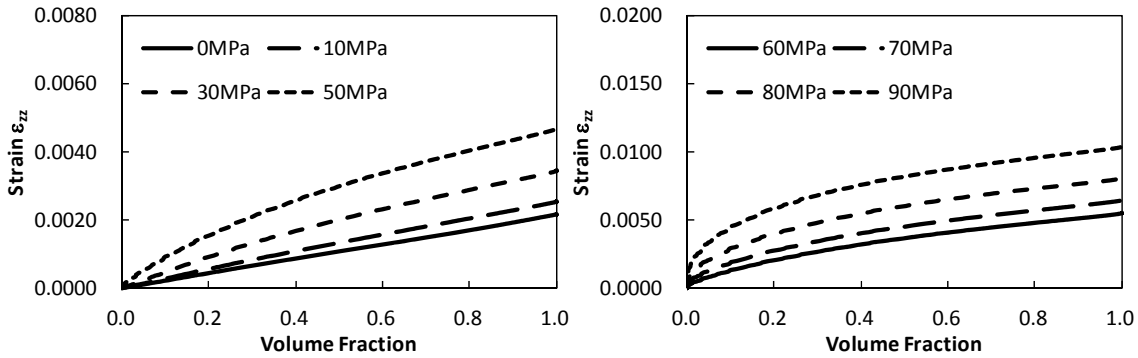

(a) Small applied stress (b) Large applied stress

Fig. 63 Evolution of strain when case ❶.

For all cases, the relation between applied stress and transformation plastic strain is almost linear like rate-independent problems under small applied stresses. It should be emphasised that the results are strongly dependent on chosen parameter sets. These results indicate that for the transformation plasticity at high temperature, the stress-strain

curves should be measured at least at two strain rates. Furthermore, in this case, present analytical models cannot give an appropriate answer.

Table 20 Transformation plastic coefficient results of each parameter set.

	K_P^+ (MPa^{-1})	K_P^- (MPa^{-1})
❶	5.06×10^{-5}	4.87×10^{-5}
❷	10.0×10^{-5}	10.3×10^{-5}
❸	9.74×10^{-5}	9.56×10^{-5}
❹	10.9×10^{-5}	11.0×10^{-5}
Experiment [42]	9.2×10^{-5}	

Table 20 is a summary of transformation plastic coefficient values for each case and experimental one. The transformation plastic coefficients are found to be very sensible with viscoplasticity. The case ❸ is equivalent to the experimental results found in the chapter 3. It may imply that the viscoplastic deformation is responsible for some discrepancies between experimental results (of ferrite or pearlite phase transformation) and both analytical and numerical ones. This means that not only yield stress but also viscoplastic behaviour has to be identified in order to describe accurately transformation plasticity at high temperature.

4.3 A new approximate analytical model

A new approximate analytical model will be proposed in this section. The main feature of the new model is that it considers plastic deformation of daughter phase and that it takes into consideration the external applied stress effect on the deformation of parent phase.

First of all, the plastic deformation of daughter phase is modelled. The existing analytical models consider plastic deformation of the parent phase and elastic deformation of the daughter phase. However, our calculation results by FFT show that the plastic deformation of daughter phase is not negligible especially at the end of phase transformation. Hereafter, the transformation plastic strain will be divided into that of parent phase and of daughter phase, such that:

$$\dot{\varepsilon}_{ij}^{tp} = \dot{\varepsilon}_{ij}^{tp1} + \dot{\varepsilon}_{ij}^{tp2} \ . \tag{157}$$

Second, let us discuss the effect of external stress on the parent phase. Leblond [79] has neglected the effect of external applied stress when calculating equivalent plastic strain of the parent phase. This approximation is valid only when applied stress is enough small (this point will be discussed later). However, for large applied stress, the external stress effect should obviously be considered.

On the other hand, we consider that the daughter phase has a spherical form with surrounding parent phase. We intend to modify the equivalent strain of parent phase in equation (20) by considering external stress effect on the vicinity of daughter phase. We denote the applied stress as σ^{eq}, and we assume that the additional strain caused by external stress reads:

$$\frac{\Delta\varepsilon_1^{eq}(\theta)}{\delta\varepsilon_1^{eq}} = \frac{\sigma^{eq}|\cos\theta|}{\sigma_1^{y}} \ , \tag{158}$$

where θ is an angle between applied stress direction and the normal of the surface of the sphere shaped daughter phase. The average value over the whole crust can be calculated by taking an average throughout the angle:

$$\delta\varepsilon'^{eq}_1 = \delta\varepsilon_1^{eq}\left(1+\frac{1}{\pi}\int_0^{\pi}\frac{\sigma^{eq}|\cos\theta|}{\sigma_1^{y}}d\theta\right) = \delta\varepsilon_1^{eq}\left(1+\frac{2\sigma^{eq}}{\pi\sigma_1^{y}}\right) \ , \tag{159}$$

where $\delta\varepsilon'^{eq}_1$ is newly defined increment of equivalent plastic strain in parent phase with the effect of external stress. The modified transformation plastic strain equation of parent phase takes the form:

$$\dot{\varepsilon}_{ij}^{tp1} = \begin{cases} \left(\frac{-2\beta}{\sigma_1^y}\right)\ln(z_l)\,\dot{z}\,\frac{3}{2}\left(1+\frac{2\sigma^{eq}}{\pi\sigma_1^y}\right)s_{ij} & \text{if} \quad z \le z_l \\ \left(\frac{-2\beta}{\sigma_1^y}\right)\ln(z)\,\dot{z}\,\frac{3}{2}\left(1+\frac{2\sigma^{eq}}{\pi\sigma_1^y}\right)s_{ij} & \text{if} \quad z > z_l \end{cases}, \tag{160}$$

where σ^{eq} denotes equivalent stress of applied stress.

The approximation of an elastic daughter phase is only appropriate when it is much harder than the parent phase such as bainite and martensite phase transformation. In addition, it is observed the plastic strain of daughter phase is important in the late stage of phase transformation.

Let us again consider the same model employed by Leblond and Taleb, infinite parent phase with a spherical inclusion of daughter phase. In this case, the stress state of daughter phase can be considered to be uniform. When the external stress σ is applied on z-direction, the three components of normal stress with angle θ from the direction of applied stress can be expressed as follows.

$$\begin{aligned} \sigma_x = \sigma_y &= \left(\sigma\sin\theta - \sqrt{\frac{1}{3}\left(\sigma_2^y\right)^2 - \frac{1}{2}\sigma^2\cos^2\theta}\right)\cdot|\cos\theta|\,, \\ \sigma_z &= \sigma(1+\sin^2\theta) - \sqrt{\frac{1}{3}\left(\sigma_2^y\right)^2 - \frac{1}{2}\sigma^2\cos^2\theta}\cdot\sin\theta\,. \end{aligned} \tag{161}$$

So, the deviatoric component in z direction will be:

$$\begin{aligned} s_z = \frac{2}{3}\Bigg\{&\sigma(1+\sin^2\theta-\sin\theta\,|\cos\theta|) - \sqrt{\frac{1}{3}\left(\sigma_2^y\right)^2 - \frac{1}{2}\sigma^2\cos^2\theta} \\ &\cdot(\sin\theta - |\cos\theta|)\Bigg\}\,. \end{aligned} \tag{162}$$

If one takes the average value over $0 \le \theta \le \pi$,

$$\frac{1}{\pi}\int_0^{\pi} s_z\,d\theta \cong \frac{2}{3}\left(\frac{3}{2}-\frac{1}{\pi}\right)\,. \tag{163}$$

So, by using Levy-Mises formula, the transformation plastic strain rate of daughter phase can be expressed as:

$$\dot{\varepsilon}_{ij}^{tp2} = \begin{cases} 0 & \text{if} \quad z \le z_l \\ \frac{\beta}{\sigma_2^y}\dot{z}\left(\frac{3}{2}-\frac{1}{\pi}\right)s_{ij} & \text{if} \quad z > z_l \end{cases}, \tag{164}$$

here z_l is defined in equation (23) but it should be calculated with the materials

parameters of daughter phase. If the yield strength of the new phase is high enough, compared to the parent phase, and the applied stress is small, the new model reduces Taleb's model [17].

4.3.1 Assessment of a new model - rate independent case -

4.3.1.1 Case of small transformation expansion ($\beta = 1.5 \times 10^{-3}$)

In this section, the proposed model and existing models are assessed by comparison with reference by FFT computations.

First of all, the transformation plastic strain values which are calculated by FFT when phase transformation is completed are plotted in Fig. 64. Here, transformation plastic strain by FFT is calculated with following definition.

$$\varepsilon^{tp} = \langle \varepsilon^{total} \rangle - \langle \varepsilon^{e} \rangle - \langle z \rangle \beta \,, \tag{165}$$

where $\langle \varepsilon^{total} \rangle$ and $\langle z \rangle$ are average total uniaxial strain along the applied stress direction and average volume fraction and $\langle \varepsilon^{e} \rangle$ is elastic strain. Note that the line "Leblond" signifies equation (7) and "Leblond-Mod." is equation (8). "Leblond-Mod" is an enhanced "Leblond" model considering nonlinearity under high external stress.

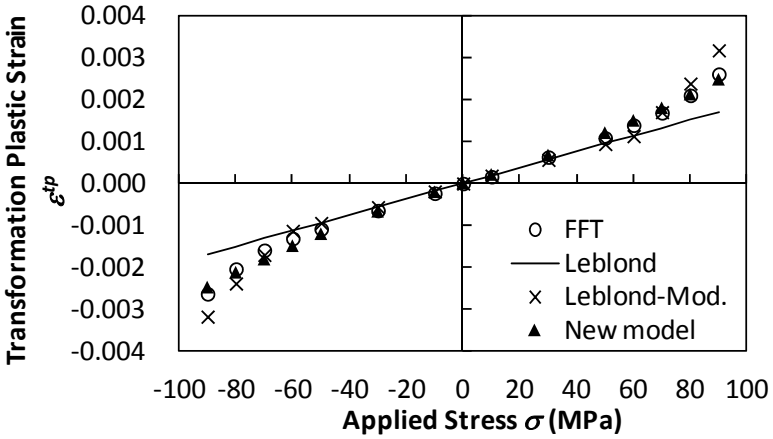

Fig. 64 Relation between applied stress and transformation plastic strain.

One can observe in the Fig. 64 the linear relation between applied stress and transformation plastic strain when applied stress is less than 60 MPa. This relation agrees with models by Greenwood-Johnson, Leblond or Inoue. The factors of proportionality (transformation plasticity coefficient) are; $K_P = 2.20 \times 10^{-5}$ (MPa^{-1}) for tensile and $K_P = 2.15 \times 10^{-5}$ (MPa^{-1}) for compressive applied stresses. Thus, there is no significant difference between tensile and compressive applied stresses. On the other hand, according to Leblond's model, transformation plasticity coefficient is $K_P = 2.17 \times 10^{-5}$

(MPa^{-1}). This appears to be in good quantitative agreement.

For the large applied stresses, the results by FFT predict well the experimental evidence that the relation between applied stress and transformation plastic strain will be nonlinear. Leblond's modified model (to describe nonlinearity) overestimates transformation plastic strain at large applied stresses. On the other hand, the new model successfully estimates the transformation plasticity for all stress regimes.

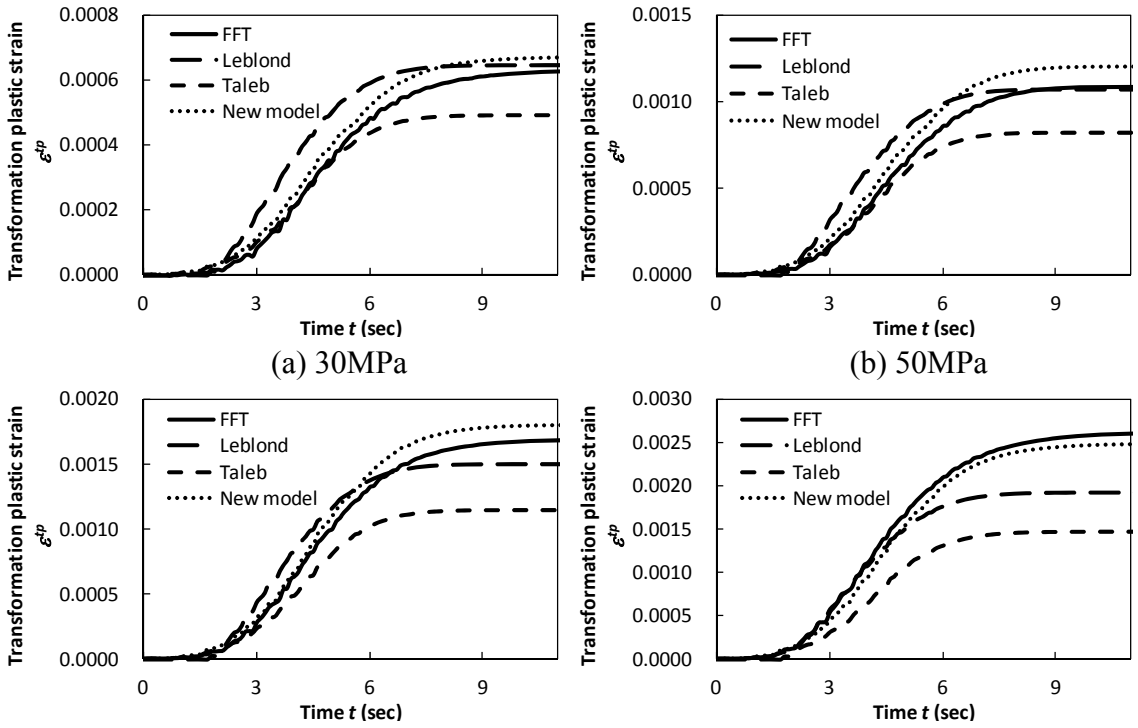

Fig. 65 Comparison of evolution of transformation plastic strain.

Second, the whole kinetics of transformation plastic strain evolution during phase transformation is analysed. Fig. 65 shows the comparison of evolution curves of transformation plastic strain among FFT, model by Leblond (7) and model by Taleb (22). According to Fig. 65, Taleb's model and FFT results agree well at the beginning of phase transformation. In contrast, Leblond's model overestimates transformation plastic strain at this stage especially under small applied stresses (figures (a), (b) and (c)). This agreement of Taleb's model and FFT results at the first stage can be explained by Taleb's modification after Leblond's model: it takes into account the fact that not the entire parent phase is subjected to plastic deformation at the beginning of phase transformation. The modification is rather important when transformation expansion is relatively small.

Both Leblond's and Taleb's models underestimate the transformation plastic strain at the

latter half of phase transformation for every condition. This means that Leblond's model overestimates the transformation plastic strain with respect to FFT results at the first stage, which is compensated by the underestimation at the final stage. On the other hand, for Taleb's model, due to its agreement at the first stage, an underestimation at the final stage remains. This derives from the assumption that daughter phase is much stronger than parent phase and so the plastic deformation of daughter phase can be neglected. This explanation will be confirmed in the sequel.

Effect of plastic deformation of daughter phase

In order to distinguish the contribution of parent and daughter phases, equivalent plastic strain of each phase during phase transformation is calculated. These results are depicted in Fig. 66.

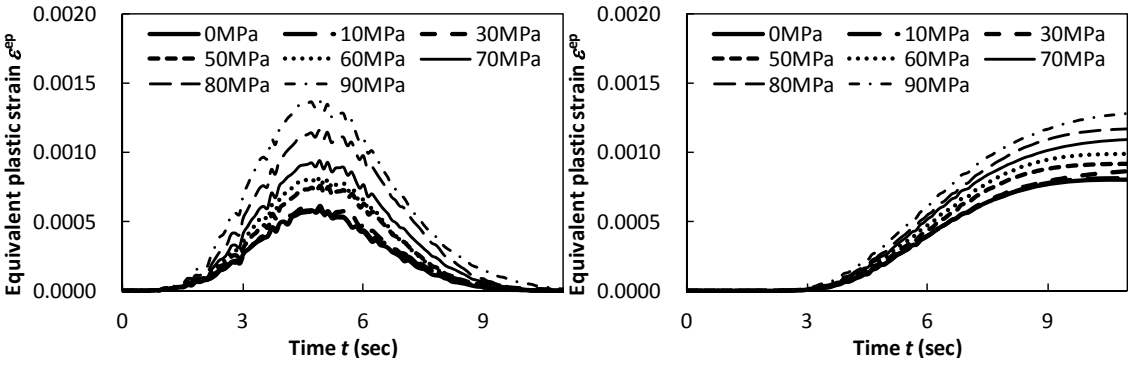

(a) parent phase (b) daughter phase

Fig. 66 Strain evolutions of parent and daughter phases during phase transformation.

The equivalent plastic strain of parent phase increases with the volume fraction during the first half of phase transformation and it decreases during latter half. The equivalent plastic strain in parent phase decreases along with diminishing parent phase by phase transformation.

On the other hand, the equivalent plastic strain in daughter phase start to increase at about 50% transformed point and it continues to increase until the end of phase transformation. The equivalent plastic strain in daughter phase is not negligible especially at latter half of phase transformation.

From these discussions, it can be concluded that the underestimation of Leblond's and Taleb's models in the latter half of phase transformation derives from the assumption of elastic daughter phase. This supports the idea of equation (157) of the newly proposed

model.

To confirm this analysis, FFT simulations with elastoplastic parent and elastic daughter phases are carried out. The macroscopic stress/strain relations of parent and daughter phases calculated by using the same FFT model are shown in Fig. 67. The comparison among models by FFT, Leblond's equation (7), Taleb's equation (22) and new model (157)-(164) under several applied stresses are shown in Fig. 68.

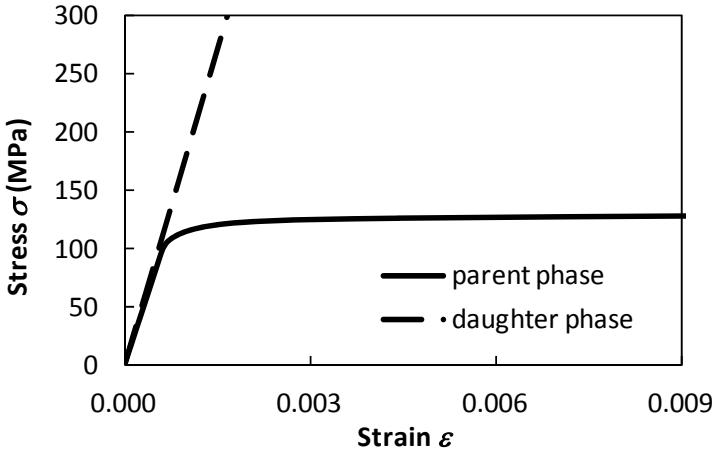

Fig. 67 Macroscopic stress/strain curves of parent (elastoplastic) and daughter (elastic) phases.

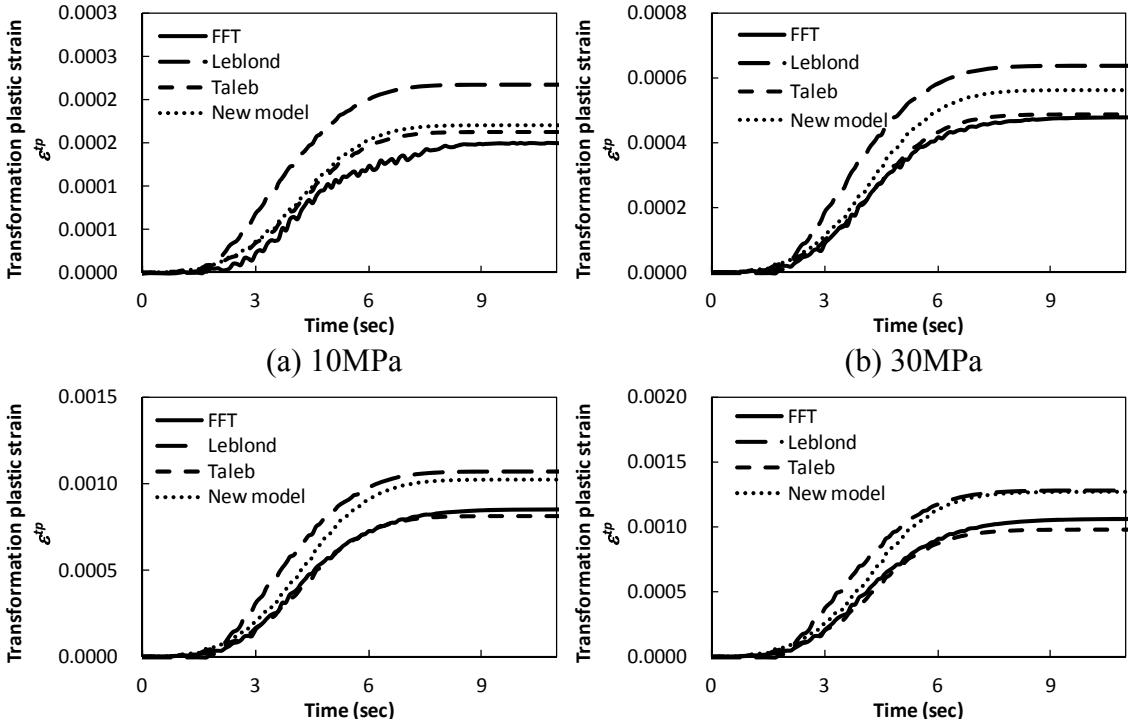

(a) 10MPa (b) 30MPa

(c) 50MPa (d) 60MPa

Fig. 68 Comparison of evolution of transformation plastic strain (daughter: elastic case).

Fig. 68 shows that Taleb's equation (22) agrees well with FFT calculation results. This is yet another evidence; Leblond's model agrees well with FFT model at the end of the phase transformation and it is because Leblond's model overestimates the transformation plasticity at the first half and it compensate the underestimation at the latter half; Taleb's model agrees well during first half of phase transformation and during latter half when daughter phase is elastic but underestimates during latter half when daughter phase is elastoplastic.

The disagreement of FFT results and those of new model is considered to be caused by over estimation of plastic deformation of parent phase. This suggests that a correlation between yield stresses of parent and daughter phases should be incorporated.

Fig. 69 represents relation between applied stress and transformation plastic strain for daughter phase elastic condition. The transformation plasticity coefficient is calculated as $K_P = 1.68 \times 10^{-5}$ (MPa^{-1}) and again there is no significant difference between tensile and compressive stress conditions. Comparing to the daughter phase elastoplastic case, the transformation plasticity coefficient value is about 20% smaller for daughter phase elastic case. This appears also to be quantitative agreement with the difference between FFT model and Taleb's model at the end of phase transformation.

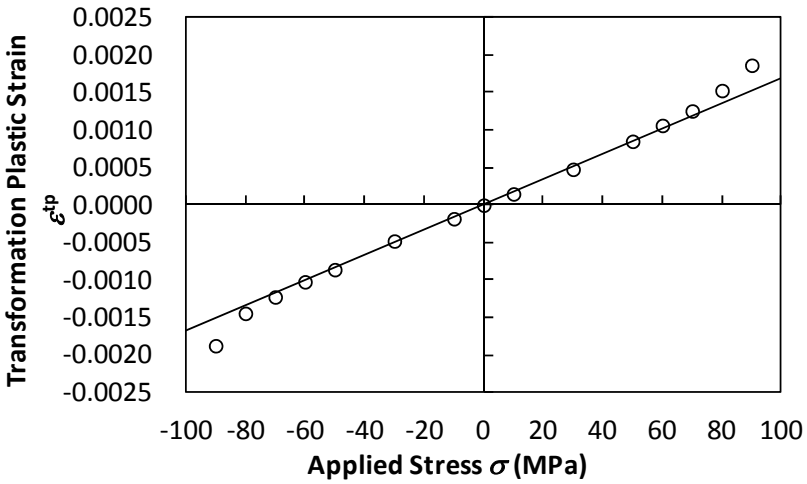

Fig. 69 Relation between applied stress and transformation plastic strain (Pearlite: elastic case).

Finally, in order to know the performance of each model, transformation plasticity calculation by FFT under increasing/decreasing stress loading conditions are carried out. The stress conditions and calculated transformation plastic strain are shown in Fig. 70.

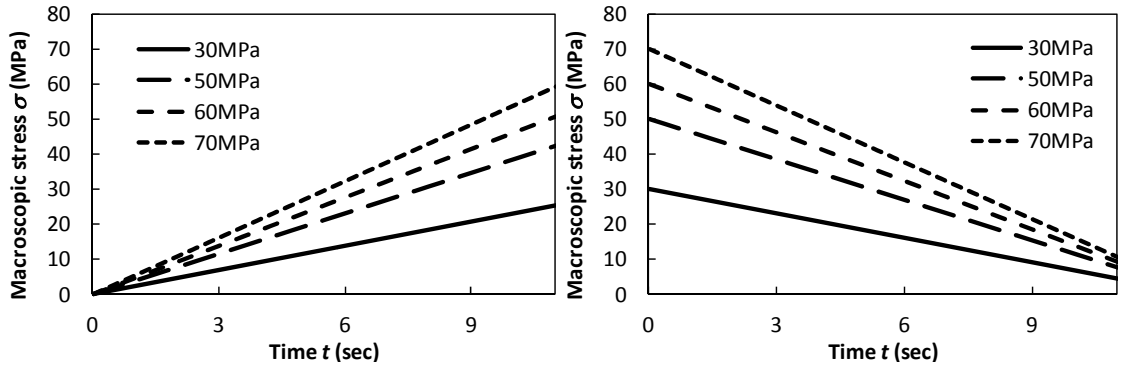

(a-1) Increasing stress (a-2) Decreasing stress

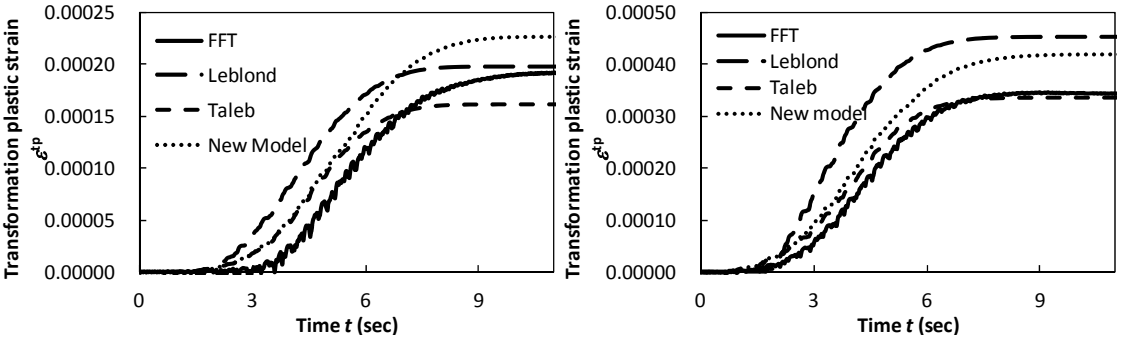

(b-1) 0 - 30MPa (b-2) 30 - 0MPa

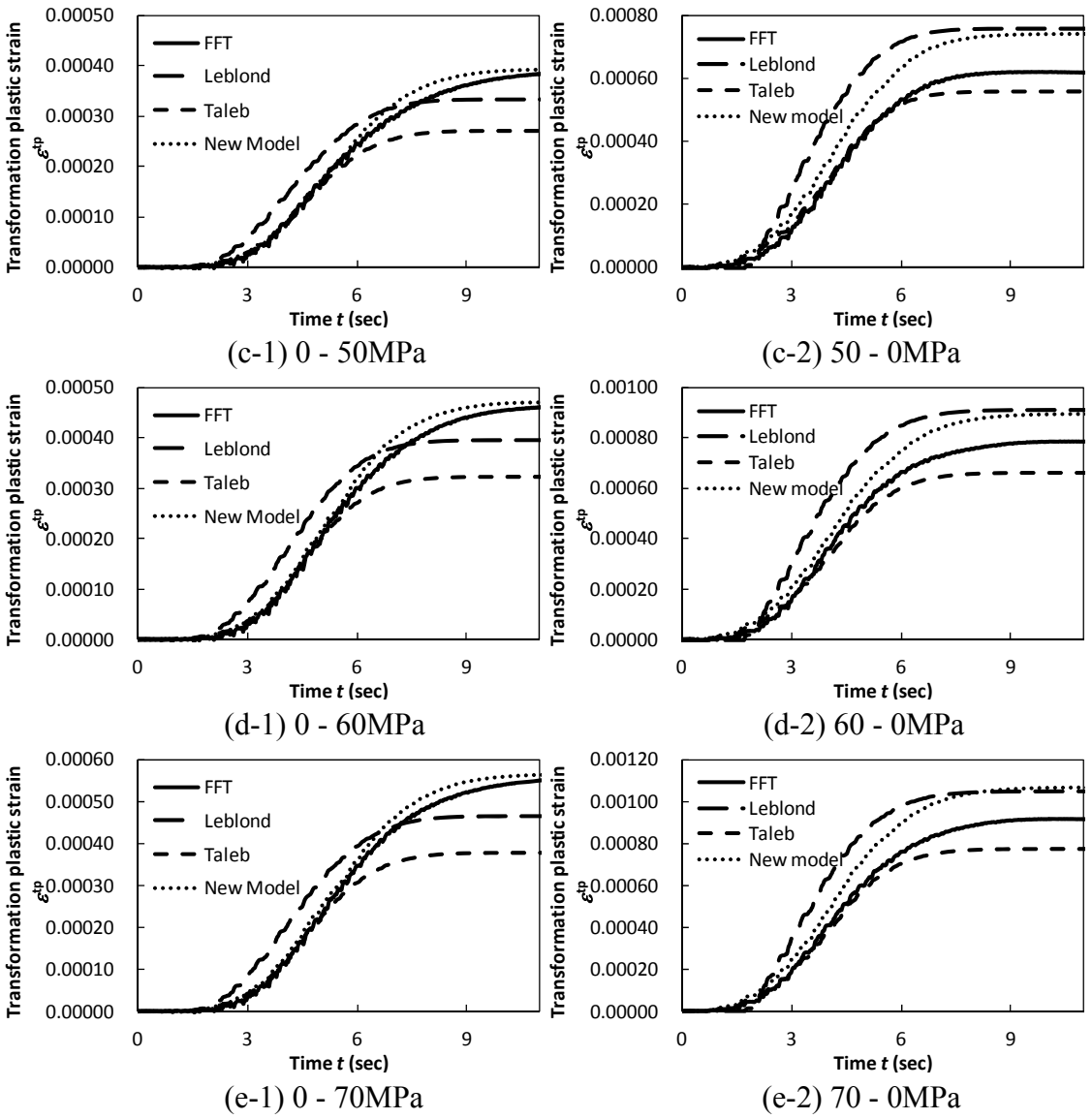

(c-1) 0 - 50MPa (c-2) 50 - 0MPa

(d-1) 0 - 60MPa (d-2) 60 - 0MPa

(e-1) 0 - 70MPa (e-2) 70 - 0MPa

Fig. 70 Variation of transformation plastic strain under linearly changing stress conditions.

For the stress increasing condition, the new model estimates well the transformation plasticity. However, there are differences between new model and FFT results under small applied stress. It seems that there is a threshold stress (about 5MPa in this case) for obtaining transformation plasticity.

To sum up, plastic deformation of daughter phase occurs during latter half of phase transformation and the value is about 20% of total plastic deformation magnitude. Leblond's model agrees well with FFT model in the sense of transformation plastic coefficient because it overestimates transformation plasticity at the beginning of phase transformation and it compensated by an underestimation during the latter half. Taleb's

model agrees well with FFT during first stage of phase transformation but it under estimates during last stage; the model estimates well if the daughter phase is elastic. The proposed model agrees well FFT throughout phase transformation. Even though the new model gives the best estimation among those models, it overestimates the plastic deformation of daughter phase, and therefore, it overestimates transformation plasticity at latter half of phase transformation.

Mechanism that causes nonlinearity under high applied stress

When the applied stress is large, both Leblond's and Taleb's model underestimate transformation plastic strain as are shown in figure (c) and (d). In these cases, the linear relation between transformation plastic strain and applied stress is never satisfied (Fig. 64). The reason of this nonlinearity is investigated by FFT computations.

Many models, such as Greenwood-Johnson [5] or Inoue [87], describe that applied stress is linear to transformation plastic strain. Therefore, they are valid only under small applied stress conditions. As previously discussed, experimental results show that when the applied stress exceeds a half the value of yield stress of parent phase, non-linearity occurs.

Leblond has analytically modelled transformation plasticity along with Greenwood-Johnson mechanism [15]. This model consists of 5 main hypotheses which are recalled here.

H1. The microscopic elastic compliance tensor may be equated to the macroscopic overall elastic compliance tensor.

H2. For small or moderately high applied stresses, the austenitic phase is entirely plastic, but the α phase remains elastic or its plastic strain rate remains always much smaller than that of the γ phase.

H3. Both phases are ideal-plastic and obey the von Mises criterion and the Prandtl-Reuss flow rule.

H4. Correlations between $\delta\varepsilon_1^{eq}/\delta z$ and s_1 can be neglected.

H5. For small applied stresses, the average stress deviator in phase 1 is almost equal to the overall average stress deviator.

We now intend to check which assumptions remain valid for the high applied stress regime.

Hypothesis 1 is fulfilled because local elastic anisotropy does not significantly affect transformation plasticity.

Concerning hypothesis 2, Fig. 71 shows equivalent plastic strain distribution at 50% transformed state calculated by FFT (64^3 voxels, 100 grains). The results show that most

voxels remain elastic, which is against the hypothesis. The larger the applied stress, the more voxels deform plastically. It means that even though there are many parts which remain elastic, this hypothesis cannot be the reason for the nonlinearity under high applied stress.

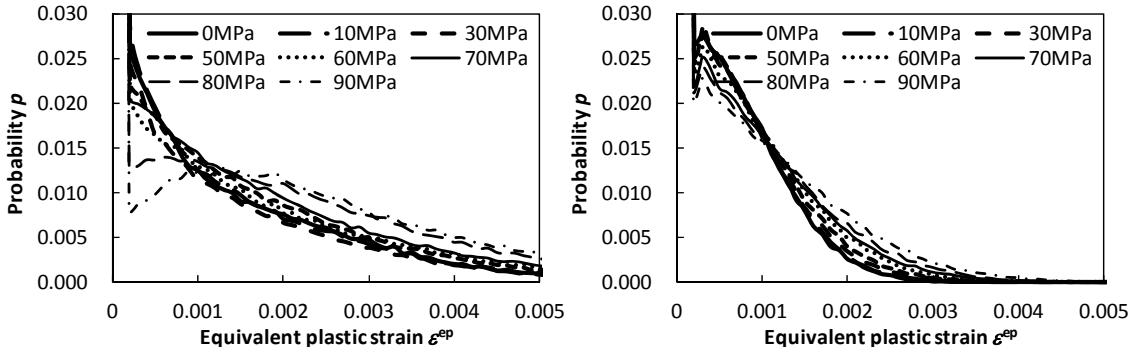

(a) Parent phase (b) Daughter phase

Fig. 71 Equivalent plastic strain distribution at $\xi = 0.5$.

We do not discuss hypothesis 3 since we perform the calculations of crystal plasticity which is not relevant to von Mises and Prandtl-Reuss models.

Hypothesis 4 can be verified by numerical results. The terms $\langle \delta\varepsilon_1^{eq}/\delta\xi \cdot s_1 \rangle_{V_1}$ (Line 1) and $\langle \delta\varepsilon_1^{eq}/\delta\xi \rangle_{V_1} \cdot \langle s_1 \rangle_{V_1}$ (Line 2) are to be calculated during phase transformation. The comparison of these two values is shown in Fig. 72.

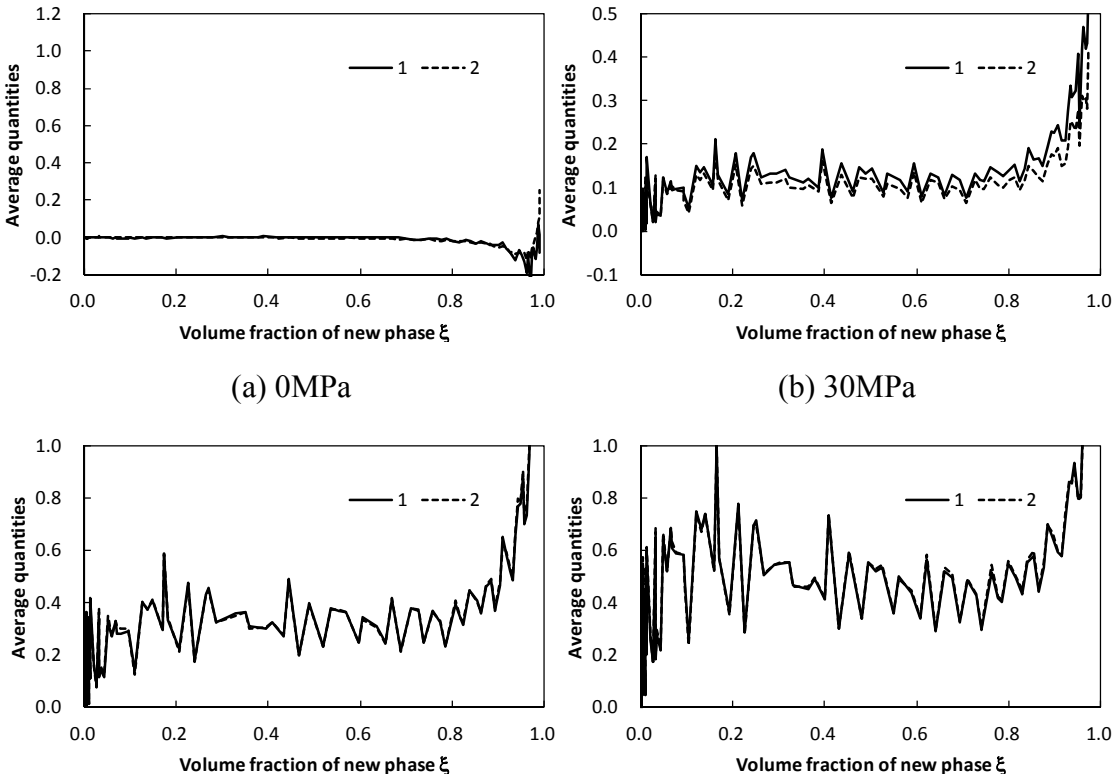

(a) 0MPa (b) 30MPa

(c) 70MPa (d) 90MPa

Fig. 72 Effect of correlation between $\delta\varepsilon_1^{eq}/\delta z$ (1) and s_1 (2) at several applied stress.

According to Fig. 72, it is clear that correlation between $\delta\varepsilon_1^{eq}/\delta z$ and s_1 can be neglected. Thus, the hypothesis 4 is well verified. In fact, as shown in Fig. 73, the resultant transformation plastic strains calculated with H.4 and without H.4 do not show substantive difference. This verification has also been performed by Leblond *et al*. [15] by using FEM with J_2 plasticity.

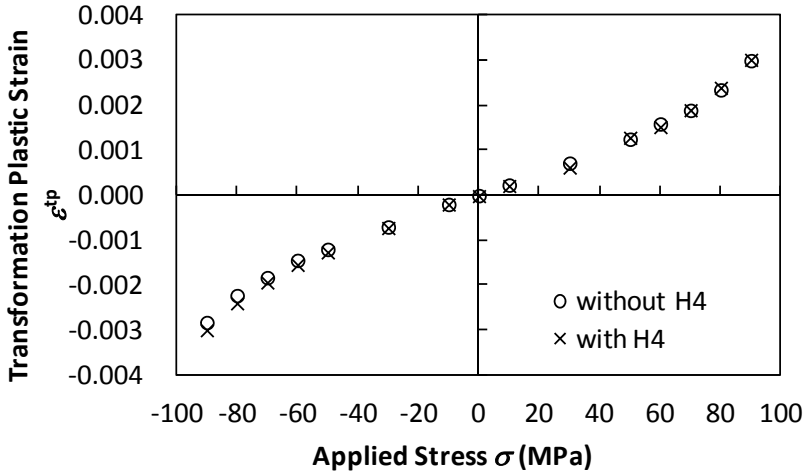

Fig. 73 Effect of correlation between $\delta\varepsilon_1^{eq}/\delta z$ and s_1.

Hypothesis 5 is also verified by numerically. As for H.4, the average stress value of phase 1 and overall stress (average stress of both phase 1 and phase 2) are shown in Fig. 74.

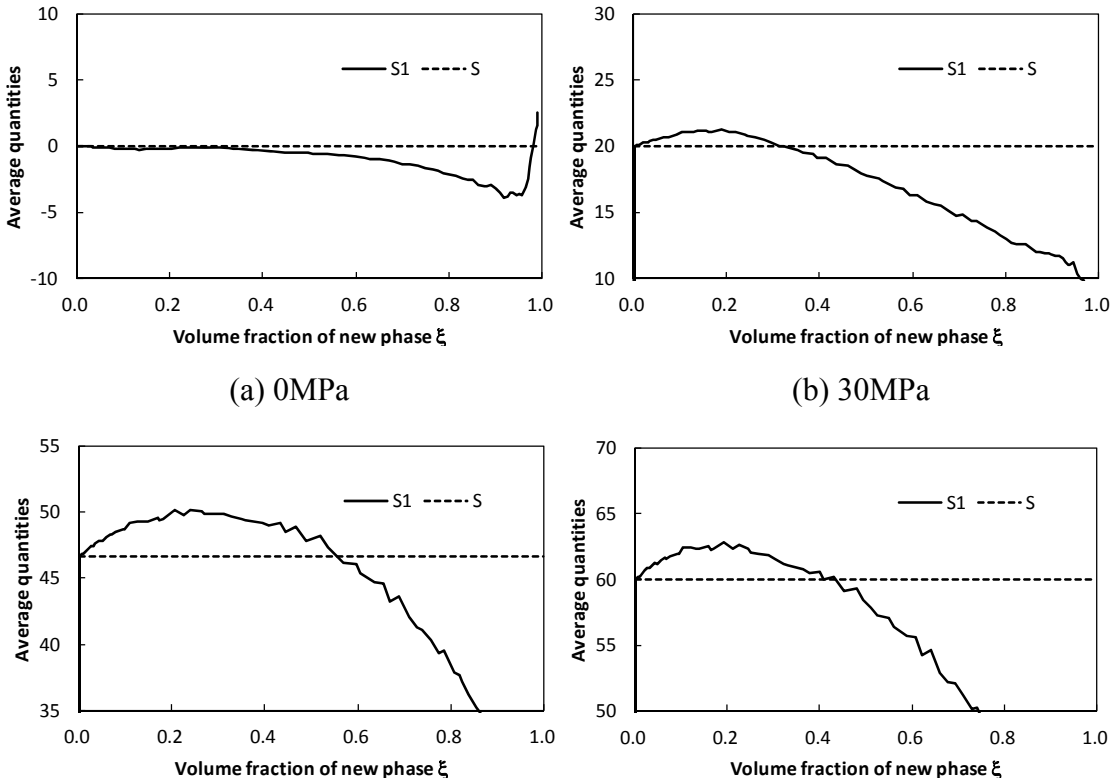

(a) 0MPa (b) 30MPa

(c) 70MPa (d) 90MPa

Fig. 74 Difference between average stress value of phase 1 and overall stress.

The maximum difference between average stress of phase 1 and overall stress until 50% phase transformation is less than 7%. So the hypothesis 5 is likely to be valid. To confirm this, the transformation plastic strain values with several applied stress are shown in Fig. 75; $\langle \delta\varepsilon_1^{eq}/\delta z\rangle_{V_1} \cdot \langle s_1\rangle_{V_1}$ without H.5 and $\langle \delta\varepsilon_1^{eq}/\delta z\rangle_{V_1} \cdot S$ with H.5. In this case, $\langle \delta\varepsilon_1^{eq}/\delta z\rangle_{V_1}$ is calculated by using analytical solution given by equation (21). As shown in Fig. 75, the hypothesis 5 is well verified.

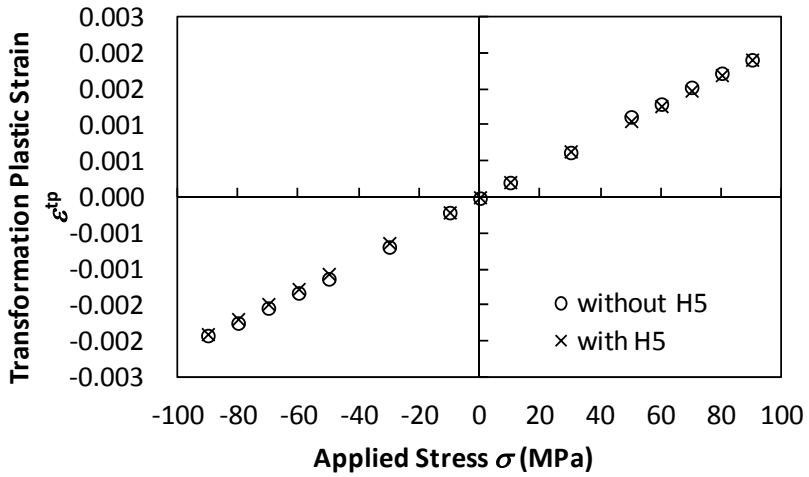

Fig. 75 Difference between average stress value of phase 1 and overall stress.

In contrast to Fig. 73, where one can observe the nonlinearity between applied stress and transformation plastic strain, Fig. 75 shows linear relation between them; the difference seems to arise from whether the term $\langle \delta\varepsilon_1^{eq}/\delta z\rangle_{V_1}$ is calculated by FFT or by analytic solution given by equation (21).

Fig. 76 shows the transformation plastic strains calculated by equation (16) in which the term $\langle \delta\varepsilon_1^{eq}/\delta z\rangle_{V_1}$.is given by analytical solution using equation (21) (1. circle symbol) and FFT solution (2. cross symbol). An important discrepancy is observed.

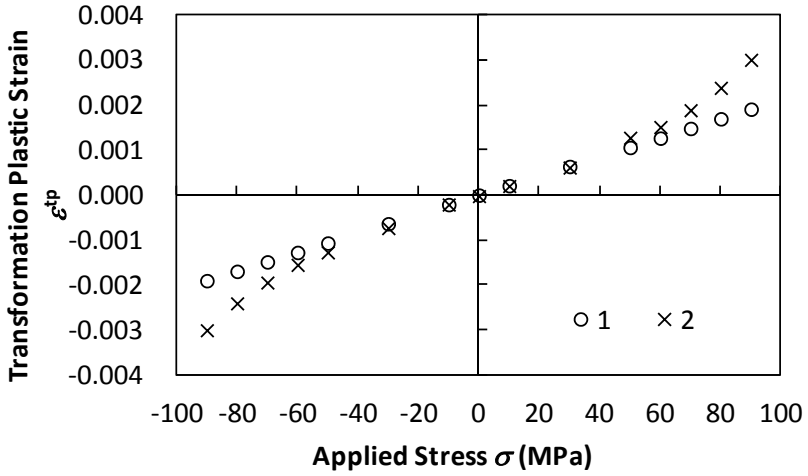

Fig. 76 Difference between analytical solution (circle) and FFT (cross) for $\langle \delta\varepsilon_1^{eq}/\delta\xi \rangle_{V_1}$.

From thse discussions, it can be concluded that the estimation of term $\langle \delta\varepsilon_1^{eq}/\delta z \rangle_{V_1}$ is responsible for the nonlinearity under high applied stress condition. In addition, it shows that the analytical solution given by equation (21) is accurate for small applied stress but it is not valid under high applied stress value.

The reason why equation (21) is invalid under high applied stress is that the equivalent strain increment $\delta\varepsilon^{eq}(x)$ is supposed to be initiated only by transformation expansion as shown in equation (20). The assumption is valid under small applied stress but applied stress effect on equivalent strain increment is no longer negligible when applied stress is large.

4.3.1.2 Case of large transformation expansion ($\beta = 4.4 \times 10^{-3}$)

The case of large transformation expansion is now analysed. The constitutive relations are the same as those used for the small transformation expansion case. The calculated final values for the transformation plastic strain as a function of several applied stresses are plotted in Fig. 77.

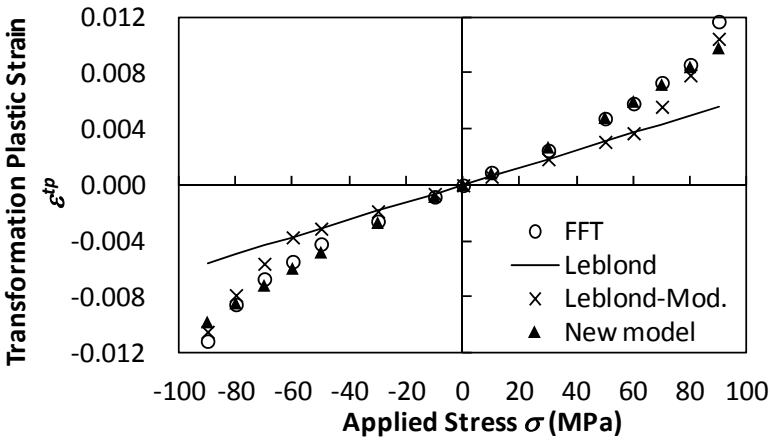

Fig. 77 Relation between applied stress and transformation plastic strain.

For this large transformation expansion case, the nonlinearity of the relationship between applied stress and transformation plastic strain starts at relatively smaller stresses compared to the small transformation expansion case. In both cases, the new model estimates correctly the magnitude of transformation plastic strain calculated by FFT. Especially, it is observed that the nonlinear threshold between applied stress and transformation plastic strain is smaller than the half-value of the yield stress of the weaker phase. By contraries, the modified Leblond's model assumes a nonlinear relation between applied stress and transformation plastic strain only when the applied stress is larger than a half value of yield stress of weaker phase. This causes an underestimation of the transformation strain when applied stresses are larger than 30 MPa. It means that the classical assumption that the nonlinearity starts from the half the value of the yield stress is not always valid. In other words, the threshold value is not only a function of the yield stress of the weaker phase but it also depends on the magnitude of the transformation expansion.

Fig. 78 shows the evolution of the transformation plastic strain with time for selected applied stresses.

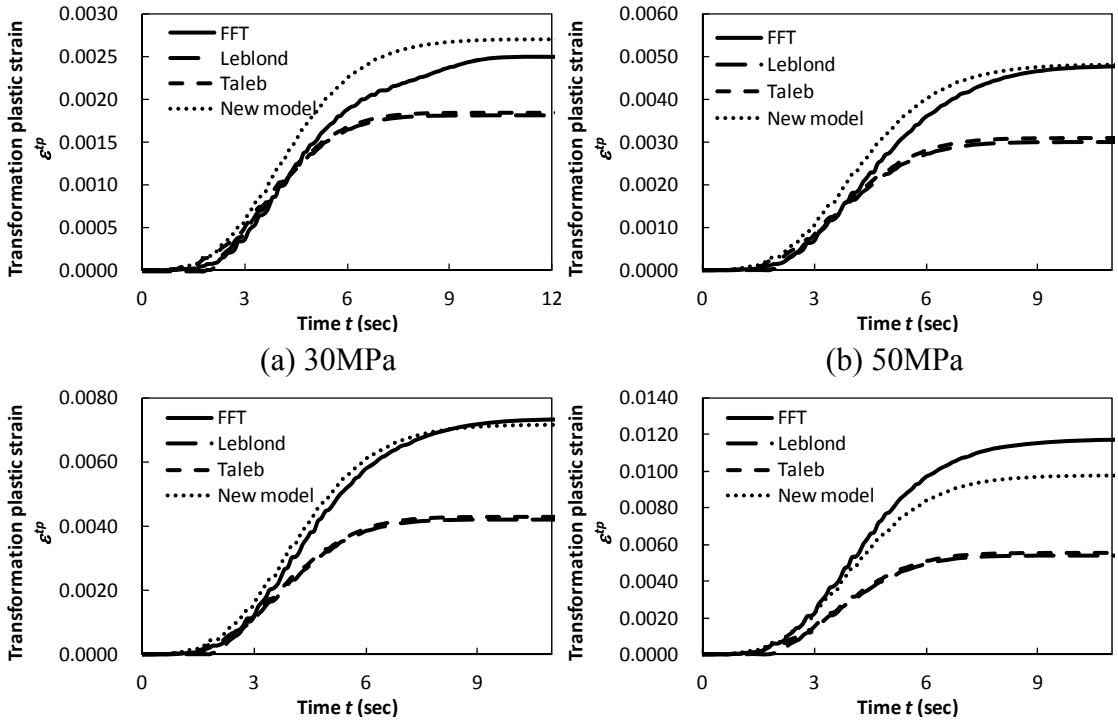

(a) 30MPa (b) 50MPa

(c) 70MPa (d) 90MPa

Fig. 78 Comparison of evolution of transformation plastic strain.

In this case, Leblond and Taleb models predict almost the same values because of the short period until the parent phase undergoes entirely plastic deformation. In addition, these two models greatly underestimate the transformation plastic strain under any applied stress conditions. The primary reason for these rather large discrepancies is that the effect of external stress on plastic strain in parent phase is more significant for large transformation expansion because much more parent phases undertake plastic deformation when the transformation expansion is larger than in small transformation expansion case. Secondly, these models always omit the plastic deformation of the daughter phase. The plastic deformation in daughter phase is also larger when transformation expansion is larger than in small transformation expansion case.

If one takes the average slope of transformation plastic strain calculated by the FFT numerical model and proposed new model between 0 and 50 (MPa) applied stresses, the transformation plastic coefficients are $K_P = 9.38 \times 10^{-5}$ (MPa^{-1}) and $K_P = 9.63 \times 10^{-5}$ (MPa^{-1}) respectively. On the other hand Leblond's model predicts $K_P = 6.20 \times 10^{-5}$ (MPa^{-1}), which is smaller than FFT result and that of new model.

4.3.2 Viscoplasticity (rate-dependent model)

An enhanced analytic model of transformation plasticity will be proposed by considering creep strain following the previous numerical investigation on viscoplasticity.

Let us define a creep constitutive equation as:

$$\dot{\varepsilon}_{ij}^{c} = A(\sigma^{eq})^{n-1}\,\sigma_{ij}\,, \tag{166}$$

where A and n are fitting parameters.

In this case, the local stress on the parent phase crust which surrounds the daughter phase caused by phase transformation can be expressed as follows.

$$\sigma = \left(\frac{\beta z \dot{z}}{A}\right)^{\frac{1}{n}}\,. \tag{167}$$

Analogous to the discussion on elastoplasticity, the additional effect by external stress is introduced. Hence, the final form of the equation is given as follows.

$$\dot{\varepsilon}_{ij}^{tp1} = \begin{cases} \dfrac{-2A_1}{3}\left\{\left(\dfrac{\beta z \dot{z}}{A_1}\right)^{\frac{1}{n_1}} + \dfrac{2\sigma^{eq}}{\pi}\right\}^{n_1-1} \ln(z_l)\,\sigma_{ij} \quad \text{if} \quad z \le z_l \\ \dfrac{-2A_1}{3}\left\{\left(\dfrac{\beta z \dot{z}}{A_1}\right)^{\frac{1}{n_1}} + \dfrac{2\sigma^{eq}}{\pi}\right\}^{n_1-1} \ln(z)\,\sigma_{ij} \quad \text{if} \quad z > z_l \end{cases}, \tag{168}$$

$$\dot{\varepsilon}_{ij}^{tp2} = \begin{cases} 0 \quad \text{if} \quad z \le z_l \\ \dfrac{2A_2}{3}\left(\dfrac{3}{2} - \dfrac{1}{\pi}\right)\left(\dfrac{\beta \dot{z}}{A_2}\right)^{\frac{n_2-1}{n_2}} \sigma_{ij} \quad \text{if} \quad z > z_l \end{cases}. \tag{169}$$

For the purpose of indentifying the parameters A and n in equations (166) and (168)-(169), the creep strain evolutions under 30, 50, 70 and 90MPa constant applied stresses are calculated. These parameters are identified by using least square method, and the fitted results are shown in Table 21. Note that the stresses are defined in MPa unit.

Table 21 Parameters for viscoplastic crystal plasticity calculation.

	A_1 (parent)	A_2 (daughter)	n_1 (parent)	n_2 (daughter)
❶	5.66×10^{-13}	4.04×10^{-16}	4.58	4.78
❷	9.66×10^{-7}	4.04×10^{-16}	1.60	4.78
❸	9.63×10^{-7}	3.03×10^{-14}	1.60	4.00
❹	9.63×10^{-7}	0.00	1.60	1.00

The computational results of uniaxial tensile calculation by FFT using crystal plasticity with viscoplastic constitutive model (equation (64) with each parameter set designated in Table 19) have been carried out. The example of comparison between FFT results and

equation (166) with parameter set ❸ in Table 21 are shown in Fig. 79. It shows that the fitting procedure (to obtain Table 21) has been successfully performed.

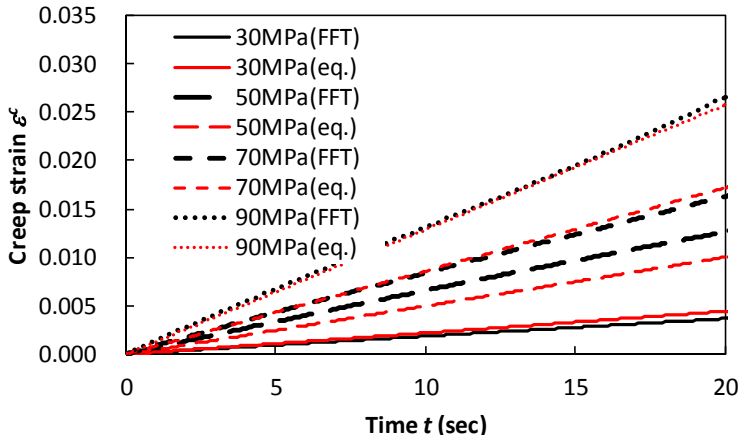

(a) Parent phase

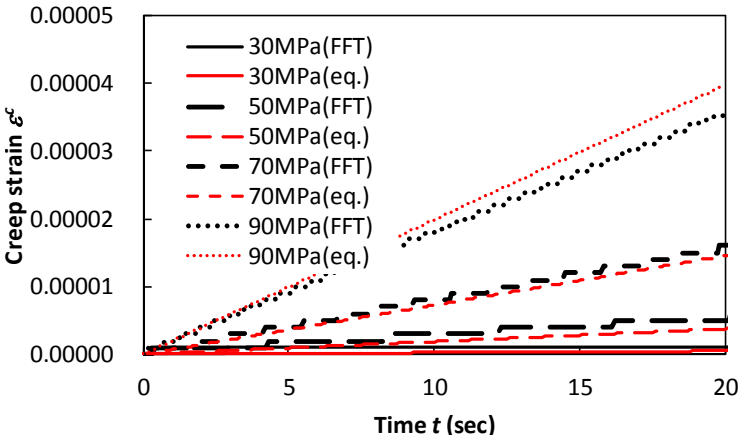

(b) Daughter phase

Fig. 79 Identification of creep parameters for case ❸.
(the label "eq." signifies equation (166))

The results of transformation plastic strain at the end of phase transformation are shown in Fig. 80. The new model agrees well with FFT numerical results for parameter sets ❶, ❷ and ❸, whereas it underestimates for parameter sets ❹. The reason why it underestimates for the case ❹ is that the work hardening of daughter phase (Fig. 61) is much larger in the case ❹ than others. This point indicates that the proposed model requires further improvements.

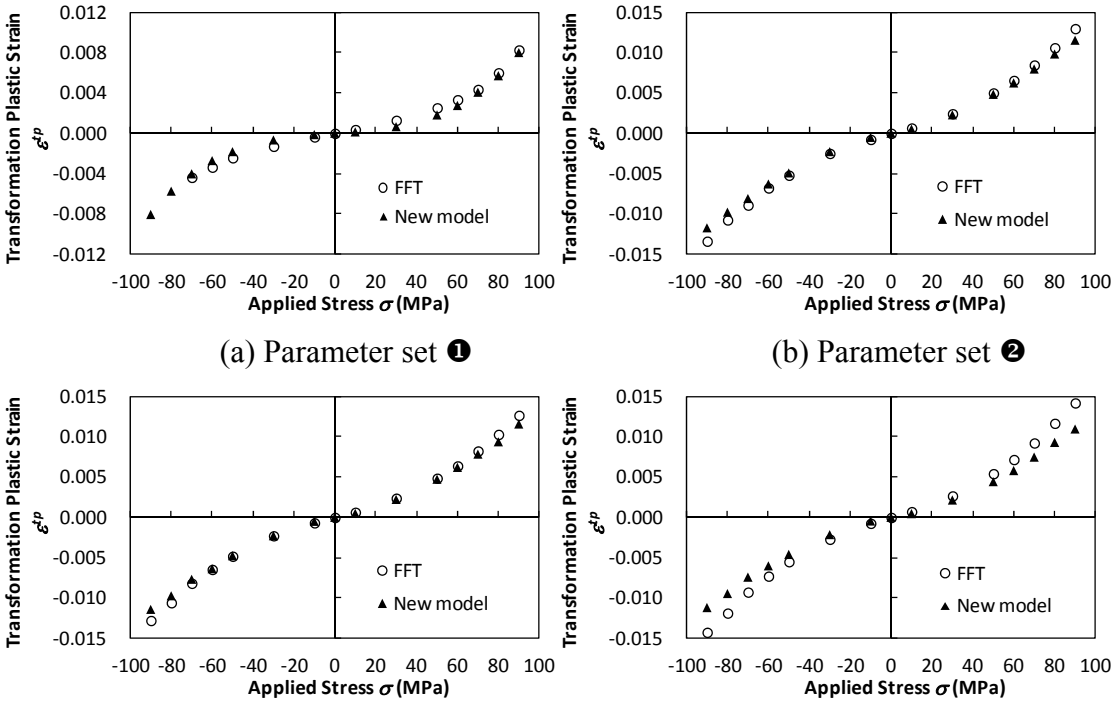

(a) Parameter set ❶ (b) Parameter set ❷

(c) Parameter set ❸ (d) Parameter set ❹

Fig. 80 Calculated transformation plastic strain with viscoplasticity.

4.3.3 Comparison with experimental results at high temperature

The calculated results of evolution of transformation plastic strain (including transformation dilatation) by using FFT numerical scheme (with parameter set ❸ in Table 19) are confronted with experimental ones (see in chapter 3) on Fig. 81.

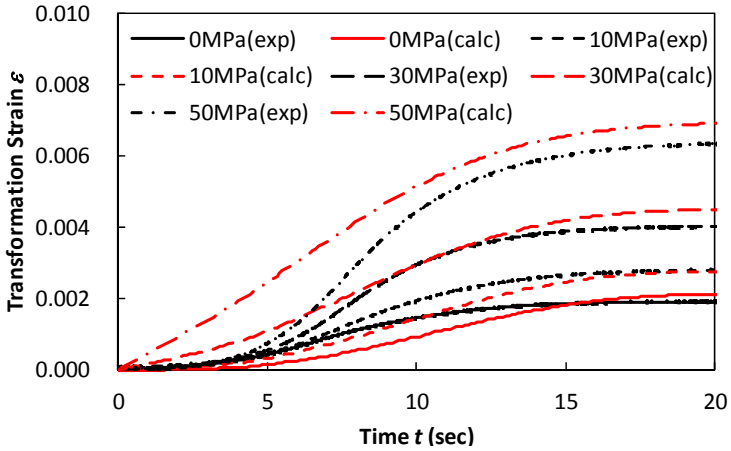

Fig. 81 Comparison of transformation strain evolution between calculation and experiment.

In spite of a good agreement at the final strain values, we obtain discrepancies on the kinetic. For small applied stress ($\sigma \leq 10$ MPa), the calculated strains by calculation evolve gently whereas the experimental results show delayed strain increase and for large applied stress ($\sigma \geq 30$ MPa) the strains by calculation show rapid increase than those of experiment.

The discrepancies may imply that the parameters which were adopted in these calculations were not appropriate to fully describe the transformation plasticity at high temperature. This indicates that the strain-rate sensitivity has to be determined accurately by experimental measurements.

Chapter 5 Conclusions and Perspectives

The mechanism of transformation plasticity in fcc-bcc (austenite-ferrite or pearlite) diffusive phase transformation and mechanical-metallurgical effect on it are discussed throughout this thesis.

In chapter 3, transformation plasticity is experimentally observed and discussed by comparing analytical model by Leblond [15]. Qualitatively, the experimental results agree with the analytical model; transformation plastic strain is proportional to transformation strain and inverse proportional to yield stress of parent (weaker) phase. The transformation plastic strain values of experiment, however, were much bigger than estimation by the model.

In chapter 4, the FFT-based numerical model with crystal plasticity and phase transformation were developed.

By using this model, the metallurgical and mechanical interaction and its influence on transformation plasticity has been analysed.

First of all, the texture effect on transformation plasticity is determined. The texture affects yield stress in parent phase and in proportion to it, the transformation plastic strain values changes although the effect is moderate.

Second, grain morphology effect is analysed. It is found that ellipsoidal shaped grains cause anisotropic transformation plastic strain.

Third, it is revealed that if a band structure is produced, it results in anisotropic transformation plastic strain, which coincides well with experimental results but the magnitude of anisotropy was much weaker for the calculation results than those of experiments.

Fourth, grain size effect is analysed. In order to realise grain size effect, a notion of Geometrically Necessary Dislocation (GND) was introduced. The developed model confirmed Hall-Petch relation. From the analyses of transformation plasticity with 10μm and 100μm average grain sizes, it was shown that the transformation plastic strain of 10μm grain size is smaller than that of 100μm. The results agree with the analytic models as they claim that the transformation plastic strain is inverse proportional to yield stress of parent phase. It should also be noted that the high dislocation density appears at the region surrounding the daughter phase particles. When two or more daughter particles approach each other, the dislocation density gains even higher.

Fifth, back stress effect on transformation plasticity was identified. Back stress is developed during plastic flow and it causes anisotropic transformation strain as well as transformation plastic strain during subsequent phase transformation.
Sixth, pearlite phase transformation is modelled to compare with ferrite phase transformation. Pearlite consists of ferrite and cementite phase and cementite is bigger and harder than ferrite. Those effects, as well as their volume percent inside pearlilte phase, were taken into account. The results of calculations show no apparent difference in transformation plasticity from pure ferrite phase.
Finally, viscoplasticity was implemented in the crystal plasticity modelling. The viscoplasticity was found to be able to explain the discrepancies between experimental results and numerical ones. The viscoplastic deformation cannot be neglected during phase transformations at high temperature. This is the reason why the numerical model developed in this thesis and analytical models agree each other with experimental ones of bainite and martensite phase transformations.
It is found that one should take into account more parameters than the previous requirements by Greenwood-Johnson [5] such as back stress and viscoplastic information. Nonetheless, it is expected that this thesis cast an indispensable knowledge on transformation plasticity and its interaction with thermo-mechanical-metallurgical effects.
In addition, a new analytical model was developed modifying the models of Leblond [15] and Taleb [17]. Then transformation plasticity is calculated by means of FFT numerical model for two different transformation strain values. By the comparison between calculated results and analytical ones, it is revealed that external stress effect causes nonlinear behaviour between applied stress and transformation plastic strain; the phenomenon is also observed by experiments. It is also found that the plastic deformation in daughter phase (stronger phase) also contribute the transformation plastic strain especially at the latter half of phase transformation. The new model takes those important effects into account and thus it agreed well with FFT numerical results.
The work on viscoplastic deformation allows to improve the new analytical model. The new model was modified by taking into account the viscoplastic behaviour during phase transformation at high temperature. The modified model shows good agreement with FFT numerical results and experimental results.

Although many phenomena concerning transformation plasticity have been discussed throughout this thesis, there still remain many aspects that should be investigated. For example, for more deep investigation, it is necessary to measure stress/strain curves at

least at two different strain rates. With this, the creep parameters can be identified and the new analytical model can be suppose to confrontation with experimental results.
Furthermore, transformation plasticity during displasive phase transformation was not treated.
Despite these remaining works, this thesis is expected to cast further apprehension on transformation plasticity in steels.

References

[1] T. Inoue , K. Okamura, “Material Database for Simulation of Metallo-Thermo-Mechanical Field,” Proceedings of the 20th Conference (ASM International), 2000.

[2] F. D. Fischer, “Q-P. Sun and K. Tanaka, Transformation-induced plasticity(TRIP),” Appl. Mech. Rev., 49, 6, 1996.

[3] L. Taleb, N. Cavallo , F. Waeckel, “Experimental analysis of transformation plasticity,” International Journal of Plasticity, 17, 2001.

[4] C. L. Magee, “Transformation kinetics, Microplasticity and Aging of Martensite in Fe-31Ni,” Ph.D. Thesis of Carnegie Institute of Technology, 1966.

[5] G. W. Greenwood , R. H. Johnson, “The Deformation of Metals under Small Stresses during Phase Transformations,” Proc. Roy. Soc. London, 283A, 1965.

[6] Y. Desalos, “Comportement dilatométrique et mécanique des materiaux d’austénite métastable d’un l’acier A533,” IRSID, rapport no.95349401 MET44, 1981.

[7] E. Gautier, A. Simon , G. Beck, “Plasticité de transformation durant la transformation perlitique d'un acier eutectoïde,” Acta Metall., 35, 1987.

[8] S. Petit-Grostabussiat, L. Taleb , J.-F. Jullien, “Experimental results on classical plasitcity of steels subjected to structural transformations,” Int. J. Plast., 20, 2004.

[9] H. -G. Lambers, S. Tschumak, H. J. Maier , D. Canadinc, “Pre-deformation-transformation plasticity relationship during martensitic transformation,” Mater. Sci. Eng. A527, 2010.

[10] A. Boudiaf, L. Taleb , M. A. Belouchrani, “Experimental analysis of the correlation between martensitic transformation plasticity and the austenitic grain size in steels,” European Journal of Mechanics A/Solids, 30, 2011.

[11] M. J. Holzweissig, D. Canadinc , H. J. Maier, “In-situ characterization of transformation plasticity during an isothermal austenite-to-bainite phase transformation,” Mater. Charact., 65, 2012.

[12] T. Inoue, Z. G. Wang , K. Miyao, “Simulation of Quenching Process of Carburized Steel Gear Wheel under Metallo-Thermo-Mechanical CouplingElsevier Science Publishers, Paris, B. V. North-Holland,” Proceedings of IUTAM Symposium on Thermomechanical Coupling in Solids, 1987-5.

[13] D. Y. Ju, W. M. Zhang , Y. Zhang, “Modeling and experimental verification of

martensitic transformation plastic behavior in carbon steel for quenching process," Mater. Sci. Eng., A 438-440, 2006.

[14] J. Montalvo-Urquizo, Q. Liu , A. Schmidt, "Simulation of quenching involved in induction hardening including mechanical effects," Comp. Mater. Sci., 79, 2013.

[15] J. B. Leblond, J. Devaux , J. C. Devaux, "Mathematical modelling of transformation plasticity in steels –I: Case of deal-plastic phases," Intl. J. Plasticity, 5, 1989.

[16] J. B. Leblond, "Mathematicl Modelling of Transformation Plasticity in Steels II: Coupling with Strain Hardening Phenomena," International Journal of Plasticity, 1989.

[17] L. Taleb , F. Sidoroff, "A micromechanical modeling of the Greenwood-Johnson mechanism in transformation induced plasticity," International Journal of Plasticity, 19, 2003.

[18] J. M. Diani, H. Sabar , M. Berveiller, "Mircromechanical modelling of the transformation induced plasticity (TRIP) phenomenon in steels," Int. J. Engng Sci., 33, 1995.

[19] M. Cherkaoui, M. Berveiller , X. Lemoine, "Couplings between plasticity and martensitic phase transformation: overall behavior of polycrystalline TRIP steels," Int. J. Plast., 16, 2000.

[20] M. Fischlschweiger, G. Cailletaud , T. Antretter, "A mean-field model for transformation induced plasticity including backstress effects for non-proportional loadings," Int. J. Plast., 37, 2012.

[21] J. F. Ganghoffer, S. Denis, E. Gautier , A. Simon, "Finite element calculation of the micromecanics of a diffusional transformation," Eur. J. Mech. A. Solids, 12, No.1, 1993.

[22] F. Barbe, R. Quey , L. Taleb, "Numerical modelling of the plasticity induced during diffusive transformation. Case of a cubic array of nuclei," Eur. J. Mech. A. Solids, 26, 2007.

[23] F. Barbe, R. Quey, L. Taleb , d. C. Souza, "Numerical modelling of the plasticity induced during diffusive transformation. An ensemble averaging approach for the case of random arrays of nuclei," European Journal of Mechanics A/Solids, 27, 2008.

[24] F. Barbe , R. Quey, "A numerical modelling of 3D polycrystal-to-polycarystal diffusive phase transformations involving crystal plasticity," International Journal of Plasticity, 27, 2011.

[25] H. Moulinec , P. Suquet, “A numerical method for computing the overall response of nonlinear composites with complex microstructure,” Computer Methods Appl. Mech. Engineering, 157, 1998.

[26] R. A. Lebensohn, R. Brenner, O. Castelnau , A. D. Rollett, “Orientation image-based micromechanical modellilng of subgrain texture evolution in polycrystalline copper,” Acta Mater., 56, 2008.

[27] S. -B. Lee, R. A. Lebensohn , A. D. Rollett, “Modeling the viscoplastic micromechanical response of two-phase materials using Fast Fourier Transfroms,” Int. J. Plast., 27, 2011.

[28] R. Brenner, R. A. Lebensohn , O. Castelnau, “Elastic anisotropy and yield surface estimates of polycrystals,” Int. J. Solids Struct., 46, 2009.

[29] P. Suquet, H. Moulinec, O. Castelnau, M. Montagnat, N. Lahellec, F. Grennerat, P. Duval , R. Brenner, “Multi-scale modeling of the mechanical behavior of polycrystalline ice under transient creep,” Procedia IUTAM, 3, 2012.

[30] R. A. Lebensohn, A. K. Kanjarla , P. Eisenlohr, “An elasto-viscoplastic formulation based on fast Fourier transforms for the prediction of micromechanical fields in polycrystalline materials,” Int. J. Plast., 32-33, 2012.

[31] P. Eisenlohr, M. Diehl, R. A. Lebensohn , F. Roters, “A spectral method solution to crystal elasto-viscoplasticity at finite strains,” Int. J. Plast., 46, 2013.

[32] W. Ludwig, S. Schmidt, E. M. Lauridsene , H. F. Poulsen, “X-ray diffraction contrast tomography: a novel technique for three-dimensional grain mapping of polycrystals. i. direct beam case,” J. Appl. Cryst., 41, 2008.

[33] A. Belkhabbaz, R. Brenner, N. Rupin, B. Bacroix , J. Fonseca, “Prediction of the overall behavior of a 3D microstructure of austenitic steel by using FFT numerical scheme,” Procedia Engineering, 10, 2011.

[34] F. Grennerat, M. Montagnat, O. Castenlau, P. Vacher, H. Moulinec, P. Suquet , P. Duval, “Experimental characterization of the intragranular strain field in columnar ice during during transient creep,” Acta Mater., 60, 2012.

[35] G. Wassermann, “Untersuchungen an einer Eisen-Nickel-Legierung über die Verformbarkeit während der α-γ-Umwandlung,” Arch Eisenhüttenwesen, 10, 7, 1937.

[36] K. Miyao, Z. G. Wang , T. Inoue, “Analysis of Temperature, Stress and Mecallic Structure in Carburized-Quenchied Gear Considering Transformation Plasticity (in Japanese),” Journal of the Society of Materials Science, Japan, 35, 399, 1986.

[37] L. Taleb, S. Petit , J. -F. Jullien, “Prediction of residual stresses in the heat affected zone,” J. Phys. IV France, 120, 2004.

[38] M. Fukumoto, M. Yoshizaki, H. Imataka , K. Okamura, “Three-Dimensional FEM Analysis of Helical Gear Subjected to the Carburized Quenching Process (in Japanese),” Journal of the Society of Materials Science Japan, 50, 6, 2001.

[39] L. Taleb , S. Petit, “New investigations on transformation induced plasticity and its interaction with classical plasticity,” International Journal of Plasticity, 22, 2006.

[40] H. Nozaki, Y. Nishikawa, Y. Uesugi , I. Tamura, “Effect of Initial Grain Size of Austenite on Transformation Superplasticity in Steel,” Journal of Japan Society for Technology of Plasticity, 26, 289, 1985.

[41] G. C. Videau, G. Cailletaud , A. Pineau, “Experimental study of the transformation induced plasticity in a Cr-Ni-Mo-Al-Ti steel,” Journal de Physique IV, colloque C1, Supplèment au J de phisique III, 6, 1995.

[42] T. Otsuka, T. Akashi, S. Ogawa, T. Imai , A. Egami, “Effect of Volume Expansion on Transformation Plasticity during Ferrite and Martensite Transformation of Steel,” Journal of the Society of Materials Science Japan, 60, 10, 2011.

[43] T. Otsuka, Y. Wakasu , T. Inoue, “A simple identification of transformation plastic behaviour and some data for heat treating materials,” Int. J. Mater. Prod. Technol., 24, 1-4, 2005.

[44] K. Arimoto, “Heat treatment simulations and their validation (in Japanese),” Arimotech Ltd. publishment, 2006.

[45] F. Abrassart, “Influence des transformations martensitique sur les propriétés mécanique des alliages du systèm Fe-Ni-Cr-C,” Thèse de Doctorat ès-Sciences Physiques, Université de Nancy I, 1972.

[46] H. Nozaki, Y. Uesugi, T. Okada, Y. Nishikawa , I. Tamura, “Application of Internal Stress Theory to Phase Transformation Plasticity in Steels at High Applied Stress Range (in Japanese),” Journal of the Japan Society for Technology of Plasticity, 26, 288, 1985.

[47] J. W. Hutchinson, “Elastic-plastic behaviour of poly crystalline metals and composites,” Proceedings of Royal Society of London, A.319, 1970.

[48] D. Peirce, R. J. Asaro , A. Needleman, “An analysis of non-uniform and localized deformation in ductile single crystals,” Acta Metall., 30, 1982.

[49] J. E. Bailey , P. B. Hirsch, “The dislocation distribution, flow stress, and stored energy in cold-worked polycrystalline silver,” Philos. Mag., 5, 53, 1960.

[50] L. Tabourot, M. Fivel , E. Rauch, “Generalised constitutive laws for f.c.c. single crystals,” Materials Science and Engineering, A234-236, 1997.

[51] H. Mecking , Y. Estrin, Proc. Int. Symp. Metallurgy and Materials Science, Riso, Denmark, 1987.

[52] P. Franciosi, M. Berveiller , A. Zaoui, “Latent hardening in copper and aluminium single crystals,” Acta Metallurgica, 28, 1979.

[53] M. Kuroda , K. Shizawa, “Theory and application of crystal plasticity (in Japanese),” Journal of the JSTP, 2002.

[54] M. F. Ashby, “The deformation of plastically non-homogeneous materials,” Phylosophical Magasine, 21, 1970.

[55] M. A. Zikry , M. Kao, “Inelastic microstructural failure mechanisms in crystalline materials with high angle grain boundaries,” Journal of the Mechanics and Physics of Solids, 44, 11, 1996.

[56] D. Walgraef , E. C. Aifantis, “Dislocation patterning in fatigued metals as a result of dynamical instabilities,” J. Appl. Phys., 58(2), 1985.

[57] J. Pontes, D. Walgraef , C. I. Christov, “Numerical Solution of the Walgraef-Aifantis Model for Simulation of Dislocation Dynamics in Materials S¥ubjected to Cyclic Loading,” Conference Proceedings of the Society for Experimental Mechanics, 2011.

[58] E. Kröner, “Kontinuumstheorie der Versetzungen und Eigenspannungen (Ergebnisse der angewandten Mathematik),” Springer; 1 edition, 1958.

[59] J. W. Hutchinson, “Bounds and self-consistent estimates for creep of polycrystalline materials,” Proceedings of the Royal Society of London A, 348, 1976.

[60] L. Anand , M. Kothari, “A computational procedure for rate-independent crystal plasticity,” J. Mech. Phys. Solids, 44, 4, 1996.

[61] J. Pan , J. R. Rice, “Rate sensitivity of plastic flow and implications for yield-surface vertices,” International Journal of Solids and Structures, 19, 11, 1983.

[62] A. Jablonka, K. Harster , K. Schwerdtfeger, “Thermomechanical properties of iron and iron-carbon alloys : density and thermal contraction,” Steel Research, 62, 1, 1991.

[63] J. Miettinen, “Calculation of solidification-related thermo physical properties for steels,” Metallurgical and Materials Transactions B, 28B, 1997.

[64] W. A. Johnson , R. F. Mehl, “Reaction kinetics in process of nucleation and growth,” Trans AIME, 135, 1939.

[65] D. P. Koistinen , R. E. Marburger, Acta metal, 7, 1959.

[66] C. L. Magee, “Phase Transformation,” Metals Park, AMS, in H. I. Aaronson(ed), 1968.

[67] Z. G. Wang , T. Inoue, “Quenching simulation of temperature, stress dependent phase and stress for steels (in Japanese),” Jounal of Society of Material and Science, Japan, 32, 360, 1983.

[68] C. Cabus, “Etude et modélisation des textures de transformations de phases dans les aciers destinés à l'emboutissage,” Doctoral thesis of University Paris 13, 2005.

[69] H. K. D. H. Bhadeshia, “Effect of stress & strain on formation of Bainite in steels,” HotWorkability of Steels and Light Alloys–Composites, 1996.

[70] H. Miyaji , H. Furubayashi, “Effect of stress on the variant selection in Martensitic transformation,” Textures and Microstructure, vol.14-18, 1991.

[71] E. C. Oliver, T. Mori, M. R. Daymond , P. J. Withers, “Neutron diffraction study of stress-induced martensitic transformation and variant change in Fe–Pd,” Acta Materialia 51, 2003.

[72] C. Bain, “The nature of martensite,” Trans AIME, 70, 1924.

[73] G. Kurdjumov , G. Sachs, “Über den Mechanismus der Stahlhärtung,” Z. Phys., 64, 1930.

[74] Z. Nishiyama, “X-Ray investigation of the mechanism of the transformation from face-centred cubic lattice to body-centred cubic,” Sci. Rep. Tohoku Imp. Univ. 23, 1934/1935.

[75] H. Kitahara, R. Ueji, M. Ueda, N. Tsuji , Y. Minamino, “Crystallographic analysis of plate martensite in Fe–28.5 at.% Ni by FE-SEM/EBSD,” Materials Characterization, 54, 2005.

[76] T. Fujii, M. Ogawa, S. Onaka , M. Kato, “Preferential Precipitation of Cr Particles on Dislocations in a Cu-0.32 mass%Cr Alloy,” J. Japan Inst. Metals, Vol.66, No.10, 2002.

[77] E. Scheil, “Anlaufzeit der Austenitumwandlung,” Arc. Eisenhuttenwesen. 12,, 1935.

[78] A. Shibata, H. Yonezawa, K. Yabuuchi, S. Morito, T. Furuhara , T. Maki, “Relation between martensite morphology and volume change accompanying fcc to bcc martensitic transformation in Fe-Ni-Co alloys,” Materials Science and Engineering, A438-440, 2006.

[79] J. B. Leblond, G. Mottet , D. C. Devaux, “A Theoretical and Numerical Approach to the Plastic Behaviour of Steels During Phase Transformations-I. Derivation of

General Relations," J. Mech. Phys. Solids, 34, 4, 1986.

[80] T. A. Kop, J. Sietsma , S. van der Zwaag, "Anisotropic dilatation behaviour during transformation of hot rolled steels showing banded structure," Materials Science and Technology, 17, 2001.

[81] E. O. Hall, "The Deformation and Ageing of Mild Steel: III Discussion of Results," Proc. Phys. Soc. B64, 1951.

[82] N. J. Petch, "The cleavage strength of polycrystals," J. Iron Steel Inst. 174: 25-8, 1953.

[83] A. Acharya , A. J. Beaudoin, "Grain-size effect in viscoplastic polycrystals at moderate strains," Journal of the Mechanics and Physics of Solids, 48, 2000.

[84] T. Ohashi, "Finite-element analysis of plastic slip and evolution of geometrically necessary dislocations in fcc crystals," Philos. Mag. Lett., 75, 2, 1997.

[85] K. Nagayama, T. Terasaki, K. Tanaka, F. D. Fischer , G. Cailletaud, "An Experimental Study of TRIP Behavior in a Cr-Ni-Mo-Al-Ti Maraging Steel - Evolution of TRIP Strain and Back Stress -," J. Soc. Mat. Sci. Japan, Vol.50, No.8, 2001.

[86] C. O. Frederick , P. J. Armstrong, "A mathematical representation of the multiaxial Bauschinger effect," Materials at High Temperatures, Vol.24, No.1, 2007.

[87] T. Inoue, "Unified Transformation-Thermoplasticity and the Application (in Japanese)," Journal of the Society of Materials Science, Japan, 56, 4, 2007.

[88] J. P. Ponthot , T. Belytschko, "Arbitrary Lagrangian-Eularian formulation for element-free Galerkin method," Comput. Methods Appl. Mech. Engrg., 152, 1998.

[89] D. Sulsky, S. J. Zhou , H. L. Schreyer, "Application of a particle-in-cell method to solid mechanics," Computer Physics Communications, 87, 1995.

[90] R. A. Lebensohn, "N-site modeling of a 3D viscoplastic polycrystal using fast Fourier transform," Acta Mater., 49, 2001.

Appendix A: Large deformation simulation of mono crystalline material

In order to identify the effect of rotation of crystallographic orientation, large deformation simulation considering rotation is performed.

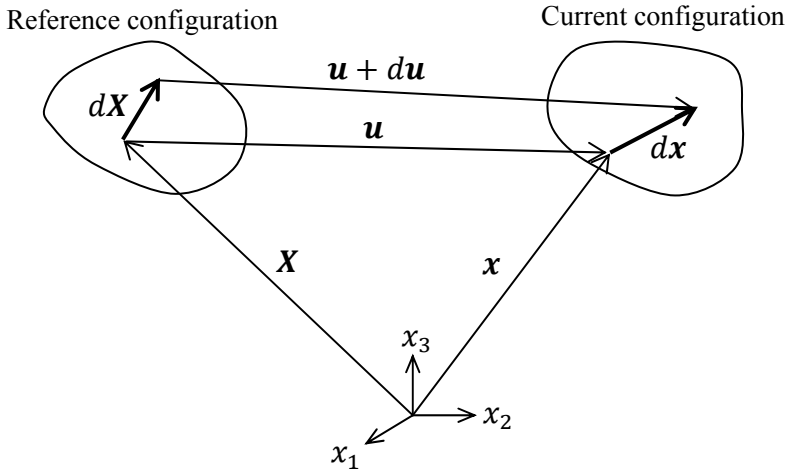

Fig. 82 Description of configuration during deformation.

Fig. 82 shows a schematic view of configurations of reference, before deformation and of current. Using this notion, engineering stress Π_{ij} (1st Piola-Kirchhoff stress) is defined as follows.

$$T_i = \Pi_{ij} N_j \ , \tag{170}$$

where N_j is a surface where the force T_i is acting before deformation. The Cauchy stress σ_{ij} and 2nd Piola-Kirchhoff stress Σ_{ij} are:

$$t_i = \sigma_{ij} n_j \ , \tag{171}$$

$$T_i^* = \Sigma_{ij} N_j \ . \tag{172}$$

And Nanson's theorem connects both surfaces of before deformation and current such that,

$$N_j dS_0 = \frac{\rho}{\rho_0} F_{ij} n_i dS \ , \tag{173}$$

where ρ_0 and ρ represent density of the material before deformation and that of current state. F_{ij} is deformation gradient. If we define J a determinant of the deformation gradient F_{ij}, these three stresses are related with using J such that,

$$\sigma_{ij} = \frac{1}{J} \Pi_{ik} F_{jk} \ , \tag{174}$$

$$\Pi_{ij} = J \sigma_{ik} F_{jk}^{-1} \ , \tag{175}$$

$$\Sigma_{ij} = J F_{ik}^{-1} \sigma_{kl} F_{jl}^{-1} \ . \tag{176}$$

And the equilibrium condition is:

$$\frac{\partial \Pi_{ij}}{\partial X_j} = 0 \ . \tag{177}$$

If one considers the current configuration as reference configuration, i.e. update Lagrange, following equations are satisfied,

$$\Pi_{ij} = \sigma_{ij} \ , \ X_i = x_i \ , \ F_{ij} = \delta_{ij} \ , \ \dot{J} = J L_{kk} \ , \tag{178}$$

where $L_{ij} = \dot{u}_{i,j}$ is velocity gradient. In this case, each stress rate can be written as follows

$$\dot{\Pi}_{ij} = \dot{\sigma}_{ij} + \sigma_{ij} L_{kk} - \sigma_{ik} L_{jk} \ , \tag{179}$$

$$\dot{\Sigma}_{ij} = \dot{\sigma}_{ij} + \sigma_{ij} L_{kk} - L_{ik} \sigma_{kj} - \sigma_{ik} L_{jk} \ , \tag{180}$$

with the equilibrium condition:

$$\dot{\Pi}_{ij,j} = 0 \ . \tag{181}$$

In contrast, for the solution by FFT, the material points have to be fixed in the calculation space. This means that the transportation equation of internal variables should be solved and they have to be interpolated/extrapolated to Euler coordinate. For example, ALE [88] or particles-in-cell method [89] may be incorporated with FFT method.

For large deformation problems, constitutive equations should not be dependent on the coordinate which observers define. First of all, suppose that velocity gradient L_{ij} can be divided into elastic L_{ij}^{*} and plastic L_{ij}^{p} parts, such that

$$L_{ij} = L_{ij}^{*} + L_{ij}^{p} \ . \tag{182}$$

This elasto-plastic decomposition is explained in Fig. 83. The total deformation gradient is divided into plastic part F_{ij}^{p}, which impose no rotation of slip vectors m_i and s_i, and elastic part F_{ij}^{*}, which impose rotation of slip vectors.

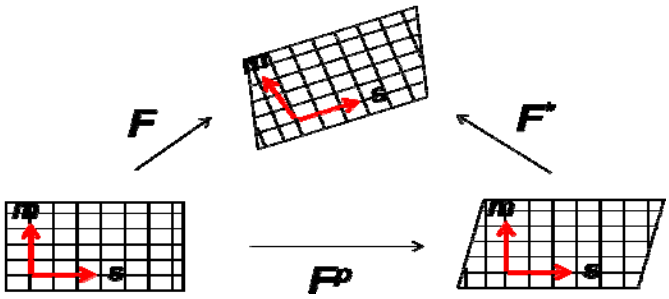

Fig. 83 Elasto-Plastic decomposition of deformation gradient.

The plastic part L_{ij}^{p} is a summation of shear slips of each slip system.

$$L_{ij}^{p} = \sum_{\alpha} \dot{\gamma}^{\alpha} s_i^{\alpha} m_j^{\alpha} \ . \tag{183}$$

Splitting L_{ij}^{p} into symmetric and asymmetric part, such that

$$D_{ij}^{p} = \sum_{\alpha} \dot{\gamma}^{\alpha} \left[\frac{1}{2}\left(s_i^{\alpha} m_j^{\alpha} + s_j^{\alpha} m_i^{\alpha}\right)\right] \equiv \sum_{\alpha} \dot{\gamma}^{\alpha} p_{ij}^{\alpha} \ , \tag{184}$$

$$W_{ij}^{p} = \sum_{\alpha} \dot{\gamma}^{\alpha} \left[\frac{1}{2}\left(s_i^{\alpha} m_j^{\alpha} - s_j^{\alpha} m_i^{\alpha}\right)\right] \equiv \sum_{\alpha} \dot{\gamma}^{\alpha} w_{ij}^{\alpha} \ . \tag{185}$$

D_{ij}^{p} is plastic strain (stretching) tensor and W_{ij}^{p} is plastic spin tensor. Then we consider elastic part of L_{ij}, i.e. L_{ij}^{*}. The symmetric and asymmetric part of L_{ij}^{*} are:

$$D_{ij}^{*} = \frac{1}{2}\left(L_{ij}^{*} + L_{ji}^{*}\right) , \tag{186}$$

$$W_{ij}^{*} = \frac{1}{2}\left(L_{ij}^{*} - L_{ji}^{*}\right) . \tag{187}$$

Local stress can be considered as result of elastic deformation rate. Then one can write as follows.

$$\mathring{\sigma}_{ij}^{*} = \dot{\sigma}_{ij} - W_{im}^{*}\sigma_{mj} + \sigma_{im}W_{mj}^{*} = C_{ijkl}D_{kl}^{*} \ . \tag{188}$$

Because $D_{ij} = D_{ij}^{*} + D_{ij}^{p}$, equation (188) can be deformed as,

$$\mathring{\sigma}_{ij}^{*} = C_{ijkl}D_{kl}^{*} = C_{ijkl}D_{kl} - C_{ijkl}D_{kl}^{p} = C_{ijkl}D_{kl} - \sum_{\alpha} \dot{\gamma}^{\alpha} C_{ijkl} p_{kl}^{\alpha} \ . \tag{189}$$

If we introduce stress Jaumann rate:

$$\mathring{\sigma}_{ij} = \dot{\sigma}_{ij} - W_{im}\sigma_{mj} + \sigma_{im}W_{mj} \ , \tag{190}$$

using equation (185), (188) and (189),the Jaumann rate of Cauchy stress becomes as follows.

$$\begin{aligned}
\mathring{\sigma}_{ij} &= \dot{\sigma}_{ij} - W_{im}^{*}\sigma_{mj} + \sigma_{im}W_{mj}^{*} - \left(-W_{im}^{p}\sigma_{mj} + \sigma_{im}W_{mj}^{p}\right) \\
&= C_{ijkl}D_{kl} - \sum_{\alpha} \dot{\gamma}^{\alpha} C_{ijkl} p_{kl}^{\alpha} - \left(-W_{im}^{p}\sigma_{mj} + \sigma_{im}W_{mj}^{p}\right) \\
&= C_{ijkl}D_{kl} - \sum_{\alpha} \dot{\gamma}^{\alpha} C_{ijkl} p_{kl}^{\alpha} - \left(-\sum_{\alpha} \dot{\gamma}^{\alpha} w_{im}^{\alpha}\, \sigma_{mj} + \sum_{\alpha} \dot{\gamma}^{\alpha} \sigma_{im} w_{mj}^{\alpha}\right) \\
&= C_{ijkl}D_{kl} - \sum_{\alpha} \dot{\gamma}^{\alpha}\left(C_{ijkl} p_{kl}^{\alpha} + w_{im}^{\alpha}\sigma_{mj} - \sigma_{im} w_{mj}^{\alpha}\right) \ .
\end{aligned} \tag{191}$$

The solution of equation (191) by using FFT is given by following. Again we introduce the polarisation tensor τ_{ij}. In contrast to previous discussion, for the purpose of

calculating spin, stress rate and strain rate are calculated instead of total stress and strain. Starting with equation (191) with polarisation tensor, we obtain:

$$\mathring{\sigma}_{ij} = C_{ijkl} D_{kl} + \mathring{\tau}_{ij} \ , \tag{192}$$

and rewriting the equilibrium condition:

$$\dot{\Pi}_{ij,j} = 0 \ . \tag{193}$$

Equations (192) and (193) in the Fourier space are:

$$\begin{aligned} \hat{\mathring{\sigma}}_{ij} &= iC^0_{ijkl}\xi_l \hat{u}_k(\xi) - \hat{\mathring{\tau}}_{ij}(\xi) \ , \\ i\xi_i\left(\hat{\sigma}_{ij} + \hat{\sigma}_{ij}\hat{L}_{kk} - \hat{\sigma}_{ik}\hat{L}_{jk}\right) &= i\xi_i\left(\hat{\mathring{\sigma}} + \hat{\sigma}_{ij}\hat{L}_{kk} - \hat{\sigma}_{ik}\hat{L}_{jk} + \widehat{W}_{im}\hat{\sigma}_{mj} - \hat{\sigma}_{im}\widehat{W}_{mj}\right) \\ &= 0 \ . \end{aligned} \tag{194}$$

Eliminating $\hat{\mathring{\sigma}}_{ij}$ from equation (194), we obtain

$$\hat{u}_k(\xi) = \frac{i}{2}\left(N^0_{kl}\xi_j + N^0_{kj}\xi_i\right)\hat{\mathring{\tau}}'_{ij}(\xi) \ , \tag{195}$$

where

$$\hat{\mathring{\tau}}'_{ij}(\xi) = \hat{\mathring{\tau}}_{ij}(\xi) - \widehat{W}_{im}\hat{\sigma}_{mj} + \hat{\sigma}_{im}\widehat{W}_{mj} + \hat{\sigma}_{ij}\hat{L}_{kk} - \hat{\sigma}_{ik}\hat{L}_{jk} \ , \tag{196}$$

and,

$$N^0_{ij}(\xi) = K^0_{ij}(\xi)^{-1}, \ K^0_{ij}(\xi) = C^0_{ikjl}\xi_k\xi_l \ . \tag{197}$$

Thus, the stretching (strain) and spin rate tensor can be solved:

$$\widehat{D}_{kl}(\xi) = \frac{i}{2}\left(\xi_l\hat{u}_k(\xi) + \xi_k\hat{u}_l(\xi)\right) = -\hat{\Gamma}^0_{klij}(\xi)\hat{\mathring{\tau}}'_{ij}(\xi) \tag{198}$$

$$\widehat{W}_{kl}(\xi) = \frac{i}{2}\left(\xi_l\hat{u}_k(\xi) - \xi_k\hat{u}_l(\xi)\right) = -\hat{\Gamma}'^0_{klij}(\xi)\hat{\mathring{\tau}}'_{ij}(\xi) \ , \tag{199}$$

where

$$\begin{aligned} \hat{\Gamma}^0_{klij} &= \frac{1}{4}\left(N^0_{li}\xi_j\xi_k + N^0_{ki}\xi_j\xi_l + N^0_{lj}\xi_i\xi_k + N^0_{kj}\xi_i\xi_l\right) \\ \hat{\Gamma}'^0_{klij} &= \frac{1}{4}\left(-N^0_{li}\xi_j\xi_k + N^0_{ki}\xi_j\xi_l - N^0_{lj}\xi_i\xi_k + N^0_{kj}\xi_i\xi_l\right) . \end{aligned} \tag{200}$$

FFT method uses Euler type mesh, which means that the calculation points are not set on the materials points but on the special points. It means that for the solution of large deformation, one should take the transportation equation into account.

The iterative solution is follows.

Iterative algorithm (without transportation equation)

Initialise, $D_{ij}^{0}(x) = D_{ij}^{n}(x)$ at the last step, $\forall x \in V$

Iteration n+1: $D_{ij}^{n}(x)$ and $\overset{\circ}{\sigma}_{ij}^{n}(x)$ are already known

(b) Check convergence $e^{n} = \dfrac{\sqrt{\langle \left\| \overset{\circ}{\sigma}_{ii}^{n} \right\|^{2} \rangle}}{\langle \left\| \overset{\circ}{\sigma}_{ii}^{n} \right\| \rangle} = \dfrac{\sqrt{\langle \left\| \xi_i \hat{\overset{\circ}{\sigma}}_{ii}^{n}(\xi) \right\|^{2} \rangle}}{\langle \left\| \hat{\overset{\circ}{\sigma}}_{ii}^{n}(0) \right\| \rangle} < 1.0 \times 10^{-4}$

(c) $\hat{D}_{ij}^{n+1}(\xi) = \hat{D}_{ij}^{n}(\xi) - \hat{\Gamma}_{ijkl}^{0}(\xi)\hat{\overset{\circ}{\sigma}}_{kl}^{n}(\xi) \quad \forall \xi \neq 0 \quad \text{and} \quad \hat{D}_{ij}^{n+1}(0) = \dot{\bar{\varepsilon}}$

(d) $\hat{W}_{ij}^{n+1}(\xi) = \hat{W}_{ij}^{n}(\xi) - \hat{\Gamma}'^{0}_{ijkl}(\xi)\hat{\overset{\circ}{\sigma}}_{kl}^{n}(\xi) \quad \forall \xi \neq 0 \quad \text{and} \quad \hat{W}_{ij}^{n+1}(0) = 0$

(e) $D_{ij}^{n+1} = FFT^{-1}(\hat{D}^{n+1})$

(f) $W_{ij}^{n+1} = FFT^{-1}(\hat{W}^{n+1})$

(g) $\overset{\circ}{\sigma}_{ij}^{n+1}(x) = g\left(D_{kl}^{n+1}(x)\right) \qquad \forall x \in V$

when converged,

(h) $\dot{\sigma}_{ij} = \overset{\circ}{\sigma}_{ij} + W_{im}\sigma_{mj} - \sigma_{im}W_{mj}$

(i) $\sigma_{ij} = \sigma_{ij} + \dot{\sigma}_{ij}$

In addition to above FFT solution, following hardening law is applied. Starting with Baily-Hirsch equation for visco-plastic materials:

$$\tau = a\mu\tilde{b}\sqrt{\rho}\,, \tag{201}$$

where τ is resolved shear stress, a is a dimensionless constant, μ is Young's modulus and $\tilde{b}$ is magnitude of Bergers vector. Then, the extended hardening model is obtained as:

$$g^{\alpha} = a\mu\tilde{b}\sqrt{\sum_{\beta} d^{\alpha\beta}\rho^{\beta}}\,, \tag{202}$$

or for visco-plastic model:

$$g^{\alpha} = a\mu\tilde{b}\sqrt{\sum_{\beta} d^{\alpha\beta}\rho^{\beta}}\,, \tag{203}$$

where $d^{\alpha\beta}$ is effect of each dislocation density ρ^{β} on g^{α}. The rate form of equation (203) is:

$$\dot{g}^{\alpha} = \frac{a\mu\tilde{b}\sum_{\beta} d^{\alpha\beta}\dot{\rho}^{\beta}}{2\sqrt{\sum_{\beta} d^{\alpha\beta}\rho^{\beta}}} \ . \tag{204}$$

Tabourot *et al.*[50] used a model by Mecking and Estrin[51]. In this model, (α) dislocation evolution is expressed as a summation of each dislocation forest (β) and annihilation of (α) dislocation controlled b the mean distance y_c such that,

$$\dot{\rho}^{\alpha} = \frac{1}{\tilde{b}}\left(\sqrt{\frac{\sum_{\beta} a^{\alpha\beta}\rho^{\beta}}{K}} - 2y_c\rho^{\alpha}\right)|\dot{\gamma}^{\alpha}| \ . \tag{205}$$

The interaction matrix $a^{\alpha\beta}$ takes the values shown in Table 23.

In order to conform to Hutchinson model, let $h^{\alpha\beta}$ a redefined hardening parameter, such that:

$$h^{\alpha\beta} = \frac{a\mu d^{\alpha\beta}}{2\sqrt{\sum_{s} d^{\alpha s}\rho^{s}}}\left(\sqrt{\frac{\sum_{s} \alpha^{\beta s}\rho^{s}}{K}} - 2y_c\rho^{\beta}\right) , \tag{206}$$

then the whole procedure of finding slip rate $\dot{\gamma}^{\alpha}$ will be exactly the same as equation (57).

Table 22 Parameters values for Cu metal [50].

T(K)	μ(GPa)	b(m)	m	$\dot{\gamma}_0$(s^{-1})	α	ρ_0(m^{-2})	y_c	K
295	42	2.56×10^{-10}	0.05	10^{-10}	0.3	10^{10}	$3.36b$	38

Table 23 Interaction coefficients represented by parameters in Table 7.

h^0	h^1	h^2	h^3	h^4	h^5
0.2	0.3	0.4	0.4	1.0	0.2
	$d^{\alpha\beta}$ if $\alpha = \beta$			0.0	
	$d^{\alpha\beta}$ if $\alpha \neq \beta$			1.0	

The strain value of α slip system $\dot{\gamma}^{\alpha}$ is determined by following visco-plastic model.

$$\dot{\gamma}^{\alpha} = \dot{\gamma}_0\left(\frac{\tau^{\alpha}}{g^{\alpha}}\right)\left|\frac{\tau^{\alpha}}{g^{\alpha}}\right|^{\frac{1}{m}-1} \ . \tag{207}$$

The single point is employed for the calculation. The point is loaded toward $[\bar{1}25]$ direction and its strain and resolved shear stress are observed.

Results and discussion

Obtained stress-strain curve of primary glide is shown in Fig. 84, and comparison of primary and secondary glide is shown in Fig. 85.

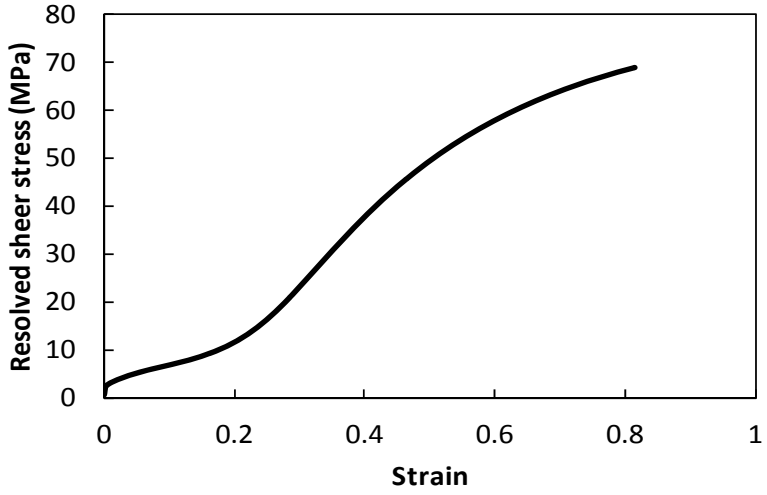

Fig. 84 Stress-strain curve of primary glide.

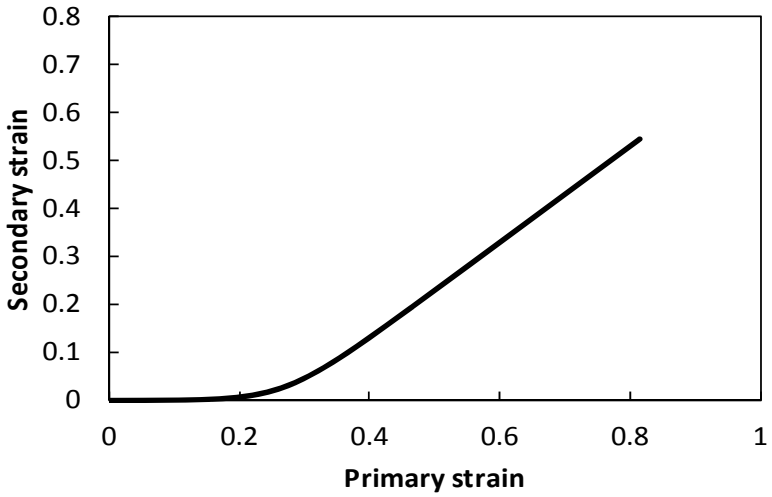

Fig. 85 Comparison of strain value between primary and secondary glide.

From Fig. 84 and Fig. 85, it is clear that from about 20% of primary slip strain, the secondary glide is activated. Right after the activation of secondary glide, because of the latent hardening, the resolved shear stress increases. The activation of secondary glide is due to the rotation of crystallographic orientation.

Fig. 86 shows the position of the initial tensile axis $[\bar{1}25]$ during deformation. It is also confirmed that after the activation of secondary glide, the rotating direction is changed.

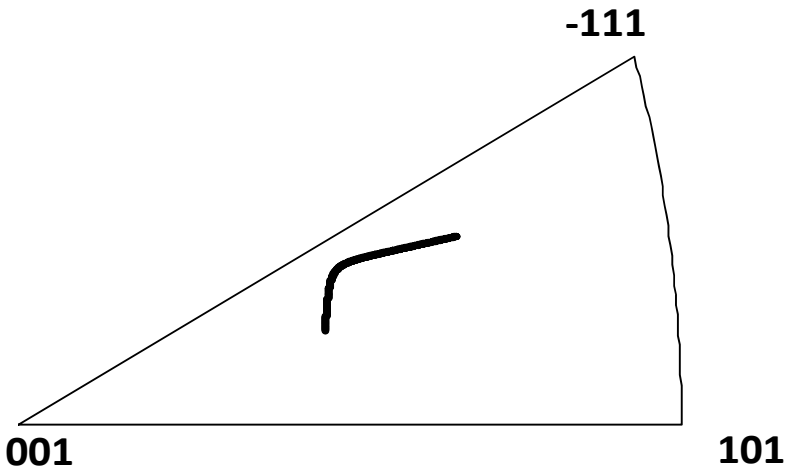

Fig. 86 Inverse pole figure of $[\bar{1}25]$ axis (initial loading direction) during deformation.